Towards Spatiotemporal Resolution of Copper Aspartate in Gel

Poh Ying Fong

A Thesis

in

The Department

of

Chemistry and Biochemistry

Presented in Partial Fulfillment of the Requirements

For the Degree of Master of Science (Chemistry) at

Concordia University

Montréal, Québec, Canada

October 2024

CONCORDIA UNIVERSITY
School of Graduate Studies

This is to certify that the thesis prepared

By: Poh Ying Fong

Entitled: Towards spatiotemporal resolution of copper aspartate in gel

and submitted in partial fulfillment of the requirements for the degree of

Master of Science (Chemistry)

complies with the regulations of the University and meets the accepted standards with respect to originality and quality.

Signed by the final examining committee:

_____ Chair
Dr. Louis A. Cuccia

_____ Examiner
Dr. Marek B. Majewski

_____ Examiner
Dr. Ashlee J. Howarth

_____ Thesis Supervisor(s)
Dr. Louis A. Cuccia

_____ Thesis Supervisor(s)
Dr. Fiorenzo Vetrone

Approved by _____
Dr. Louis A. Cuccia (Graduate Program Director)

_____
Dr. Pascale Sicotte (Dean, Faculty of Arts and Science)

Abstract

Towards Spatiotemporal Resolution of Copper Aspartate in Gel

Poh Ying Fong

Chiral resolution is essential in the pharmaceutical and food industries, as well as in material engineering, due to the unique properties of enantiomers. This study explores the coordination polymerization of homochiral (L- and D-) and racemic (DL-) copper aspartate (CuAsp) and spatiotemporal resolution of racemic aspartic acid (DL-Asp) using L- and D-proline (Pro)-copper complexes as tailor-made additives (TMAs) *via* reaction-diffusion frameworks (RDFs) in both 1D and 2D agar gel systems. The imposed supersaturation gradient translates into a gradient of crystal sizes facilitating the formation of CuAsp coordination polymers with spherulitic morphology. Solid-state circular dichroism (CD) and powder X-ray diffraction (PXRD) analyses confirmed the chiral nature and crystalline phases of the CuAsp polymers, with DL-CuAsp forming as conglomerates. Drawing inspiration from Kaoru Harada's seminal work on the resolution of DL-Asp using L- and D-Pro-copper complexes, the preferential crystallization with 'rule of reversal' was evident, where the crystalline CuAsp near the liquid-gel interface exhibited the opposite configuration to those of the TMA. Variability in chirality was noted further from the interface due to concentration gradients. These findings underscore the utility of RDF coupled with the rule of reversal in chiral resolutions, offering an effective strategy for enhancing enantioselectivity in racemic compounds across various applications.

Acknowledgments

First, I would like to extend my deepest gratitude to my research supervisor, Dr. Louis A. Cuccia. His relentless support, patience, motivation, and extensive knowledge have been the backbone of my research journey. His guidance was invaluable throughout both the research and writing phases of this thesis.

I also wish to express my sincere thanks to my co-supervisor, Dr. Fiorenzo Vetrone, and Dr. Mazen al-Ghoul. Their expertise, critical insights, and encouragement have greatly contributed to refining my research.

I am extremely grateful to my thesis committee, Dr. Marek Majewski and Dr. Ashlee Howarth, for their thoughtful comments, encouragement, and invaluable suggestions. Special thanks to Dr. Howarth for allowing access to the PXRD instrument in her lab, which was crucial for my work.

I am particularly grateful to the professionals I had privilege to collaborate with: Manal Ammar, who helped with the preliminary SEM analysis; Dr. Scott Bohle, who provided the capillary tubes for XRD analysis; Dr. Mihails Arhangelskis and Dr. Hatem Titi, who assisted in solving the crystal structure; and Victor Quezada-Novoa and Christopher Copeman from Dr. Howarth's group, who helped with PXRD operations. Additionally, my thanks go to all the technical staff in Chemistry and Biochemistry Department for accommodating my numerous requests over the past two years.

To my lab mates – Jean-Louis Do, Greg, Natalia, Hadi, and Tsion – I am grateful for the camaraderie, support, and countless stimulating discussions. You have made this journey much more enjoyable. I would also like to thank Sehrish for her contribution to the preliminary work on the coordination polymerization of homochiral and racemic copper aspartate in gel (*section* 2.2.2.1)

Finally, to my family, I express my deepest gratitude for your unwavering support, understanding, and endless love throughout my academic journey.

Table of contents

List of figures

List of abbreviations

Ala	Alanine
Asn	Asparagine
Asn•H_2O	Asparagine monohydrate
Asp	Aspartic acid
BZ	Belousov-Zhabotinsky reaction
CD	Circular dichroism
CPs	Coordination polymers
$Cu(NO_3)_2$•$3H_2O$	Copper nitrate trihydrate
$Cu(NO_3)_2$•$6H_2O$	Copper nitrate hexahydrate
CuAmi	Copper aminoadipate
CuAsp	Copper aspartate
CuGlu	Copper glutamate
Cys	Cysteine
DBS	1,3:2,4-dibenzylidene-D-sorbitol
FESEM	Field-emission scanning electron microscopy
FTIR	Fourier transform infrared spectroscopy
Glu	Glutamic acid
Ln	Lanthanide
LPs	Liesegang patterns
MOFs	Metal-organic frameworks
$NaClO_3$	Sodium chlorate

NaOH	Sodium hydroxide
NIR	Near-infrared
PC	Preferential crystallization
Pro	Proline
PXRD	Powder X-ray diffraction
RD	Reaction-diffusion
RDF	Reaction-diffusion framework
SCXRD	Single crystal X-ray diffraction
SEM	Scanning electron microscopy
SMS	Sodium metasilicate
TbAsp	Terbium aspartate
TEM	Transmission electron microscopy
TGA	Thermogravimetric analysis
Thr	Threonine
TMAs	Tailor-made additives
XPS	X-ray photoelectron spectroscopy
XRD	X-ray diffraction

Chapter 1

1.1 Pattern formation

Self-assembly and self-organization are the fundamental mechanisms that drive the formation of complex patterns across both animate and inanimate systems.[1] These processes facilitate the emergence of ordered structures through the local interactions of system components. Self-assembly is commonly observed in physical and chemical systems, where the components spontaneously organize into structured arrangements based on inherent properties such as molecular shape or charge interactions, ultimately reaching an equilibrium state.[1] Notable examples include the crystalline structures of snowflakes and the complex atomic arrangements in minerals.[2] Whereas, self-organization is prevalent in biological systems and results in patterns emerging from interactions among lower-level components without external direction, often occurring in far-from-equilibrium conditions.[1,3] Examples include the patterns on animal coats,[1] fish schools,[1] and bacterial swarms.[4]

Pattern formation is characterized by the non-homogeneous spatial distribution of the concentration of one or more chemical species. Reaction-diffusion (RD) patterns are a category of these formations, governed by the interplay between chemical reactions and the diffusion of species under non-equilibrium conditions.[5] RD systems can be described by combining Fick's second law with reaction rate equations to model the spatiotemporally repeating phenomena. The general equation is given by:

$$\frac{\partial c}{\partial t} = D\nabla^2 c + R(c) \tag{1.1}$$

where c, t, D, ∇^2, and R are the concentration of the chemical species, time, diffusion coefficient, Laplace operator, and reaction term, respectively.

Some well-known examples of RD systems include Turing patterns, Belousov-Zhabotinsky (BZ) reactions, and Liesegang patterns (LPs) (Figure 1.1). These systems gained significant attention following Alan Turing's ground-breaking 1953 paper.[6] He proposed a mathematical model describing how an initially uniform mixture containing diffusing, reactive activator, and inhibitor species can spontaneously break symmetry, leading to the formation of static spatiotemporal patterns.[4,6,7] The BZ reactions, discovered by Boris Belousov and later developed by Anatoly Zhabotinsky, exemplify oscillatory chemical reactions that create temporal and spatial patterns in a liquid medium.[8,9] This reaction has become an important model for understanding nonlinear dynamics and chemical kinetics. Lastly, LPs involve the inter-diffusion and co-precipitation typically between cations and anions in a hydrogel, leading to the form of spatiotemporally repeating patterns.[5]

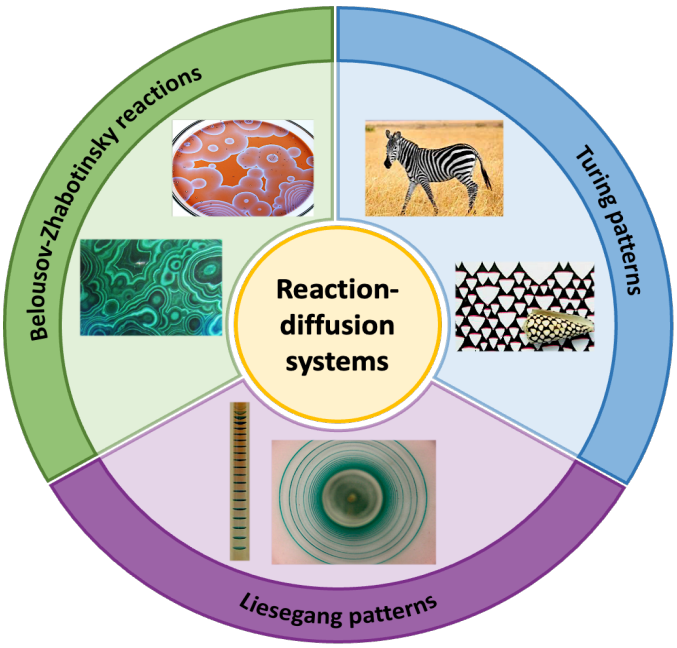

Figure 1.1. Illustrative examples of reaction-diffusion systems. Clockwise from top right: Turing patterns as seen on zebra stripes and mollusk shells,[6] Liesegang patterns of $Co(OH)_2$ within a Petri dish and test tube,[10] wave-like patterns on a malachite stone and the ferroin-malonic acid BZ reaction.[11]

1.1.1 Liesegang phenomenon

The Liesegang phenomenon, also known as periodic precipitation, is a famous example of RD systems, discovered in the late 19th century by the German chemist Raphael Edward Liesegang. He first observed this phenomenon when concentric ring of silver dichromate crystallites formed after a solution of silver nitrate was dropped onto a thin gelatin film containing potassium dichromate.[12,13] LPs typically emerge when an aqueous solution of an outer electrolyte (A) is layered onto a gel containing an inner electrolyte (B). The diffusion of the outer electrolyte into the gel medium triggers the spatial formation of precipitates (P), represented by the reaction:[5]

$$A\ (aq) + B\ (aq) \rightarrow P\ (s) \downarrow$$

In these experiments, the concentration of the outer electrolyte is generally several orders of magnitude greater than that of the inner electrolyte to ensure that pattern formation is primarily

governed by the diffusive flux of the outer electrolyte.[12] The resulting patterns manifest as periodic bands in test tubes (1D system), rings in a Petri dish (2D system), or even spherical shells in gel spheres (3D system).[5] Due to the simplicity of the underlying chemical principles, LPs have been observed across a broad range of systems involving metal ions such as Ag^{+}, Ca^{2+}, Cu^{2+}, Ba^{2+}, Pb^{2+}, Co^{3+}, and various counter-ions, including OH^{-}, HPO_4^{2-}, $Cr_2O_7^{2-}$, SO_4^{2-}, I^{-}, F^{-}.[9,14] Liesegang's seminal work has not only gained the interest of physicists and chemists but has also extended its influence to biologists, geologists, and mineralogists, reflecting its broad applied potential and theoretical relevance.[13]

1.1.2 Empirical laws and model of Liesegang phenomenon

To date, developing a comprehensive theoretical model for the Liesegang phenomenon remains a significant challenge. However, researchers have historically described the LPs using three empirical laws (Figure 1.2).

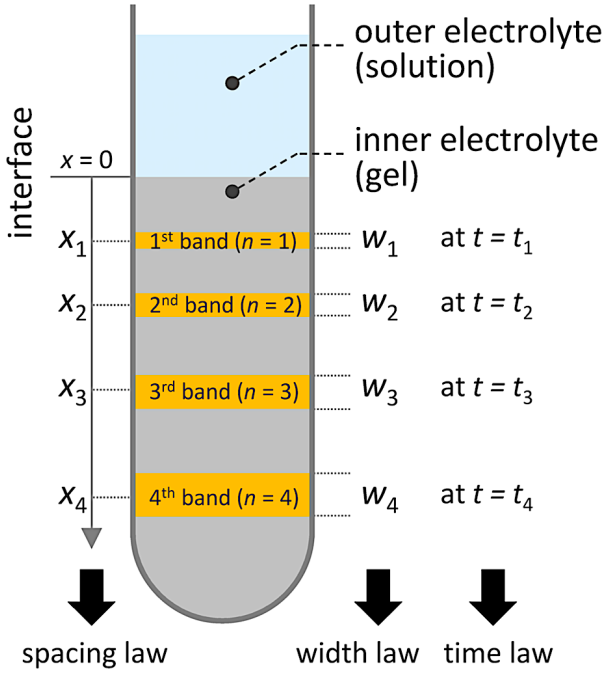

Figure 1.2. Schematic diagram of periodic precipitation and three empirical laws describing the Liesegang phenomenon. x = 0 is the liquid-gel interface. The x_n, w_n, and t_n denote the spacing, width, and time laws, respectively. Figure was adapted from [5].

(i) First, the space law as described by Jablczynski, where the spatially ordered Liesegang bands follow a geometric series:[15]

$$\rho_n = \frac{x_{n+1}}{x_n} \rightarrow p \tag{1.2}$$

where ρ, x_n, and p are the spacing ratio, distance of the n^{th} bands from the interface, and spacing coefficient, respectively. The ratio ρ approaches a constant p, which is typically $1 < p < 1.5$, as n becomes sufficiently large.[9] Moreover, the spacing between the bands $\Delta x_n \left(= \frac{x_{n+1}}{x_n}\right)$ increases as n increases; thus, the bands become more separated following the diffusion front.[5] Furthermore, the magnitude of p is highly dependent on experimental parameters, such as the concentration of the electrolyte,[10,16] concentration of the gel medium,[10,16] pH,[10,16] and the electric field.[10] Matalon and Packter later refined this understanding by relating the spacing coefficient to the initial concentrations of outer $[a_0]$ and inner $[b_0]$ electrolytes.[16] The equation is written as

$$p = F[b_0] + G\frac{[b_0]}{[a_0]} \tag{1.3}$$

where $F[b_0]$ and $G[b_0]$ are decreasing functions of $[b_0]$. In other words, p decreases linearly with increasing $[a_0]$ when $[b_0]$ is held constant (Figure 1.3).[17]

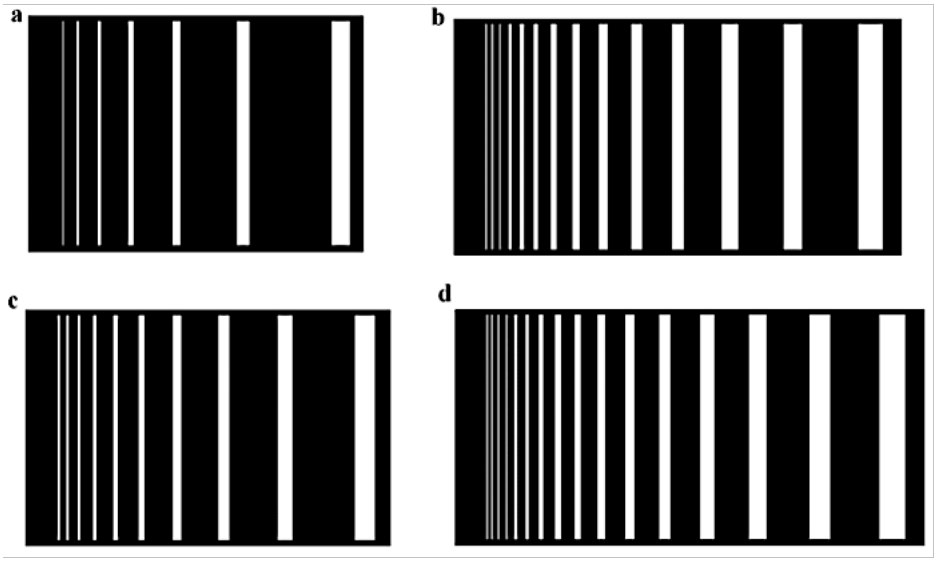

Figure 1.3. Simulated Liesegang patterns that align with the space law and Matalon-Packter law. The concentration of inner electrolyte, b_0 = 0.035 M and the concentration of outer electrolyte are (a) a_0 = 0.05 M, (b) a_0 = 0.09 M, (c) a_0 = 0.07 M, and (d) a_0 = 0.10 M. Figure was adapted from [17].

(ii) The time law was introduced by Morse and Pierce.[18] This law correlates the temporal dynamics to the spatial formation of the bands. It postulates that the position of a band, x_n, is proportional to the square root of time elapsed until its formation, t_n, expressed mathematically as

$$\frac{x_n}{\sqrt{t_n}} = q \tag{1.4}$$

This relationship highlights how the diffusive behavior of the outer electrolyte in the gel medium is stabilized over time, with the ratio between x_n and t_n approaching a constant q as n increases.[19]

(iii) Lastly, the width law focuses on the thickness of the bands, stating that the width of bands, w_n, increases linearly with x_n:

$$w_n = x_n^{\alpha} \tag{1.5}$$

with $\alpha > 0$.[17] Simply said, the width of precipitated bands increases at distances further from the liquid-gel interface.

Several theoretical models have been developed to explain LPs, one of which is the pre-nucleation model. It is also known as supersaturation theory, which was first proposed by William Ostwald.[12,20] This model posits that periodic precipitation is governed by a repeating process of supersaturation, nucleation, and depletion.[17] As illustrated in Figure 1.4, the process begins when the outer electrolyte A diffuses into the gel medium containing the inner electrolyte B, increasing the local ion concentrations to exceed the supersaturation threshold. This increase triggers the nucleation and growth of particles, forming a distinct precipitation band. Since the reaction is diffusion-limited, no further nucleation occurs at the band position due to the depletion of reactants around the nuclei and a subsequent decrease in local product concentration level as the reaction front moves further from the liquid-gel interface. When the supersaturation threshold of the product approaches the critical level again at the moving front, the process triggers the nucleation of another precipitation band. This repeating cycle of nucleation kinetics and diffusion transport results in the formation of LPs, which adhere to the scaling law.[21]

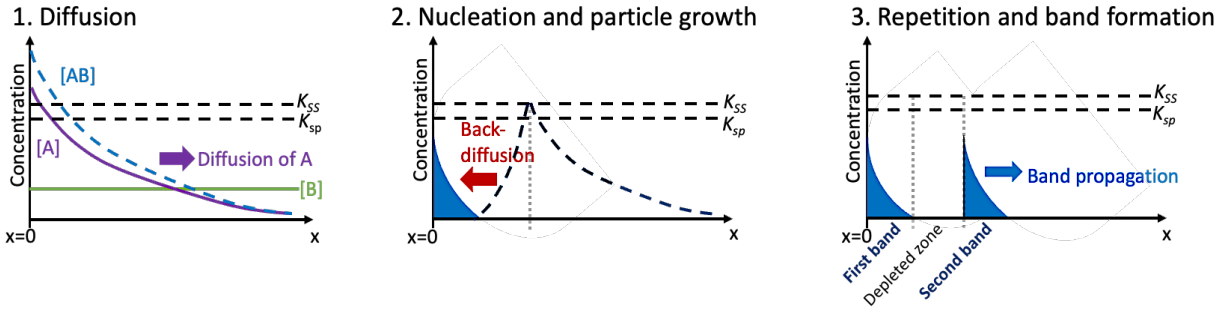

Figure 1.4. Pre-nucleation model of periodic precipitation. When outer electrolyte A reacts with inner electrolyte B (1), exceeding the supersaturation threshold ($[AB] > K_{ss}$), triggers the nucleation and particle growth to form the first precipitation band (2). The back-diffusion into the first band (2) creates a depleted zone. As diffusion continues, [A] once again reaches the K_{ss} at the moving front (2), initiating the formation of subsequent band (3).[5]

1.2 Crystallization in hydrogels

The use of hydrogels for single crystal growth has been extensively documented in the literature.[22] Hydrogels can be defined as a semi-solid, two-component systems that are rich in water.[22] Typically, hydrogels are classified into two categories: (1) physical gels, *e.g.*, agar, gelatin, and silk fibers, or (2) chemical gels, *e.g.*, sodium metasilicate (SMS) gel and polyacrylamide.[23] The gel plays a critical role in three-dimensional crystal growth by suppressing the sedimentation of crystals and convection currents, thus ensuring that crystallization is primarily driven by diffusion.[5,24]

Following the initial discovery of Liesegang rings of silver dichromate, various LP formations have been achieved using hydrogels, including agar,[24] gelatin,[10] SMS gels,[25] and 1,3:2,4-dibenzylidene-D-sorbitol (DBS) gels.[24] The Lewis structure of these gels are depicted in Figure 1.5.

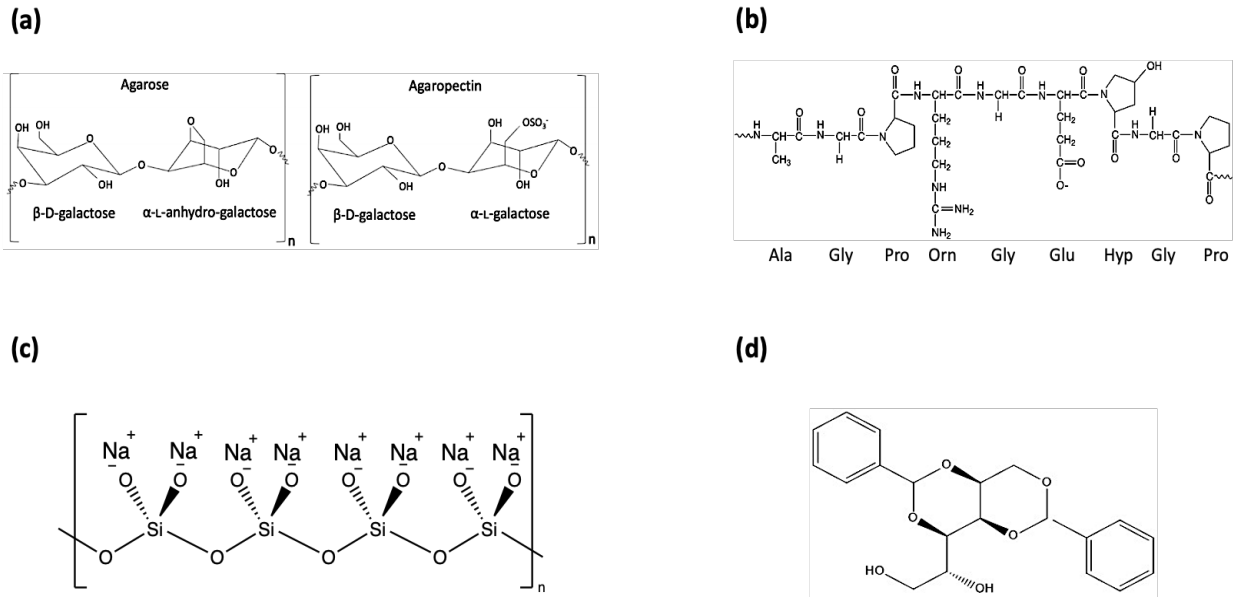

Figure 1.5. Lewis structures of (a) agar, (b) gelatin, (c) sodium metasilicate, and (d) 1,3:2,4-dibenzylidene-D-sorbitol gels.

Physical gels such as agar and gelatin are primarily composed of polysaccharides, *e.g.*, agarose and agaropectin, as well as amino acid polymers. The network within these gels is formed through hydrogen bonding or hydrophobic interactions along the polymer chains, which can be induced by changes in temperature and/or pH.[23] This gelation process is typically reversible. In contrast, the 3D network structure of an SMS gel results from irreversible polymerization between Si-O linkages (Figure 1.5 (c)).[23] In our research, we selected agar as the gel medium due to its inertness, making it an ideal candidate for RD crystallization processes.

To set the optimum conditions for the crystallization process, there are several variables that need to be considered in their preparation, such as the concentration of inner and outer electrolytes, concentration of gel, additives, pH, temperature, and the geometry of the system.[26,27]

1.3 Chirality in chemistry: Historical perspectives and modern implications

In the realm of chemistry and molecular sciences, chirality emerges as a fundamental concept, pivotal in understanding the asymmetrical nature of many molecular structures and their behaviors. The term 'chirality' was proposed by Lord Kelvin, derived from the Greek work 'cheir', meaning 'hand'. He defined chirality as the property of an object that makes it non-superimposable on its mirror image.[28,29] This molecular asymmetry significantly influences the physical and chemical properties of substances.

Chirality is not simply a curiosity of molecular geometry but a critical feature with far reaching implications in biology and pharmacology.[29] Chirality is ubiquitous in nature and fundamental to the function and structure of many biological molecules. For instance, amino acids, the building blocks of proteins (except for glycine), are chiral, existing exclusively in L-form (Figure 1.6 a).[30] This chiral purity is essential for the proper structure and function of proteins, which are crucial for biological processes. Similarly, the double helix of DNA, the repository of genetic information, exhibits chirality with its chiral D-sugars and right-handed helical structure (Figure 1.6 b).[31,32] In pharmaceuticals, the significance of molecular chirality is profound; different enantiomers of the same molecule can have vastly different effects on the human body. This phenomenon was tragically highlighted in the case of Thalidomide (Figure 1.6 c), where the (*R*)-enantiomer acted as a sedative, while the (*S*)-enantiomer caused severe congenital disabilities.[33] Consequently, the pharmaceutical industry places significant emphasis on developing enantiomerically pure compounds, underscoring the critical role of chirality in drug design and safety.

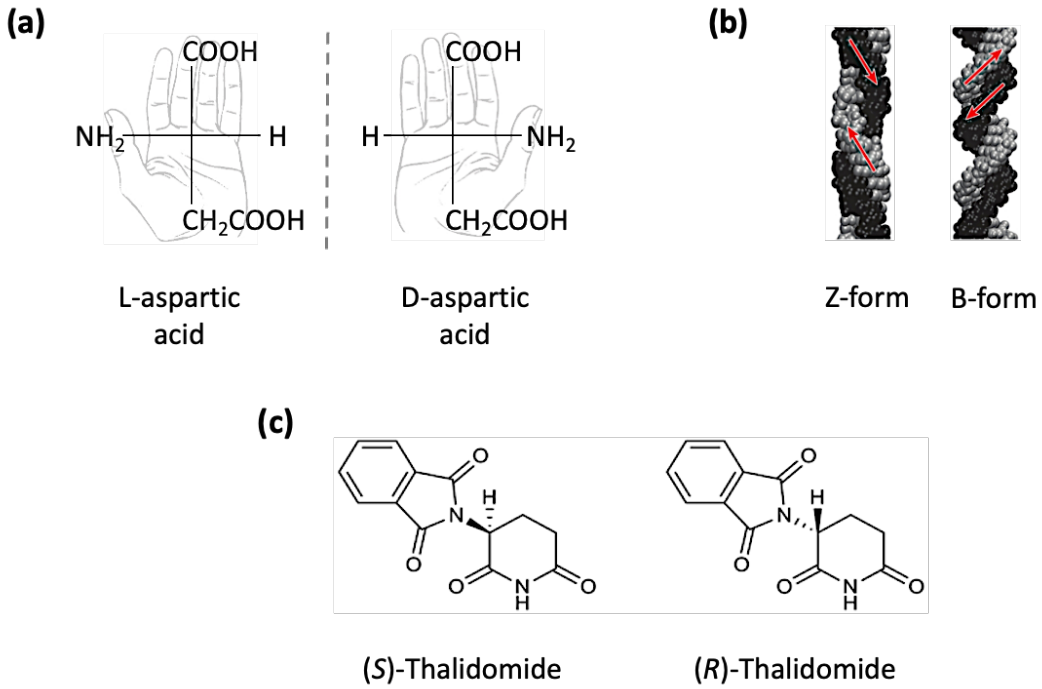

Figure 1.6. (a) Amino acid. L-aspartic acid (left) and D-aspartic acid (right). (b) Left-handed Z-form (left) and right-handed B-form (right) DNA double helices. B-form DNA was proposed by Watson and Crick.[31,32] The red arrows indicate the direction of the helix. (c) (*S*)-Thalidomide (left) can cause teratogenic side effects, while (*R*)-Thalidomide (right) acts as a sedative.[33]

1.4 Chiral resolution

Building on the foundational principles of chirality, the process of separating enantiomers, known as chiral resolution, is essential in chemical industry. There are three main approaches used to obtain enantiopure compounds, with our research primarily focusing on resolution *via* crystallization (Figure 1.7).[33]

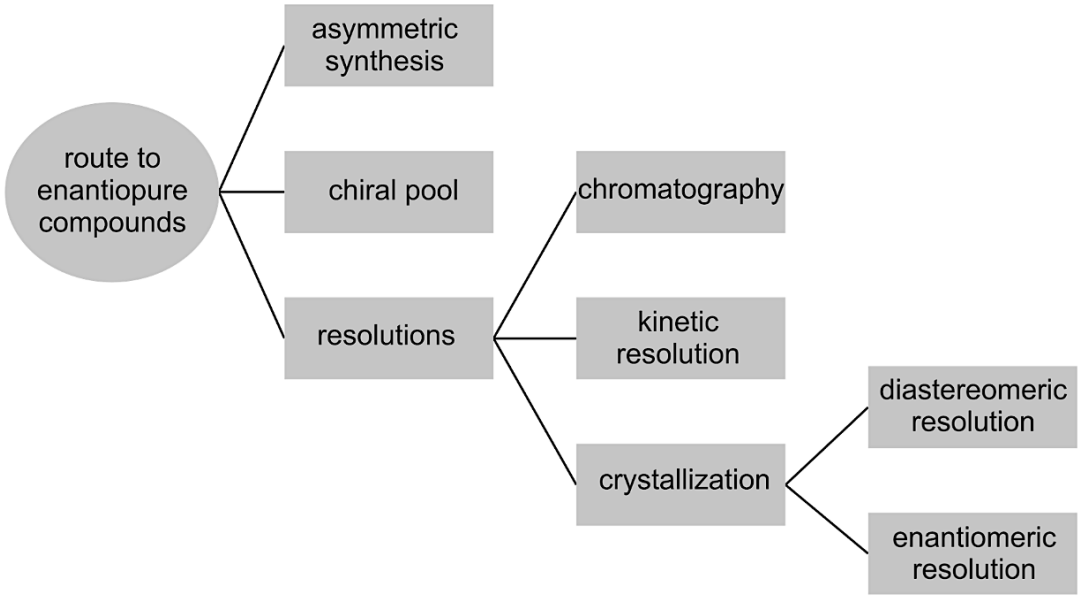

Figure 1.7. Schematic representation of three routes leading to enantiopure compounds. Figure was adapted from [33].

1.4.1 Crystallographic studies

Self-assembly from crystallization is a fundamental process whereby molecules spontaneously organize into a crystalline structure, typically driven by the minimization of free energy within the system.[34] During crystallization, individual molecules bind through non-covalent interactions, such as hydrogen bonding, metal coordination, hydrophobic forces, van der Waals forces, and electrostatic effects.[1] This ordered arrangement results in the formation of a unit cell that extends over macroscopic distances, manifesting as crystals with distinct shape and symmetries.[2] Each unit cell is defined by six lattice parameters (Fig. 1.8 a), with three parameters specifying the lengths of the edges (a, b, c*)* and the other three outlining the angles (α, β, γ) between these edges. These parameters establish the three-dimensional structure of the crystal lattice in relation to the Cartesian axes (x, y, z). Additionally, crystals can be classified into 7 crystal systems based on their

lattice parameters and symmetry: triclinic, monoclinic, orthorhombic, tetragonal, trigonal, hexagonal, and cubic (Fig. 1.8 b).

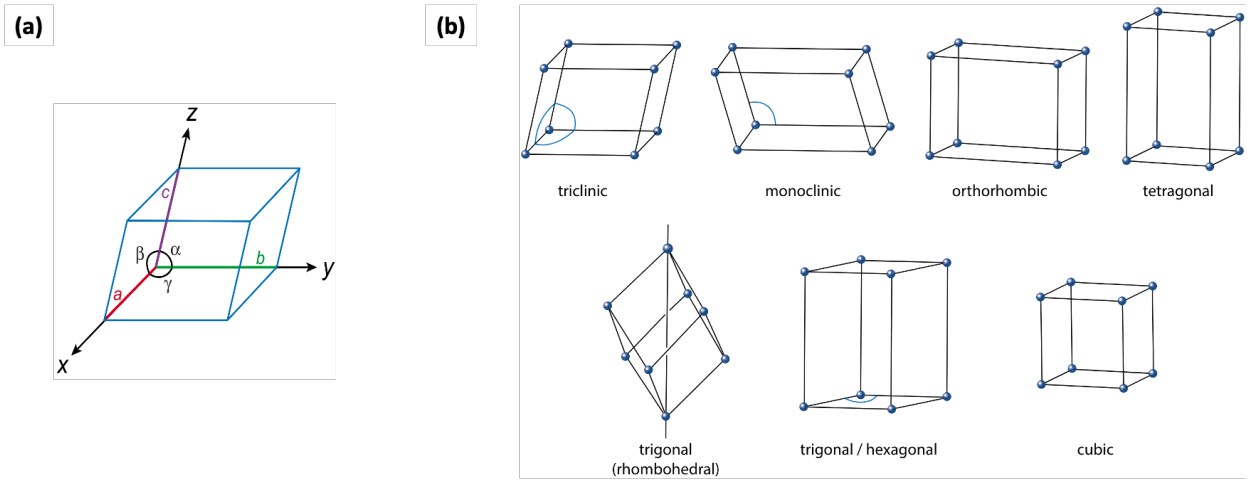

Figure 1.8. (a) The unit cell is defined by six lattice parameters: three edge lengths a, b, and c oriented along with x, y, and z axis, respectively, and the angles between these edges, α (between b and c), β (between a and c), and γ (between a and b). (b) The seven crystal systems, which differ in their axial lengths and interaxial angles. Figure adapted from [2].

Crystallographic studies utilize Miller indices (h,k,l), which represent the orientation of crystal planes based on their intercepts with the axes in a Cartesian axes (Fig. 1.9).[35] A negative Miller index is denoted with a bar above the number or a minus sign, *e.g.* ($\overline{1}$ or -1). The relationship between Miller indices and Cartesian planes is critical as these indices provide a direct link to the geometry of the crystal and the orientation of each plane in a three-dimensional space.[2]

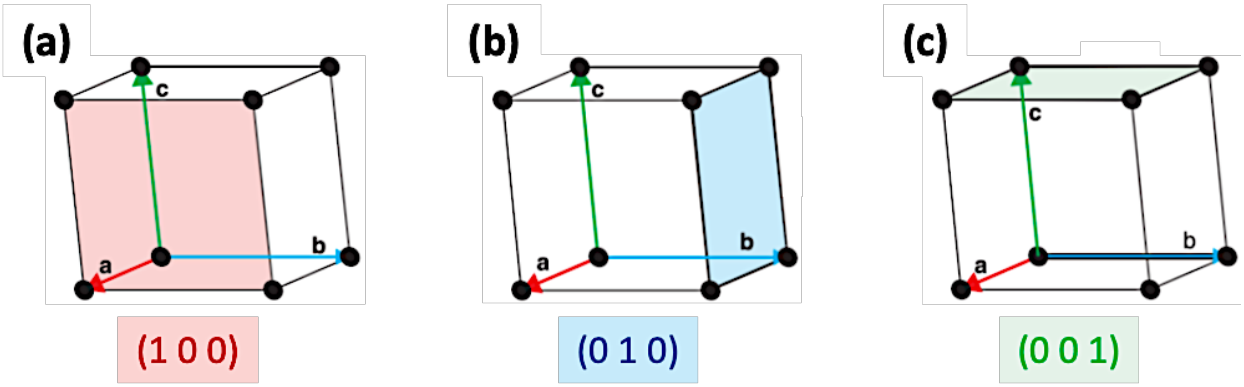

Figure 1.9. Miller indices of lattice planes: the plane perpendicular to the (a) a-axis, represented by (1 0 0), (b) b-axis, represented by (0 1 0), and (c) c-axis, represented by (0 0 1).[35]

Space groups, which combine translational and point symmetries, further enhance the understanding of crystal structure. These groups specify symmetry operations, such as rotations, reflections, inversions, and screw axes, that correspond to the lattice parameters of the crystal.[2] The *International Tables for Crystallography* documented 230 unique space groups in three-dimensions, each vital for analyzing crystal structures and determining their physical properties.[2] Space group symbols always begin with a letter indicating the type of lattice (*e.g.*, *P* for primitive), followed by symbols that represent viewing directions.[2]

1.4.2 Conglomerate crystallizations

When a racemic mixture crystallizes, the chiral molecules can form either racemic or conglomerate crystals (Figure 1.10). Racemic crystals contain both enantiomers in an ordered arrangement within the crystal lattice at an equimolar ratio. Whereas conglomerates crystals have only one enantiomer within each individual crystal. Conglomerate crystallization is also known as spontaneous resolution because the racemic mixture separates into a physical mixture of enantiomorphic crystals.[33]

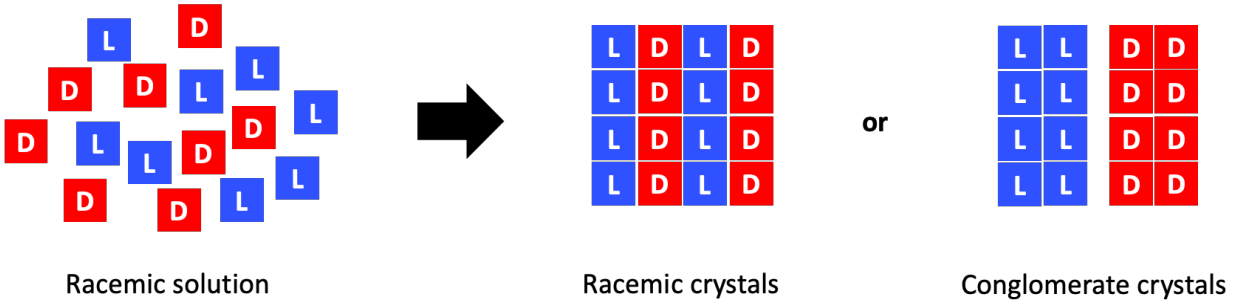

Figure 1.10. Enantiomers from racemic solution can either crystallize as racemic crystals or conglomerate crystals.[36] L = L-enantiomer; D = D-enantiomer

Within the various symmetry operations (refer to section 1.4.1), the 230 crystallographic space groups can be divided into two sets: (i) 165 space groups that generate achiral crystal structures and (ii) 65 space groups that generate chiral crystal structures.[37] These 65 space groups are called non-centrosymmetric Sohncke space groups, which lack mirror or glide planes, and inversion centers. The Sohncke space groups are further divided into two subgroups: (i) 22 space groups (11 enantiomorphic pairs), where each space group in the pair represents one of two possible chiral forms (*e.g.* $P4_1$ is enantiomorphic with $P4_3$) and (ii) 43 achiral space groups that still result in chiral crystals because they do not have a mirror plane or inversion center (*e.g.*, $P2_1$).[37] Notably, conglomerate crystals must crystallize in one of these 65 space groups. Statical analyses have shown that only about 5-10% of racemates crystallize as conglomerates, yet these conglomerates are particularly suitable for the resolution of enantiomers into enantiopure solid phases.[33,38]

One of the earliest documented examples of conglomerate crystallization involved sodium ammonium tartrate tetrahydrate, achiral molecule known for forming chiral conglomerate crystals. These crystals belong to the orthorhombic Sohncke space group, $P2_12_12$.[39] In 1848, Louis Pasteur pioneered the separation of enantiomers by manually sorting these asymmetric crystals under a

microscope. He identified the enantiomers by observing a small hemihedral (*h*) facet on the crystals (Figure 1.11) that were asymmetric, and selectively separated them with tweezers based on their handedness.[40–42] This meticulous process marked the first documented resolution of a racemic mixture, thereby setting a precedent for chiral resolution.

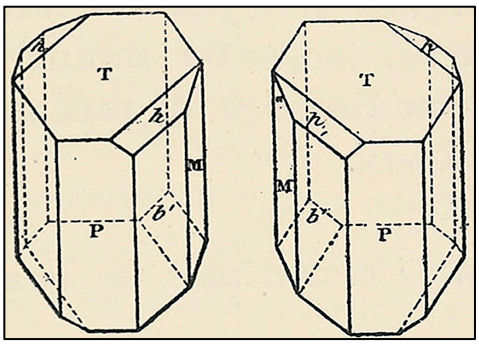

Figure 1.11. Sodium ammonium tartrate tetrahydrate enantiomorphic crystals. The hemihedral facets are labeled with *h*.[42]

In 1898, Kipping and Pope demonstrated the overall stochastic chiral crystallization sodium chlorate ($NaClO_3$).[43] Although $NaClO_3$ is achiral in solution, it crystallizes into homochiral *l*- or *d*-crystals belonging to the $P2_13$ space group (another Sohncke space group).[44] By introducing chiral seed crystals into saturated solutions, Kipping and Pope demonstrated that subsequent crystal growth occurs through secondary nucleation, leading to the formation of crystals that exhibit the handedness of the seed crystals.[43]

Relevant to our research, Petrova and Swift demonstrated that the statistical distribution of $NaClO_3$ crystals could be significantly biased from the expected racemic distribution when grown in agarose gel media. They obtained 95 *l*-enantiomorphic crystals and 159 *d*-enantiomorphic crystals when growing crystals in 6 ºC aqueous agarose gels (0.5 %wt/wt). As illustrated in Fig. 1.5 a, agarose, a major component of agar, consists of repeating units of chiral sugars (β-D-

galactose and α-L-anhydro-galactose) that confer chirality to its structure. This inherent chirality of the agarose is believed to influence the orientation and alignment of the crystallizing $NaClO_3$, favoring the formation of *d*-$NaClO_3$ over *l*-$NaClO_3$. [45] This symmetry breaking illustrates how the characteristics of the medium, can significantly influence chiral outcomes in crystal growth.

Among the twenty proteinogenic amino acids, four exhibit the property of forming conglomerates upon crystallization, including aspartic acid (Asp)[38,46], glutamic acid (Glu)[36,38], asparagine monohydrate (Asn•H_2O)[36] , and threonine (Thr)[36,47] (Figure 1.12). Additionally, certain amino acid salts demonstrate the ability to be resolved *via* crystallization. For example, Glu readily forms conglomerates with NH_4^+, Mg^{2+}, Zn^{2+}, and HCl salts, while proline does so with lithium and zinc salts.[36] Asn and Thr can naturally crystallize as conglomerates,[36] Asp is noted for forming conglomerates as 2-methylaspartic acid,[36] and phenylalanine has been reported to form conglomerates with 2,5-xylenesulfonic acid.[48]

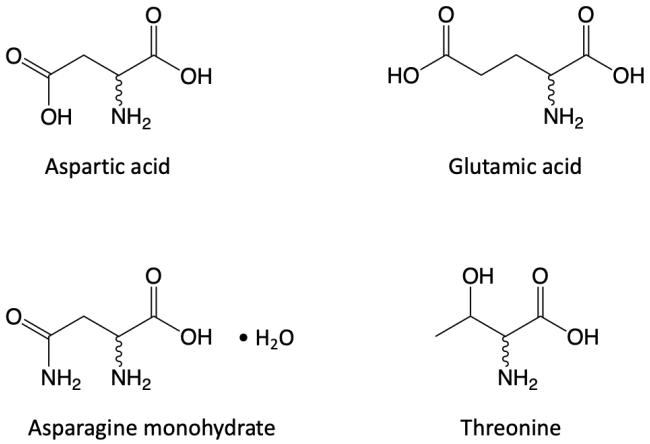

Figure 1.12. Four amino acids that crystallize as conglomerates.

Aspartic acid was chosen for this study due to its versatile coordination capabilities as demonstrated by Imaz *et al*.[49] and Wu *et al*.[50]. Asp possesses three potential donor sites (one amine

and two carboxyl groups), that allow it to act as a mono-, bi-, or tri-dentate bridging ligand with metal ions across various pH ranges.[51,52] Specifically, the α- and β-carboxylic acid moieties have a pKa of 2.09 and 3.86, respectively. This pKa configuration suggests that both carboxyl groups are fully deprotonated and available for metal binding in the environments with a pH > 4.0, facilitating Asp coordinating as a tridentate ligand.[51] Even at lower pH values, the amine group, with a pKa of 9.82, can participate in coordination due to its strong electron-donor character and the stability imparted by the formation of chelate rings. The influence of pH on the available coordination sites of Asp is outlined in Fig. 1.13.

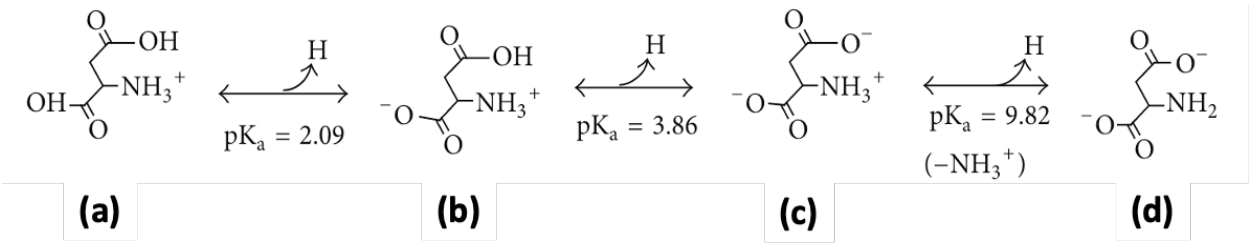

Figure 1.13. pH-dependent coordination behavior of Aspartic acid. (a) in strong acid (pH < 1), the net charge is +1, (b) around pH 3, the net charge is 0, (c) between pH 6 to 8, the net charge is -1, and (d) in strong alkali (pH > 11), the net charge is -2. Figure adapted from [51].

1.4.3. Coordination polymers

1.4.3.1 A brief history of coordination polymers

The journey of coordination polymers (CPs) began serendipitously in the 18th century when Heinrich Diesbach, a German colormaker, accidentally discovered a method for making the blue pigment known as Prussian Blue.[53] The structural complexity of this pigment puzzled scientists for nearly two centuries[54] until it was discovered to be a CP featuring a 3D cubic lattice constructed from heterometallic centers and cyanide ligands, forming a mixed-valence polycyanide compound (Fig. 1.14) distinguished by its strong blue color.[55,56] This example highlights the challenges faced

by crystal engineers in predicting structures resulting from the supramolecular assembly of metal ions and/or organic molecules.

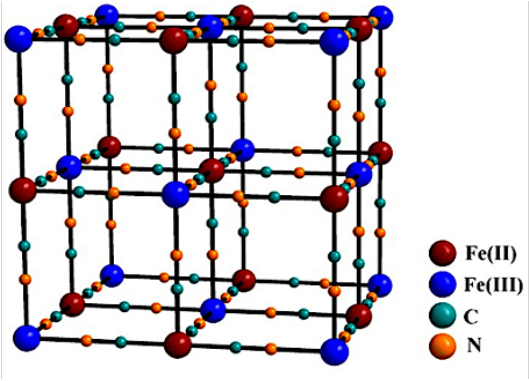

Figure 1.14. Idealized structure of Prussian Blue where octahedral sites of Fe(II) and Fe(III) ions are interconnected by cyanide ligands, forming a 3D cubic array. Figure adapted from [56].

A significant breakthrough in understanding and designing CPs emerged in the 1980s. Prof. Lehn who introduced Supramolecular Chemistry,[57] along with subsequent studies by Prof. Desiraju[58] and Prof. Etter[59] on molecular organization *via* hydrogen bonds, laid the groundwork for predicting CP structures. Prof. Wells further refined the approach by describing crystal structures as networks composed of points with specific geometries like octahedra and tetrahedra, connected by lines.[60] Building on Wells' foundational work, in 1989, Robson *et al*. applied this network approach to the design of CPs.[61] They demonstrated that CPs could be constructed by linking metal ions with specific valencies, such as tetrahedral or octahedral, using rod-like organic ligands as connectors.[62] This method allowed for the deliberate engineering of materials with unique properties, including porosity and catalytic activity,[62] thereby pioneering new possibilities in chemistry, materials science, and nanotechnology.

1.4.3.2 What defines a coordination polymer?

Coordination polymers are versatile metal-ligand compounds that form infinite arrays along one-, two-, or three-dimensions (1D, 2D or 3D) through coordination bonds (Fig.1.15).[63,64] These polymers are synthesized using a variety of techniques including hydro-/solvo-thermal methods,[65,66] microwave-assisted synthesis,[67] mechanochemistry,[68] sonochemistry,[69] and gel growth.[24] Transition metals, which are commonly used in CP synthesis, exhibit predictable coordination geometries typically ranging from two to six coordinate points (Fig. 1.16),[70] while rare earth metals can accommodate up to ten.[71]

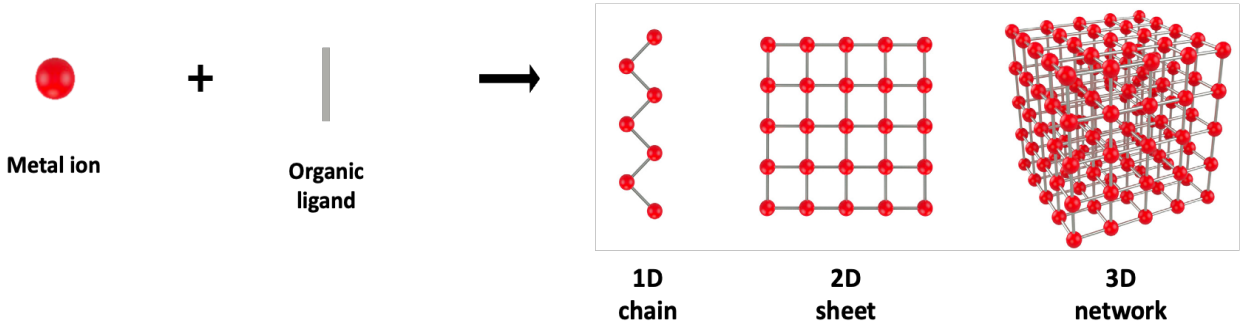

Figure 1.15. Schematic representation of the assembly of CPs showing 1D, 2D, and 3D structures.[64]

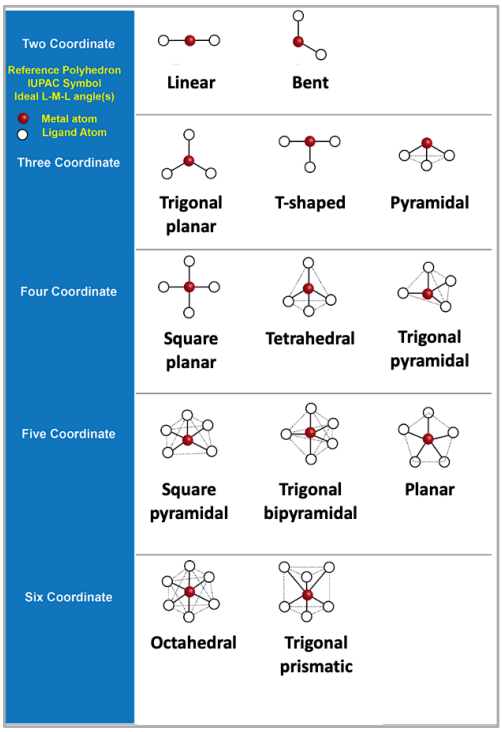

Figure 1.16. Typical coordination geometries of transition metals (ranging from two- to six-coordinate) and their bond angles. Figure adapted from [70].

The architecture of a CP is determined by the coordination geometry of metal ions, the ligand selection, and the binding mode(s) of the ligand. Other factors such as hydrogen bonds, van der Waals interactions, and π-π stacking interactions also play crucial roles in defining the final structures of CPs. This methodological diversity, coupled with the vast array of possible combinations of metal coordination geometries and organic ligands allows for the creation of vast array of CPs with varying compositions and topologies. These range from simple and common 1D linear structure[49,50] to complex 3D constructs (*e.g.*, metal-organic frameworks (MOFs)).

MOFs are distinguished as a subclass of CPs, noted for their highly ordered, porous structures that can be meticulously tuned to specific pore sizes and functionalities. These frameworks are capable of hosting guest molecules within their cavities, with surface areas that can reach up to

6000 m^2/g.[64,72] The ability to finely control pore characteristics enhances their utility in application such as gas storage and separation, and in catalysis, where high surface area is required.[64,73,74]

Building on the structural advantages of MOFs, the incorporation of luminescent lanthanide ions (Ln^{3+}) into these frameworks introduces additional functional capabilities. Ln-based MOFs employ chromophoric ligands to act as antennae, effectively sensitizing the Ln^{3+} excited state through energy transfer processes.[75] This results in functional systems with their prolonged emission from the UV-Vis to NIR ranges, enhancing their application potential.[76,77]

The remarkable versatility of CPs opens up extensive possibilities for designing materials that integrate multiple properties, making them ideally suited for diverse applications, including sensing,[64] gas storage,[73] luminescence,[78] catalysis,[74] magnetism,[79] and drug delivery.[80]

1.4.3.3 Amino acid-based coordination polymers

As mentioned above, the selection of the organic ligand is very important to determine the final characteristics, properties, and applications of CPs. Conventional coordination polymerizations often employ rigid ligands that contain carboxylate, imidazolate, or pyridyl moieties, and frequently coupled with aromatic groups or polyaromatic spacers.[72] Although these rigid aromatic ligands are effective in engineering the desired structural properties, they may pose environmental and health risks due to their potential toxicity.[63]

In recent years, the focus of CP research has evolved towards green chemistry approaches, particularly through the use of naturally-occurring biomolecules, including amino acids, nucleobases, and carbohydrates.[81] Employing these biomolecules in the construction of CPs offers several advantages: (1) they are cost-effective and readily accessible, (2) they are inherently chiral, (3) their diverse structures and metal-binding sites enhance the flexibility and rigidity, influencing

the functional properties and structural diversity of CPs, (4) they possess intrinsic self-assembly properties that facilitate structural and functional control,[49,50,82] and (5) they are environmental-friendly and biocompatible.[83]

Amino acids, as biodegradable and naturally occurring molecules, offer an alternative to traditional synthetic ligands. The integration of amino acids into CPs not only aligns with environmental sustainability goals but also opens up new pathways for creating biocompatible materials.[63,81] These amino acid-based CPs harness the intrinsic properties of amino acids, to develop materials that are potentially more functional due to the unique interactions of amino acid side chains with metal ions.

In general, amino acids form a five-membered glycinate chelate ring involving the carboxyl (O) and amino (N) groups, which facilitate the formation of metal-amino acid chelates (Fig. 1.17 b).[84] Additionally, the side chain R groups of amino acids introduce further metal-binding capabilities. For example, the β-carboxylate groups of aspartic and glutamic acids, the imidazole group of histidine, the phenyl ring of tyrosine, the thiol of cysteine, or the thioether group of methionine (Fig. 1.17 c), serve as additional metal-binding sites, promoting the bridging of metal ions and enhancing the dimensionality of metal-amino acid-based CPs.[84,85] Although these binding groups can lead to more complex structures, amino acids predominantly form 1D CPs due to the coordination numbers directing growth along one dimension.[49,50,86,87]

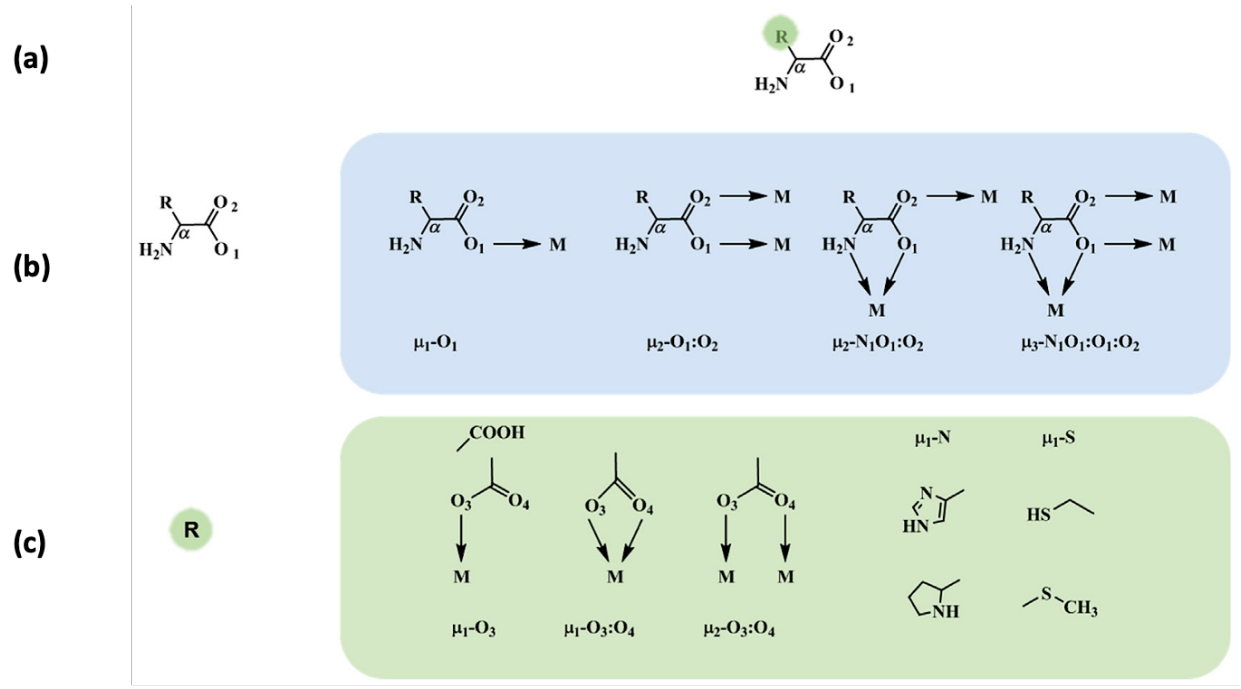

Figure 1.17. Schematic representation of (a) the common structure of a natural amino acid, (b) the potential coordination modes that metal ions can adopt with the amino group and carboxyl group, and (c) various side chain R groups that amino acids can exhibit. 'μ' denotes the bridging ligand, with the subscript number 'x' after μ indicating the ligand coordination with 'x' central atoms (μx). Figure adapted from [85].

By selecting chiral amino acids as building blocks, researchers can tailor the chirality of coordination polymers, leading to the formation of materials with specific molecular orientations and functionalities. For instance, Imaz *et al.*[49] demonstrated the diffusion controlled growth of 1D CuAsp nanofibers by slowly adding an aqueous solution of $Cu(NO_3)_2 \cdot 6H_2O$ to an ethanol/water mixture containing deprotonated L- or D-Asp (Fig. 1.18 a and b). These nanofibers formed at the liquid-liquid interface, range between 100 – 200 nm in diameter and extend up to 1 cm in lengths (Fig. 1.18 c and d). Conversely, rapidly adding $Cu(NO_3)_2 \cdot 6H_2O$ to the deprotonated L- or D-Asp solutions under stirring yielded shorter nanofibers. At higher concentrations of 70 mM, a blue aqueous gel formed, consisting of long, intertwined nanofibers that maintained structural stability

(Fig. 1.19). The chirality of L- and D-CuAsp nanofibers was analyzed using solid-state CD, where the L-form exhibited a positive Cotton effect and the D-form showed a negative Cotton effect at *ca*. 745 nm, with both showing opposite Cotton effects at a crossing wavelength of 637 nm, near the absorption band of Cu(II) complexes (Fig. 1.18 e).

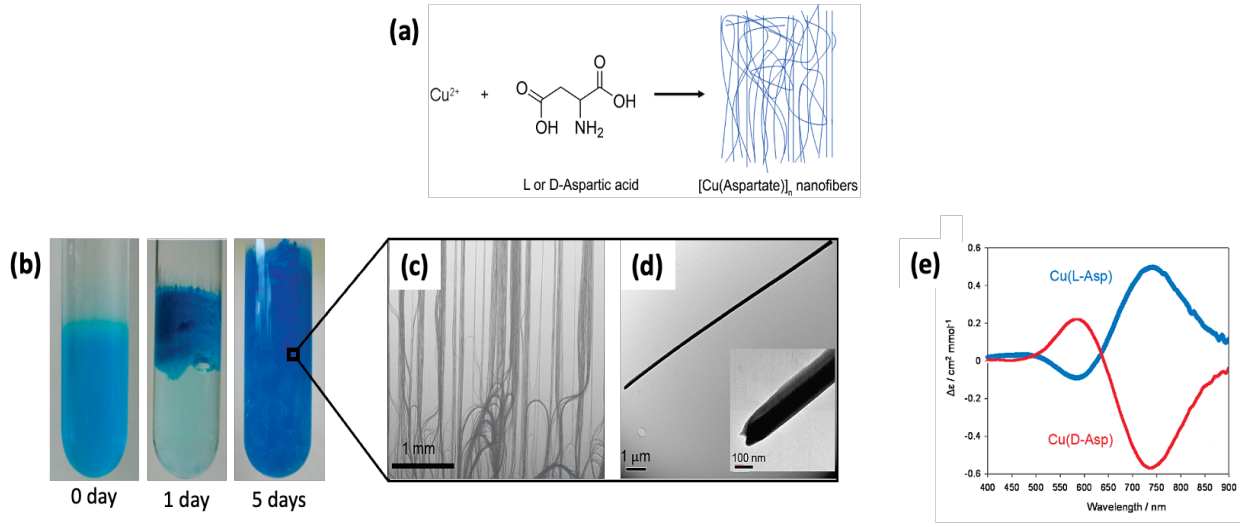

Figure 1.18. (a) Schematic representation of the coordination polymerization of CuAsp nanofibers. (b) Sequential images showing the diffusion process and formation of the nanofibers. (c) Optical microscope and (d) TEM images of the nanofibers. (e) Solid-state CD spectra of L-CuAsp (blue line) and D-CuAsp (red line) nanofibers. Figure adapted from [49].

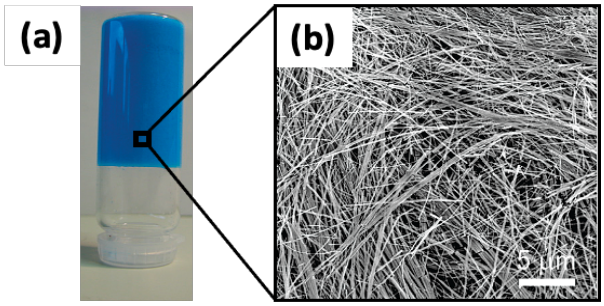

Figure 1.19. (a) Photograph of the CuAsp gel formed at 70 mM of $Cu(NO_3)_2 \cdot 6H_2O$ and deprotonated L- or D-Asp. (b) FESEM image of the CuAsp gel. Figure adapted from [49].

Glutamic acid, another amino acid with a β-carboxylate side chain, has also been shown to form CPs with Cu^{2+} ions in aqueous solutions at room temperature. Pu *et al*.[87] demonstrated that nanofibers could be generated through the self-assembly of DL-Glu with various copper salts, including $Cu(NO_3)_2$, $CuSO_4$ or $CuCl_2$ (Fig. 1.20 b, e, and h). These nanofibers range between 50 – 80 nm in diameters and up to several micrometers in length. While nanofibers formed consistently across different anions (NO_3^-, SO_4^{2-}, and Cl^-), those formed in the presence of SO_4^{2-} were notably wider, likely due to the larger ionic radius and divalent nature of SO_4^{2-}. Interestingly, when Cu^{2+} was mixed with homochiral Glu, nanoparticles of various morphologies were produced (Fig. 1.20), highlighting the chirality of Glu plays a crucial role in guiding the assembly of the final products. These CuGlu nanofibers have shown significant efficacy in removing anionic dyes from water and exhibiting antibacterial properties, underscoring their potential environmental and biomedical applications.

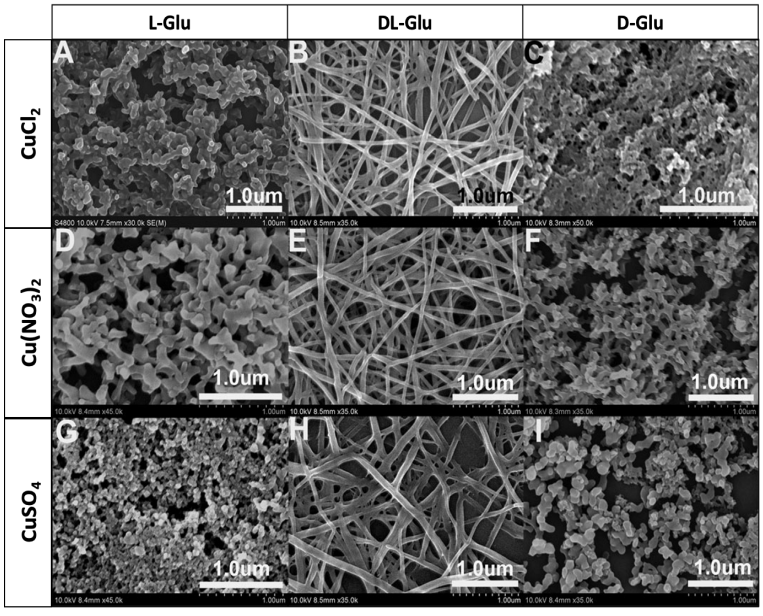

Figure 1.20. SEM images demonstrating the coordination of L-Glu, DL-Glu, and D-Glu with copper salts: $CuCl_2$ (A, B, C), $Cu(NO_3)_2$ (D, E, F), and $CuSO_4$ (G, H, I). Figure adapted from [87].

In 2015, Wu *et al*.[50] explored the impact of stereochemistry on the self-assembly rates of CuAsp, CuGlu, and copper aminoadipate (CuAmi). These 1D nanofibers were formed through coordination between copper sulfate and Asp, Glu, and 2-aminoadipic acid (Ami). At a low reactant concentration (14 mM), nanofibers were obtained from the coordination of Cu^{2+} with homochiral Asp and Ami, as well as DL-Glu. When the concentrations of Cu^{2+} and DL-Glu were increased to 35 mM, the self-assembly evolved from 1D nanofibers into 2D microsheets. At an even higher concentration (70 mM), homochiral CuAsp gels formed more rapidly than the DL-CuAsp gel (Fig 1.21 a and b). Meanwhile, at 280 mM, DL-CuGlu formed an aqueous gel (Fig. 1.21 d and e), although this gel was less stable than CuAsp gels and easily disassembled upon agitation due to insufficient bridging between the microsheets. Notably, no gelation occurred with either homochiral or racemic Ami (Fig. 1.21 g and h), which was attributed to the inability of the short nanofibers to bridge effectively. These observations highlight how both chirality and the carbon chain length of the amino acid (Fig. 1.21) significantly influence the assembly process.

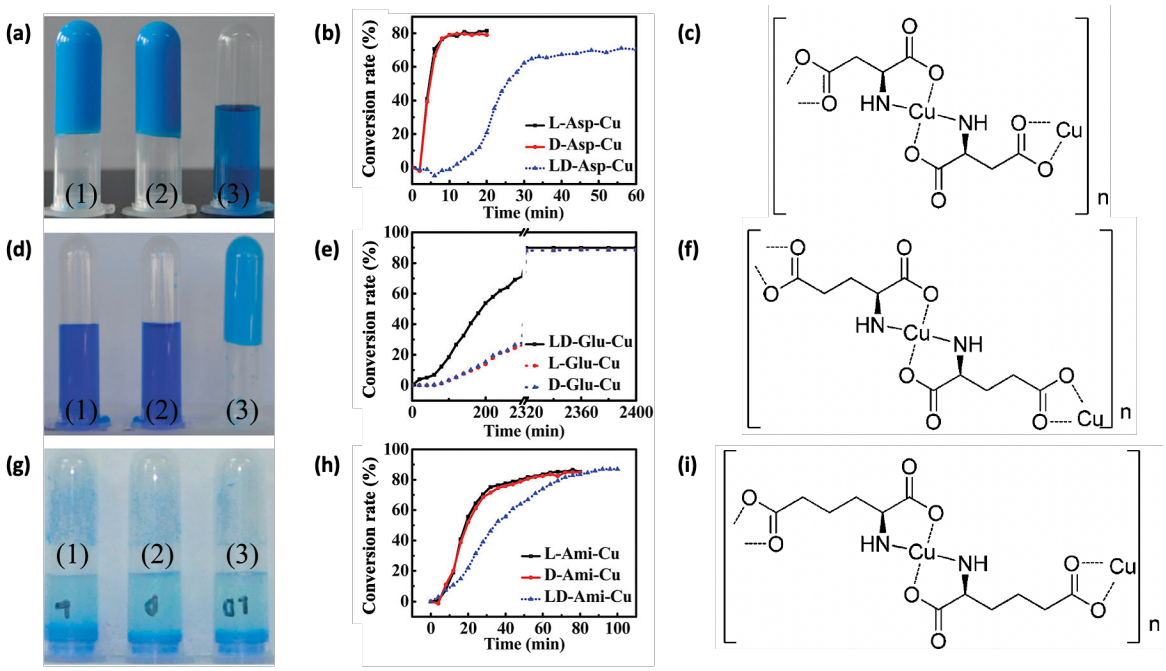

Figure 1.21. Self-assembly of 70 mM CuSO4 with L-, D-, and DL-Asp (a1, a2, a3), and 280 mM Cu^{2+} with L-, D-, and DL-Glu (d1, d2, d3), and L-, D-, and DL-Ami (g1, g2, g3), respectively. (b, e, h) show the time-dependent conversion rates of the assemblies at reactant concentrations of 14 mM for Asp and 280 mM for Glu and Ami. The corresponding 1D polymeric structures of (c) L-CuAsp, (f) L-CuGlu, and (i) L-CuAmi. Figure adapted from [50].

In their characterization of these metal-biomolecule nanofibers, Wu *et al*. performed X-ray photoelectron spectroscopy (XPS), thermogravimetric analysis (TGA), Fourier transform infrared spectroscopy (FTIR), PXRD, and solid-state CD. The XPS analysis (Fig. 1.22 a) and TGA revealed a stoichiometric 1:1 ratio of nitrogen to copper, indicating precise coordination between Cu^{2+} ions and amino groups in the amino acids. The FTIR spectra (Fig. 1.22 b) showed distinct asymmetric and symmetric COO- stretching bands at 1620/1580 cm^{-1} and 1400 cm^{-1}, respectively, along with N-H and -OH stretching bands in the 2500-3700 cm^{-1} region, indicative of hydrogen bonding. These results suggest that the nanofibers evolved from the 1D $[Cu(II)(amino\ acid)]_n$ polymer chains into short nanofibrils through inter-ligand hydrogen interactions.[49,87] PXRD (Fig. 1.22 c)

confirmed the crystallinity of these structures, while solid-state CD (Fig. 1.22 d) displayed the chiral nature of the nanofibers, with both L- and D-forms exhibiting opposite Cotton effects.[50]

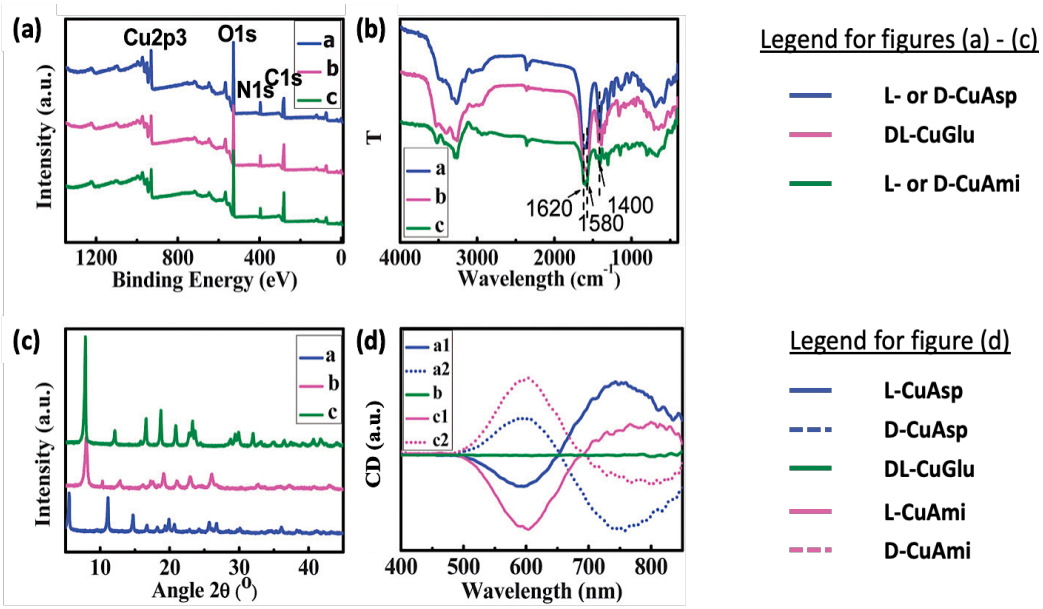

Figure 1.22. (a)XPS spectra, (b) FTIR spectra, (c) X-ray powder diffraction patterns and (d) solid-state CD spectra of L- and D-CuAsp, DL-CuGlu, and L- and D-CuAmi nanofibers. Figure adapted from [50].

Ma *et al*. demonstrated a simple precipitation-assisted method for synthesizing L- or D-terbium aspartate (TbAsp) nanocrystals, which form tetrahedral structures with a planar hexagonal network.[76] This study highlighted distinct luminescent responses from Tb^{3+} ions when coordinated with L- and D-Asp (Fig. 1.23 c). Surprisingly, the D-Asp formed a more stable coordination polymer with Tb^{3+} ions, characterized by higher absorption, longer luminescence lifetime, and increased quantum yields. The authors observed that replacing D-Asp with by L-Asp distorted the D-TbAsp tetrahedron, enlarging the lattice spacing from 0.66 nm to 0.70 nm, as depicted in Fig. 1.23 a and b. This alteration led to a decreased in structural stability of the TbAsp coordination polymers.

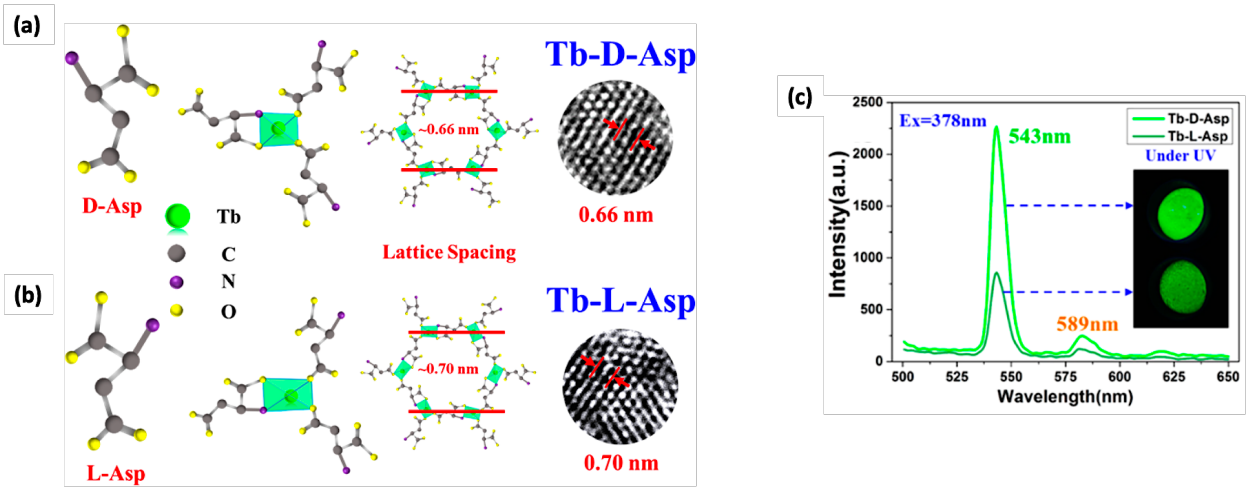

Figure 1.23. Schematic illustrations showing and the structural differences between (a) D-TbAsp and (b) L-TbAsp nanocrystals. (c) Emission spectra of D-TbAsp and L-TbAsp at 378 nm excitation. Inset: Fluorescence of D-TbAsp and L-TbAsp nanocrystals under UV light. Figure adapted from [76].

Li *et al.*[86] investigated the self-assembly of Ag(I)-cysteine (Cys) complexes using L-, D- and DL-Cys. When Ag(I) coordinated with L-Cys, it resulted in the formation of right-handed helical nanobelts (Fig. 1.24 a), while D-Cys produced left-handed helices (Fig. 1.24 d). These nanobelts were 10 μm in length with a helical pitch of 2.2 μm (Fig. 1.24 b and e) and varied in width from 100 – 200 nm across their twisted and stretched segments (Fig. 1.24 c and f). CD spectra revealed distinct Cotton effects at 352 nm and 424 nm for Ag(I)/L-Cys nanobelts, indicating chiral properties, while Ag(I)/D-Cys exhibited mirror-image optical properties (Fig. 1.24 g). However, when DL-Cys was used, it led to the formation of 2D nanosheets (Fig. 1.24 h), with the CD spectrum showing no chiral signal, suggesting an equimolar ratio of L- and D-Cys. Density functional theory simulation supported these findings by showing that homochiral Cys breaks the translation equivalence in the Ag(I)/Cys lattice, leading to specific twist accumulation and the formation of asymmetric Ag-S bonds that discriminate between the intralayer directions. Conversely, DL-Cys

facilitated the formation of uniform Ag-S bonds, resulting in 2D networks devoid of intralayer asymmetry and twist accumulation. These “flat” Ag-S slabs were then interconnected through weak interlayer O–H•••O hydrogen bonds to form final structures. This study highlights the critical role of amino acid chirality in directing the structural assembly and morphological characteristics of metal-amino acid CPs.

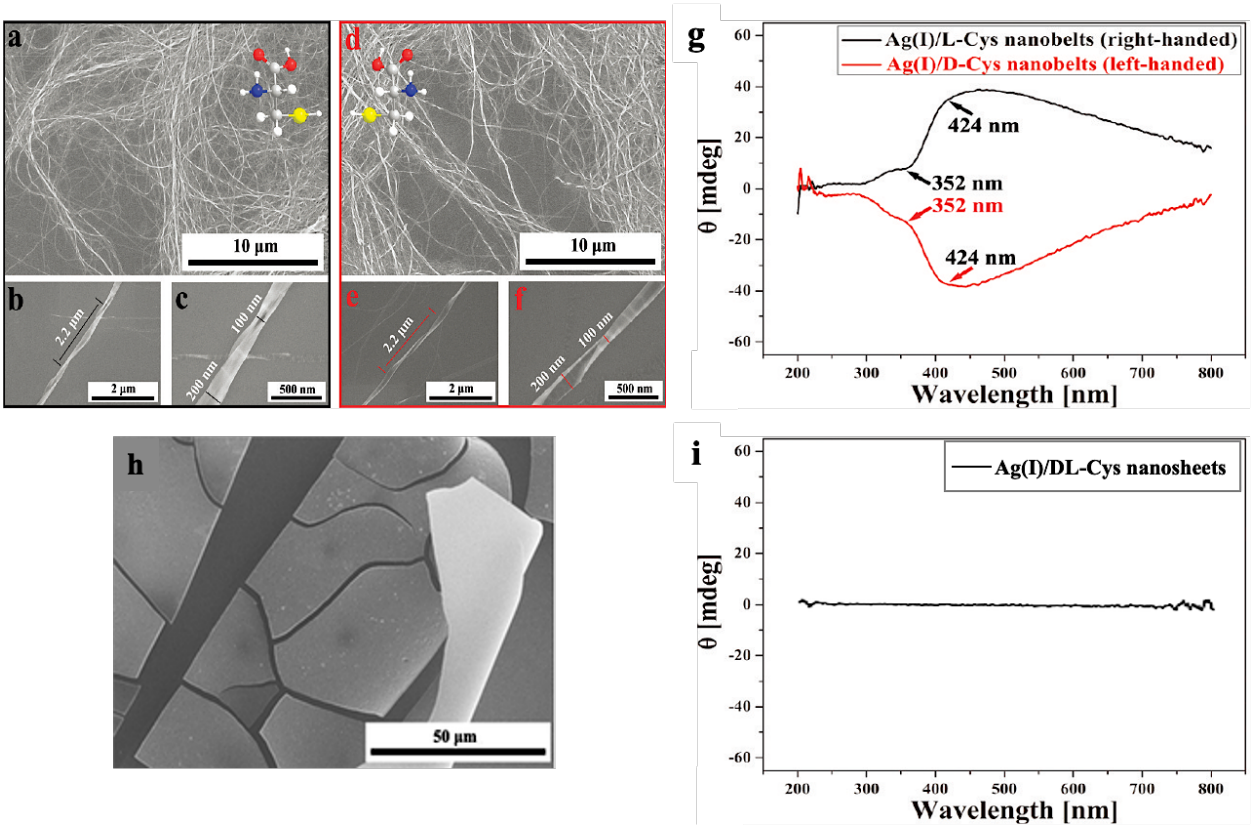

Figure 1.24. Self-assembly of Ag(I)-Cys nanostructures. (a, b, c) SEM images at various magnifications of Ag(I)/L-Cys nanobelts showing right-handed helical structures. (d, e, f) SEM images at similar scales of Ag(I)/D-Cys nanobelts illustrating left-handed helical structures. (h) SEM image of the 2D nanosheets formed by Ag(I)/DL-Cys. CD spectra (g) display distinct Cotton effects at 352 nm and 424 nm for Ag(I)/L-Cys (black line) and Ag(I)/D-Cys (red line) nanobelts. In contrast, the CD spectrum (i) of Ag(I)/DL-Cys nanosheets shows an absence of Cotton effects. Figures adapted from [86].

1.4.4 Revisiting chiral resolution: Preferential crystallization with the *'rule of reversal'*

Chiral coordination polymers play a pivotal as additives in the resolution of enantiomers through crystallization. Despite significant advances in asymmetric synthesis, preferential crystallization (PC) remains an economically viable method for obtaining high-purity enantiomers.[88] This technique takes advantage of differences in crystallization kinetics between enantiomers and is commonly applied to conglomerate-forming systems.[89–91]

In the 1960s, Harada *et al*.[92,93] successfully resolved DL-Asp using homochiral amino acid–copper complexes, including L-Glu, L-Pro, L- and D-Ala. This approach enabled the crystallization of D-CuAsp in the presence of L-amino acid-copper complexes (Fig. 1.25 a), and *vice versa*.[93] Harada *et al*. invoked this phenomenon as the stereoselective ligand exchange.[92] The resolution process was significantly influenced by both the concentration of reactants and the mole ratio of homochiral amino acid to DL-Asp.When the mole ratio of the chiral amino acid to DL-Asp was less than 1, the second crop of crystals remained the same configuration as the first crop. However, when the mole ratio was equal or greater than 1, the configuration of the second crop reverses relative to the first crop.[93]

This crystallization method, later termed preferential crystallization with 'rule of reversal' by Addadi *et al*., utilizes tailor-made additives (TMAs) that structurally resemble the crystallizing parent molecule.[89] As shown in Fig. 1.25 b, L' additives selectively adsorb on the surface of L-enantiomer crystals, influencing their nucleation and growth. Addadi *et al*. demonstrated the effectiveness of TMAs in controlling crystal morphology, facilitating the kinetic resolution of racemates, and guiding self-assembly processes at the air-water interface.[89,94,95] For example, crystals grown from (*RS*)-Glu•HCl with 1-3% wt/wt of *S*-lysine additive form as plate-like (*R*)-Glu•HCl crystals covered by a crystalline powder of (*S*)-Glu•HCl. In addition, kinetic resolution

of the (*RS*)-Glu•HCl was induced by higher concentrations of *S*-lysine additive (up to 10% wt/wt) by inhibiting the growth of (*S*)-Glu•HCl and promotes the preferential crystallization of (*R*)-Glu•HCl. This technique was applied similarly to other racemic systems, such as (*RS*)-Asn•H_2O and (*RS*)-threonine.[95]

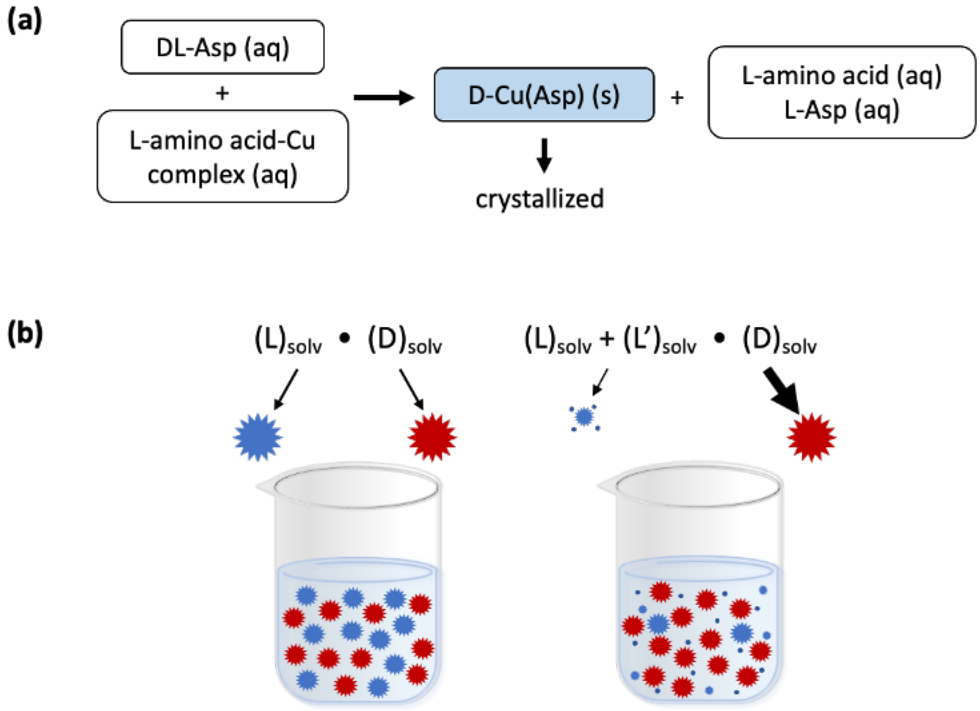

Figure 1.25. (a) Preliminary mechanism of resolving DL-Asp conglomerates in the presence of L-amino acid-copper complex.[52] (b) Schematic describing preferential crystallization with 'rule of reversal' - (left) without additives, (right) with L' additives.

1.5 Characterization techniques

1.5.1 X-Ray diffraction (XRD)

X-ray Diffraction (XRD) is non-destructive analytical technique widely used to characterize crystalline materials. The technique involves directing X-rays towards a material and analyzing the intensity and angles of the X-rays scattered by the internal structure of the material.[96] The

fundamental principle governing XRD is Bragg's Law, which described the conditions for constructive interference of X-rays scattered by parallel atomic planes within a crystal,[96,97] expressed as:

$$n\lambda = 2d\ sin\theta \tag{1.6}$$

where n is an integer, λ is the wavelength of the X-rays, d is the spacing between the crystal planes, and θ is the angle of incidence. This law is essential for interpreting XRD patterns, which are instrumental in determining the atomic or molecular structure of the material.[97]

The interaction of X-rays with the atomic planes in a crystal generates constructive and destructive interference. Constructive interference occurs when X-rays scattered from successive atomic planes are in phase, reinforcing one another and producing high-intensity peaks known as Bragg peaks. These peaks provide essential information about the spacing between crystal planes and the crystallographic orientation of the sample. Conversely, destructive interference arises when scattered X-rays are out of phase, leading to a reduction or cancellation of intensity, which is typically seen in the valleys between the Bragg peaks in the XRD pattern.[97,98] The interplay between these interferences allows researchers to deduce the ordered atomic arrangement characteristic of crystalline materials, thus providing insights into the properties and behaviors of the materials.

Single-crystal X-ray diffraction (SCXRD) is used to obtain detailed atomic structures from single crystals, typically ranged from 100 μm to 200 μm.[99] Powder X-ray diffraction (PXRD) is used when the sample is only available in powdered form or when it is difficult to grow a large single crystal, with crystalline size between 0.1 μm and 1.0 μm.[99]

XRD has a wide range of applications, including the comparison of Bragg peak positions and intensities to the standard reference patterns from databases such as Cambridge Crystallographic Data Centre (CCDC). The Scherrer equation is also commonly applied to estimate particle sizes from peak broadening observed in the diffraction patterns; a decrease in crystallite size can result in peak broadening.[97] For polycrystalline materials, crystallographic orientation is significant, as preferred orientation can influence material properties. When crystals are not randomly oriented, certain planes may not meet the diffraction condition, resulting in fewer reflections and affecting the intensity of Bragg peaks.[96,97,99]

1.5.2 Solid-state circular dichroism (CD)

Solid-state circular dichroism is a powerful tool for studying the optical and chiral properties of materials in solid forms. This methos measures the difference in absorption of left- and right-circularly polarized light, revealing molecular asymmetry and chiral configurations within the sample. A fundamental phenomenon observed in CD spectroscopy is the Cotton effect, named after Aimé Auguste Cotton in the late 19th century.[100,101] This effect is characterized by the simultaneous appearance of circular dichroism (and ellipticity) alongside an optical rotation dispersion curve within the absorption region of an optically active compound.[102] Each Cotton effect curve comprises two extremes: a geometric maximum termed a “peak” and a geometric minimum called a “trough,” with the zero crossing point denoting the maximum absorption. For instance, the positive Cotton effect manifests when optical rotation increases as the wavelength decreases, placing the peak at the longer wavelength (Fig. 1.26). In contrast, the negative Cotton effect is noted by its trough appearing at the longer wavelength.[102]

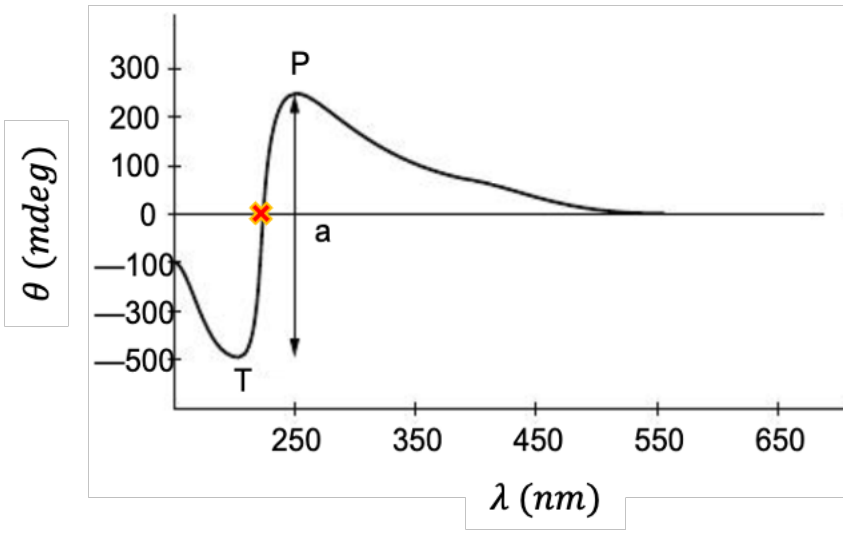

Figure 1.26. CD spectrum showing positive Cotton effect, featured by the peak (P) appears at longer a wavelength. The red "x" marks the zero crossing point, indicating the maximum absorption. 'T' and 'a' denote the trough and amplitude, respectively. Figure adapted from [102].

Two main techniques for analyzing sample in solid-state CD are the Nujol mull and the KBr pellet method. Both approaches present unique advantages and limitations often influenced by factors such as absorption flattening,[103] light scattering, [103] turbidity,[104] and sample inhomogeneity.[104] Variations in absorption and shifts in absorption peaks, commonly observed during CD spectrum acquisition, are attributed to light scattering and reflections due to varied in size distribution of crystals.[104] Minimizing these challenges can be achieved by optimizing sample preparation and concentration, repeating experiments, and positioning the sample closer to the detector to reduce light scattering.[105]

The Nujol mull method is advantageous for its rapid sample preparation and typically generates lower HT (photomultiplier) voltage owing to the transparency and homogeneity of the sample. However, reproducing spectra can be challenging.[106] Practice is required to achieve a homogeneous sample with a uniform crystal size distribution and reproducible thickness between quartz windows.

Conversely, the KBr pellet method generally performs well across most systems, especially when transparent pellets are obtained.[105] Moreover, the crystal size distribution tends to be consistent with the KBr matrix as the powder mixture is ground together. Nevertheless, KBr is hygroscopic which can lead to rapid clouding upon exposure to air, thereby increasing light scattering. Inhomogeneity within KBr pellets also poses challenges, as achieving a homogeneous mixture of solids is difficult and can result in signal variations.

1.6 Scope of thesis

This thesis explores the coordination polymerization of homochiral (L- and D-) and racemic (DL-) copper aspartate (CuAsp) within a reaction-diffusion framework (RDF) and investigates the spatiotemporal resolution of DL-aspartate using homochiral proline (Pro)-copper complexes as tailor-made additives (TMAs). The research aims to understand the self-organization mechanisms, crystallization patterns, and chiral resolution processes of copper-based coordination polymers (CPs) in agar gel under far-from-equilibrium conditions. Through these investigations, the study contributes to a broader understanding of hierarchical crystallization in coordination systems and proposes innovative strategies for enantioselective separation.

Chapter 1 provides an overview of the theoretical foundation for the research. It introduces the key concepts of self-organization and pattern formation, with a focus on the Liesegang phenomenon and reaction-diffusion systems. The role of hydrogels in crystallization and the importance of chirality in chemistry are also discussed. Special attention is given to chiral resolution through preferential crystallization with the 'rule of reversal,' which forms the experimental basis for the research.

Chapter 2 focuses on the coordination polymerization of L-, D-, and DL- CuAsp in 1D and 2D agar gel systems *via* reaction-diffusion system. The research explores how supersaturation gradients in agar gel environments drive self-organization, influencing nucleation, growth, and the hierarchical pattern formation. Characterization methods such as circular dichroism (CD) spectroscopy, powder X-ray diffraction (PXRD), and scanning electron microscopy (SEM) are employed to characterize the resulting coordination polymers. A key focus is on achieving chiral resolution of DL-aspartate in 1D and 2D agar gel systems by applying homochiral Pro-copper complexes as TMAs. The study explores how the chiral additives, in accordance with the 'rule of reversal,' guide the formation of enantiomeric CuAsp polymers and influence spatial crystallization patterns across concentration gradients. The interaction between chiral additives and the gel matrix are analyzed to understand the chirality-switching behavior.

Chapter 3 summarizes the research findings and provides recommendations for future work, including further exploration of different gel matrices, applying the RDF to other amino acid-metal complexes, and conducting the conglomerate crystallization of L-, D-, and DL-CuAsp by applying electric field.

Chapter 2

2.1 Introduction

Coordination polymers (CPs) encompass a versatile class of metal-ligand coordination compounds capable of forming one-, two-, or three-dimensional structures.[63,107] The inherent flexibility of CPs to integrate a variety of metals and ligands allows for the creation of materials with a wide range of applications, including magnetic,[79] gas adsorption,[73] catalysis,[74] luminescence,[78] and drug delivery.[80] Recent advancements have focused on the design and construction of chiral CPs, not only for their complex architectures, which offer new insights into chiral topology, but also for their potential in applications such as enantioselective separation and asymmetric catalysis.[63,108] However, the ideal enantiopure ligand should be readily accessible, inexpensive, environmentally friendly, and exhibit versatile coordination behaviour.[63] Thus, the strategic design and selection of chiral ligands are critical for developing multifunctional chiral CPs.

Biomolecules such as amino acids, nucleobases, and saccharides present considerable potential as eco-friendly organic ligands.[81] Employing these biomolecules in the construction of CPs offers several advantages: (1) they are cost-effective and readily accessible, (2) they are inherently chiral, (3) their diverse structures and metal-binding sites enhance the flexibility and rigidity, influencing the functional properties and structural diversity of CPs, (4) they possess intrinsic self-assembly properties that facilitate structural and functional control,[49,50,82] and (5) they are biodegradable and biocompatible.[83] Amino acids, in particular, have garnered significant attention due to their efficient self-assembly with metal ions.[49,50,82] Their characteristic amino, carboxylate, and functional group-containing side chains render them ideal for complexation with metal ions.[65,84] Several research groups have demonstrated the fabrication of a series of 1D nanostructures such

as nanofibers,[49,50,109] nanowires,[110] nanobelts,[86] and nanorods[82] from metal-amino acid assemblies. For example, Imaz *et al*. successfully prepared CuAsp nanofibers by mixing a Cu^{2+} solution with a water/ethanol mixture containing deprotonated L- or D-Asp. Similarly, Pu *et al*. and Wu *et al*. demonstrated the self-assembly of CuGlu,[50,87] CuAsp,[50] and CuAmi[50] at room temperature. Their studies revealed that crystallization is driven by coordination between deprotonated amino acid and Cu^{2+} metal ions in a proposed square planar coordination geometry. Furthermore, amino acid chirality clearly influences supramolecular self-assembly.[50,87]

Chiral resolution remains a critical requirement in the pharmaceutical and food industries, where enantiopure products are essential.[111] Various techniques have been developed to achieve resolution of conglomerate crystalline systems,[90,112–115] with preferential crystallization (PC) being particularly notable for its ability to separate racemic mixtures in a single step by seeding the preferred enantiomer into a supersaturated solution.[91] Pioneering work by Kaoru Harada demonstrated the successful separation of DL-Asp, DL-Glu, and DL-Asn using homochiral amino acid-copper complexes.[92,93,116,117] However, the mechanism of resolution remained unclear until the 1980s when Addadi and colleagues proposed a concept called the "rule of reversal",[89] which clarified that enantiomers crystallize preferentially in an opposite configuration using TMAs. The TMAs are structurally similar to solute molecules, enabling selective adsorption and binding to specific growth sites and thus influencing nucleation and crystal growth.[89,90,118,119] This rule provides a framework for understanding Harada's works. More recently, Kongsamai *et al*. explored the effects of D-Asp and D-Glu on resolving DL-Asn•H_2O,[120] while Gou *et al*. and Zou *et al*. obtained higher product yields and purity of (*S*)-mandelic acid and L-norvaline, respectively, with PC using TMAs.[121,122] It is important to note that, to date, these studies have been exclusively conducted in solution.

The RDF incorporates diffusion, crystal nucleation, and growth, resulting in self-organized spatiotemporal patterns.[24] Within RDF, precipitates form as the outer electrolyte solution (reactant A) diffuses into a gel medium containing the inner electrolyte (reactant B). The concentration of the outer electrolyte is significantly higher than that of the inner, establishing a concentration gradient that dictates pattern formation.[5] As a result, smaller crystals are formed near the liquid-gel interface due to high supersaturation, whereas larger crystals are obtained at the diffusion front because the crystal growth is dominating.[24] Typically, the gel used for crystal growth is a hydrogel, consisting of up to 97% water. The gels are formed by loosely interconnected polymers that create a three-dimensional network with high porosity.[123] This network prevents crystal sedimentation and suppresses convection, thus effectively trapping crystals at the site of reaction.[24]

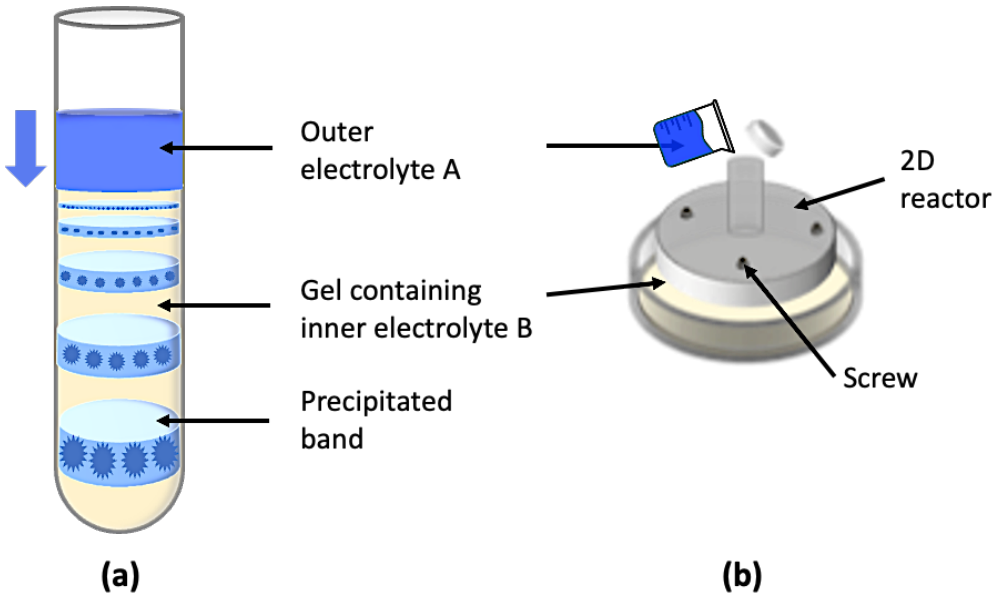

Figure 2.1. Schematic diagrams of reaction-diffusion framework for CuAsp coordination polymers. (a) 1D system – Illustration of a higher concentration copper solution diffusing into a gel containing a lower concentration of deprotonated DL-Asp, leading to the formation of periodic precipitation of CuAsp spherulites. (b) 2D system – Depicts a Petri dish coupled with a customized 2D reactor, where a copper solution is added through a central tube onto an evenly spread gel. The thickness of the gel is adjustable using three screws.

Inspired by Imaz's[49] and Harada's work[93] and the intricacies of RDF, we explored the chiral resolution of DL-Asp using homochiral Pro in both 1D (test tubes) and 2D (Petri dish) agar gel systems (Fig. 2.1). By diffusing a higher concentration of homochiral Pro-copper solution into a gel containing a lower concentration of deprotonated DL-Asp, a periodic precipitation of CuAsp polymers was observed. The resulting CuAsp polymers displayed a size gradient across different zones, a result of uniform diffusion, nucleation, and crystal growth processes. Furthermore, the CuAsp polymers exhibited spherulitic morphology, a phenomenon typically associated with the crystallization of sparingly soluble salts from highly supersaturated solutions in gel media.[122] Solid-state CD and PXRD analyses confirmed the chirality and crystallinity of the CuAsp coordination polymers, respectively. Overall, we established a method that aligns with the "rule of reversal" which can provide valuable insights into the spatiotemporal resolution of CuAsp enantiomers.

2.2 Experimental section

2.2.1 Materials

All chemical reagents, L-aspartic acid (from Aldrich Chemical Company), D-aspartic acid (from Alfa Aesar), DL-aspartic acid, L-proline, D-proline (from TCI America), BD™ Difco™ Agar (from Fisher Scientific), sodium hydroxide (from BDH Reagents and Chemicals), and copper nitrate trihydrate (from Thermo Scientific Chemicals), were used without further purification. All electrolyte solutions and hydrogels were freshly prepared using Millipore water (18.2 mΩ). Glass test tubes with 20 mm × 125 mm and Petri dishes with 150 mm × 15 mm were used.

2.2.2 Preparation procedures

2.2.2.1 Coordination polymerization of homochiral and racemic CuAsp in agar gels in 1D system

CuAsp coordination polymers were synthesized in test tubes containing both inner and outer electrolytes. Initially, the inner gel solution was prepared by dissolving 0.6 g (1% wt/wt) agar powder in 54 mL of water, heating, and stirring until completely dissolved. The agar gel was then cooled to 60 ºC. Concurrently, a solution of deprotonated L-, D-, or DL-Asp was prepared by dissolving 0.3993 g (3 mmol) of Asp and 0.24 g (6 mmol) of NaOH in water (6 mL). This solution was then added to the cooled agar gel and stirred for 5 minutes. The mixture was carefully transferred to test tubes, covered, and left to solidify fully. The final concentration of the inner electrolyte was 50 mM Asp and 100 mM NaOH, filling each tube with a total gel volume of 18 mL. The outer electrolyte, composed of copper nitrate trihydrate ($Cu(NO_3)_2 \cdot 3H_2O$) 1.4496 g (6 mmol, 300 mM), was dissolved in water (20 mL) and carefully layered over the gel using a glass Pasteur pipette. The test tubes were sealed with parafilm and left undisturbed to facilitate the controlled diffusion of electrolytes and the formation of distinctive blue spherulitic crystals.

The CuAsp spherulites were collected after the diffusion process was completed. The agar gel was carefully extracted and segmented into different zones using a spatula. Each zone underwent 3-5 washes in hot water to effectively separate the spherulites from the agar gel matrix. The spherulites were then transferred to Corning® 15 mL centrifuge tubes and isolated by centrifugation at 450 xg for 5 minutes, using IEC clinical CL bench-model centrifuge equipped with a Rotor 809 (radius = 12.7 cm). Finally, the spherulites were dried overnight in a 60 ºC oven.

2.2.2.2 Chiral separation of racemic Asp using homochiral Pro-copper complexes in 1D system

The inner electrolyte, consisting of 1% wt/wt agar and deprotonated DL-Asp, was prepared as described in *section 2.2.2.1*. The outer electrolyte was then prepared by dissolving 0.2303 g (2

mmol, 100 mM), and 0.4605 g (4 mmol, 200 mM) of L- or D-Pro in water (20 mL), followed by the addition of 0.08 g (2 mmol, 100 mM), and 0.16 g (4 mmol, 200 mM) of NaOH for deprotonation. Subsequently, 1.4496 g (6 mmol, 300 mM) of $Cu(NO_3)_2 \cdot 3H_2O$ was added to the deprotonated Pro solution with continuous stirring for 5 minutes until fully dissolved. This outer electrolyte was then gently layered over the gel using a glass Pasteur pipette. The test tubes were sealed and left undisturbed. After two weeks, the gels were extracted, and the spherulites were isolated as outlined previously.

2.2.2.3 Coordination polymerization of homochiral and racemic CuAsp in 2D system

Overall preparation in a Petri dish is similar to in a 1D system, except that the resulting solutions were poured into the dish through a customized 2D reactor. 60 mL of the inner electrolyte, consisting of 1% wt/wt agar, 50 mM of L-, D-, and DL-Asp, and 100 mM of NaOH, was prepared as described in *section 2.2.2.1*. The mixture was then carefully poured into a Petri dish through the central tube of the 2D reactor, ensuring it spread smoothly and evenly into a thin layer between the plates, avoiding bubble formation. Once the gel solidified, 10 mL of 300 mM $Cu(NO_3)_2 \cdot 3H_2O$ solution was slowly added to the central tube using a glass Pasteur pipette. The central tube was covered and left undisturbed. After one week, the CuAsp spherulites were ready for collection.

2.2.2.4 Chiral separation of racemic Asp using homochiral Pro-copper complexes in 2D system

60 mL of the inner electrolyte, consisting of 1% wt/wt agar and deprotonated DL-Asp, was prepared as described in *section 2.2.2.1*. Then, the mixture was subsequently poured into a Petri dish through the central tube of the 2D reactor and left undisturbed until it solidified. The outer electrolyte was prepared by dissolving 0.2303 g (2 mmol, 100 mM), 0.3454 g (3 mmol, 150 mM), and 0.4605 g

(4 mmol, 200 mM) of L- or D-Pro in water (20 mL), followed by the addition of 0.08 g (2 mmol, 100 mM), 0.12 g (3 mmol, 150 mM), and 0.16 g (4 mmol, 200 mM) of NaOH, respectively for deprotonation. Subsequently, 1.4496 g (6 mmol, 300 mM) of $Cu(NO_3)_2 \cdot 3H_2O$ was added to the deprotonated Pro solutions with continuous stirring for 5 minutes until fully dissolved. Finally, 10 mL of outer electrolyte was carefully layered on top of the gels. After two weeks, the gels were extracted, and the spherulites were collected as described above.

2.2.3 Sample characterization

2.2.3.1 Solid-state circular dichroism

CD spectra were recorded in the range of 400 to 800 nm using a Jasco J-710 spectropolarimeter. The spectra were obtained with a resolution of 5 points/nm, and each curve represents the accumulation of 5 scans at a scan rate of 100 nm/min. A binomial filter with a convolution width of 99 points was applied. Solid-state samples were prepared as Nujol mulls by grinding the samples (2.0 – 2.8 mg) from each zone in a mortar and pestle in Nujol mineral oil to achieve a homogeneous mixture (30-35% wt/wt). This mixture was then sandwiched between two quartz discs (22.5 mm diameter, 1 mm thick), and the sample assembly was mounted using a circular cell holder.

2.2.3.2 Powder X-ray diffraction

PXRD patterns were collected on a Rigaku MiniFlex 6G X-ray diffractometer equipped with Cu-Kα radiation (λ = 1.54059 Å) and a sealed-tube X-ray source operating at 40 kV and 15 mA. Samples were smeared onto a zero-diffraction silicon wafer and measured between the 2θ of 3-50 in 0.01º step with a scan rate of 10º/min.

2.2.3.3 Scanning electron microscopy imaging

Scanning electron microscopy (SEM) images were acquired using a Tescan Mira instrument with an accelerating voltage of 15 kV. SEM samples were coated with a thin layer of platinum prior to imaging.

2.2.3.4 UV-Vis spectrophotometry

UV-Vis absorbance spectra were recorded in the range of 200 to 900 nm using a Varian Cary 100 Bio UV-Vis spectrophotometer. The following sample concentrations were prepared: (1) L- and D-Pro solutions at 10 mg/mL (20 mg of Pro in 2 mL of Millipore water), (2) a 10-fold dilution of 300 mM $Cu(NO_3)_2•3H_2O$, 100 mM L- and D-Pro-copper complexes, and (3) a 20-fold dilution for the 200 mM L- and D-Pro-copper complexes. Each solution sample was loaded in a quartz cuvette with an optical path of 2 mm for analysis.

2.3 Results and Discussion

2.3.1 Coordination polymerization and characterizations of L-, D-, and DL-CuAsp in 1D and 2D systems *via* RDF

Research on the coordination polymerization of CuAsp has traditionally focused on solution-based self-assembly processes.[49,50] However, to our knowledge, the coordination polymerization of CuAsp in hydrogels has not been previously documented. Taking advantage of the RDF, we have successfully achieved periodic precipitation of L-, D-, and DL-CuAsp coordination polymers in agar gel across both 1D and 2D systems (Fig. 2.2). The diffusion of $Cu(NO_3)_2•3H_2O$ solution, serving as the outer electrolyte into the gel containing deprotonated Asp, led to the formation of distinct blue spherulites. The evolution of this periodic precipitation is shown in Fig. 2.3.

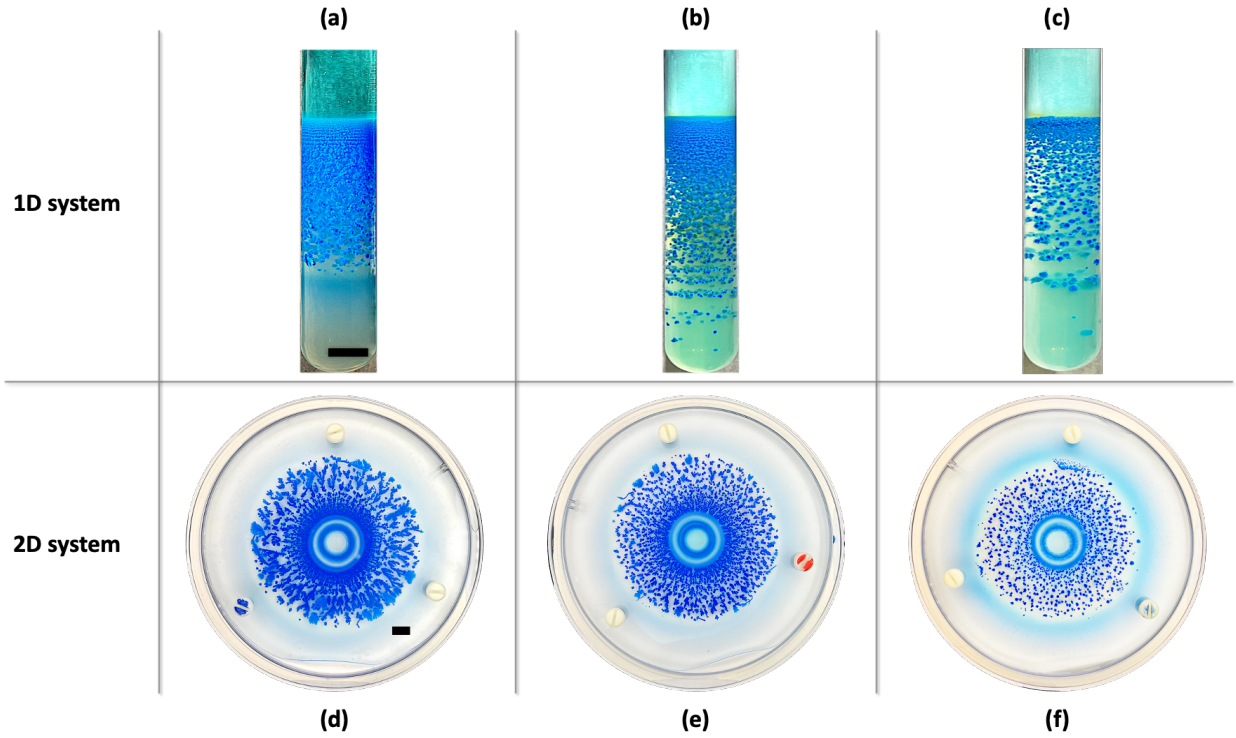

Figure 2.2. Periodic precipitation of (a and d) L-, (b and e) D-, and (c and f) DL-CuAsp spherulites in 1D and 2D agar gel systems. Scale bars: 1 cm.

A notable 6-fold higher concentration Cu^{2+} outer electrolyte was used to create a high level of supersaturation at the liquid-gel interface, facilitating rapid diffusion.[24] This setup established a concentration gradient, where supersaturation decreased with increasing distance from the interface, consequently leading to a gradient in crystal size. Smaller crystals were formed near the interface due to the higher supersaturation and nucleation rates, while larger crystals developed near the diffusion front where the crystal growth dominates (Fig. 2.4).

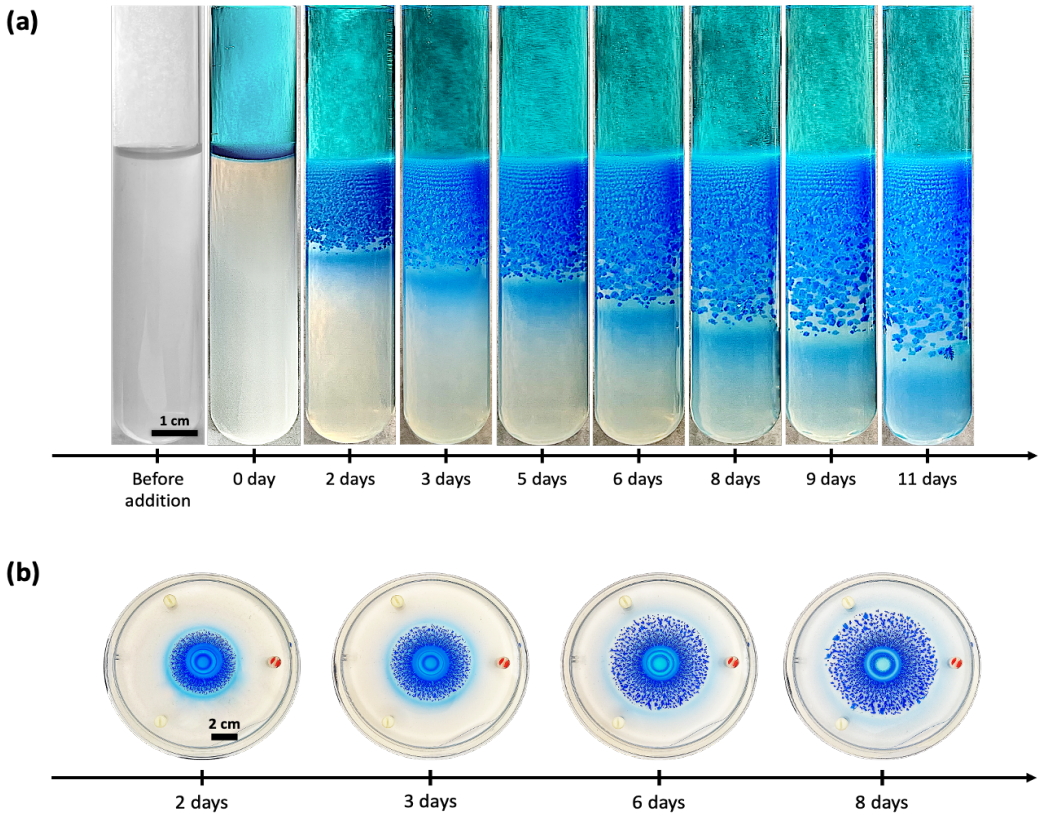

Figure 2.3. Time-lapse images of D-CuAsp periodic precipitation in the (a) 1D and (b) 2D systems.

The formation of spherulites is a common occurrence in gel growth, driven by diffusion-controlled processes. High supersaturation significantly influences the formation of CuAsp enantiomers with spherulitic morphology, marked by enhanced rates of polycrystalline incorporation on the crystal surface.[122] When Cu^{2+} ions coordinate with aspartate ions, the complexes develop into numerous 1D CuAsp nanofibrils, which subsequently aggregate into the nanofibers *via* weak interactions, such as hydrogen bonding and van der Waals forces.[50,87] SEM images revealed that the CuAsp nanofibers were densely aggregated around the spherulite nuclei (Fig. 2.5 a-c). Interestingly, although the overall size of the spherulites increased, the diameters of the nanofibers decreased progressively down the reaction tube (Fig. 2.5 d-f), ranging from 100 nm

near the interface to 50 nm near the diffusion front, aligning closely with those reported by Imaz *et al*.[49]

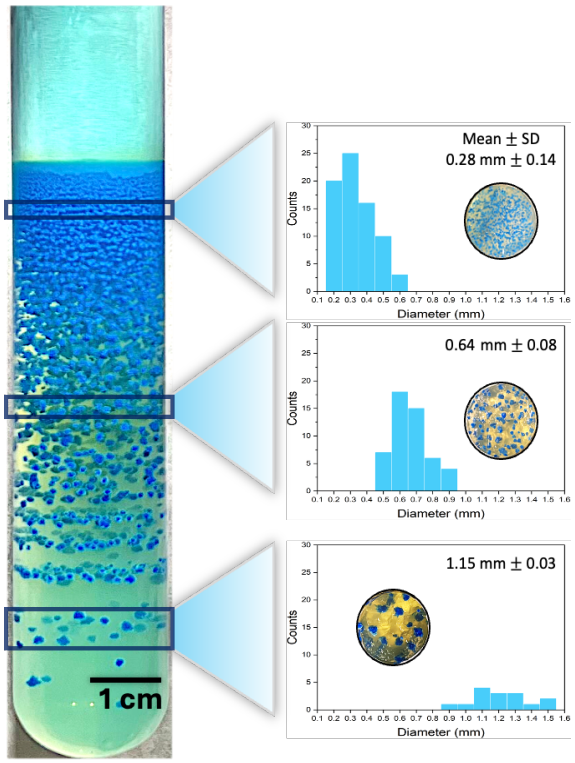

Figure 2.4. Slices of gels and histogram showing the diameter of D-CuAsp spherulites from different zones.

When comparing the precipitation patterns of homochiral CuAsp against DL-CuAsp, notable differences were observed in both the 1D and 2D systems (Fig. 2.2). Homochiral CuAsp spherulites formed densely packed arrays, while the DL-CuAsp spherulites were more discretely dispersed. This dispersion in DL-CuAsp is due to the slower formation of coordination complexes, a result of the incompatibilities between L- and D-Asp in nanofiber formation. When DL-Asp is used as building blocks, the L- and D-CuAsp nanofibers form independently, highlighting the crucial role of chirality in directing the assembly of amino acid-coordinated structures.[50] Research by Imaz *et al*. and Wu *et al*. demonstrated that mixing 70 mM of Cu^{2+} solution with 70 mM of

deprotonated L- or D-Asp results in rapid gelation, whereas a blue gel forms more slowly with DL-Asp at the same concentration, suggesting faster assembly rates for homochiral CuAsp compared to DL-CuAsp.[49,50] Furthermore, the discrepancy in crystallization patterns can also be attributed to the solubility differences between the compounds. DL-Asp, with a solubility of 7.78 mg/mL at 25ºC, is twice as soluble as homochiral Asp, which has a solubility between 4 mg/mL to 5 mg/mL at 25ºC.[46,124]

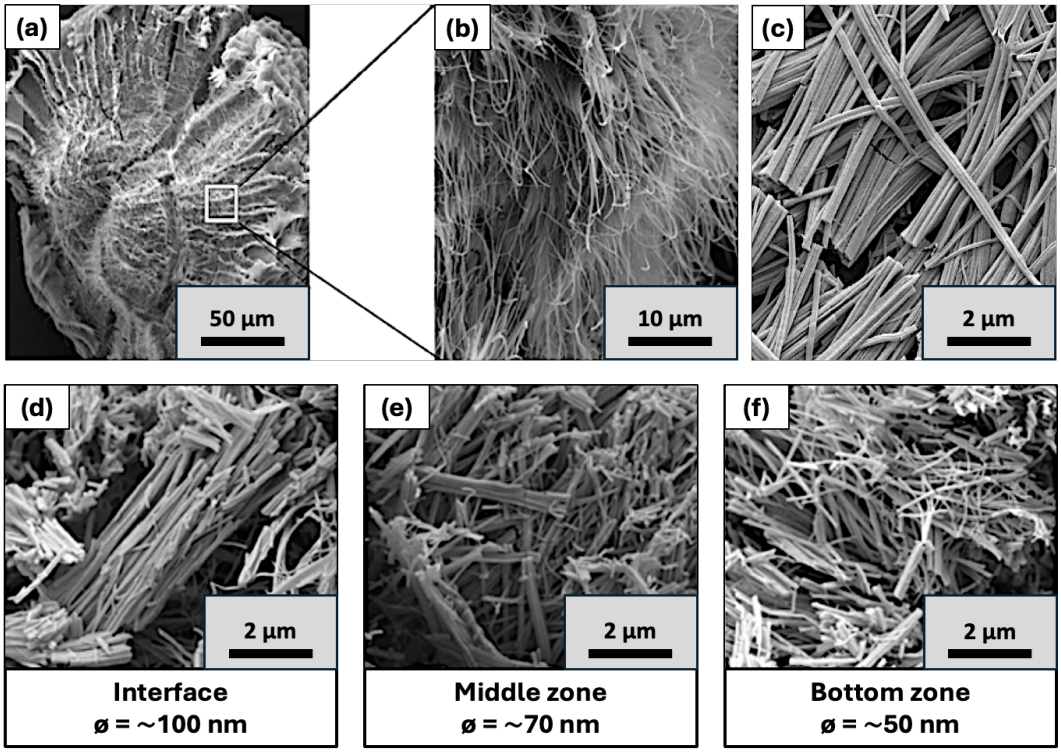

Figure 2.5. SEM images of a D-CuAsp spherulite cross-section. (a - c) The spherulite is made up of CuAsp nanofibers; (d - f) the diameter of D-CuAsp nanofibers near the liquid-gel interface, middle zone, and bottom zone in the reaction tube. Figures adapted from [125].

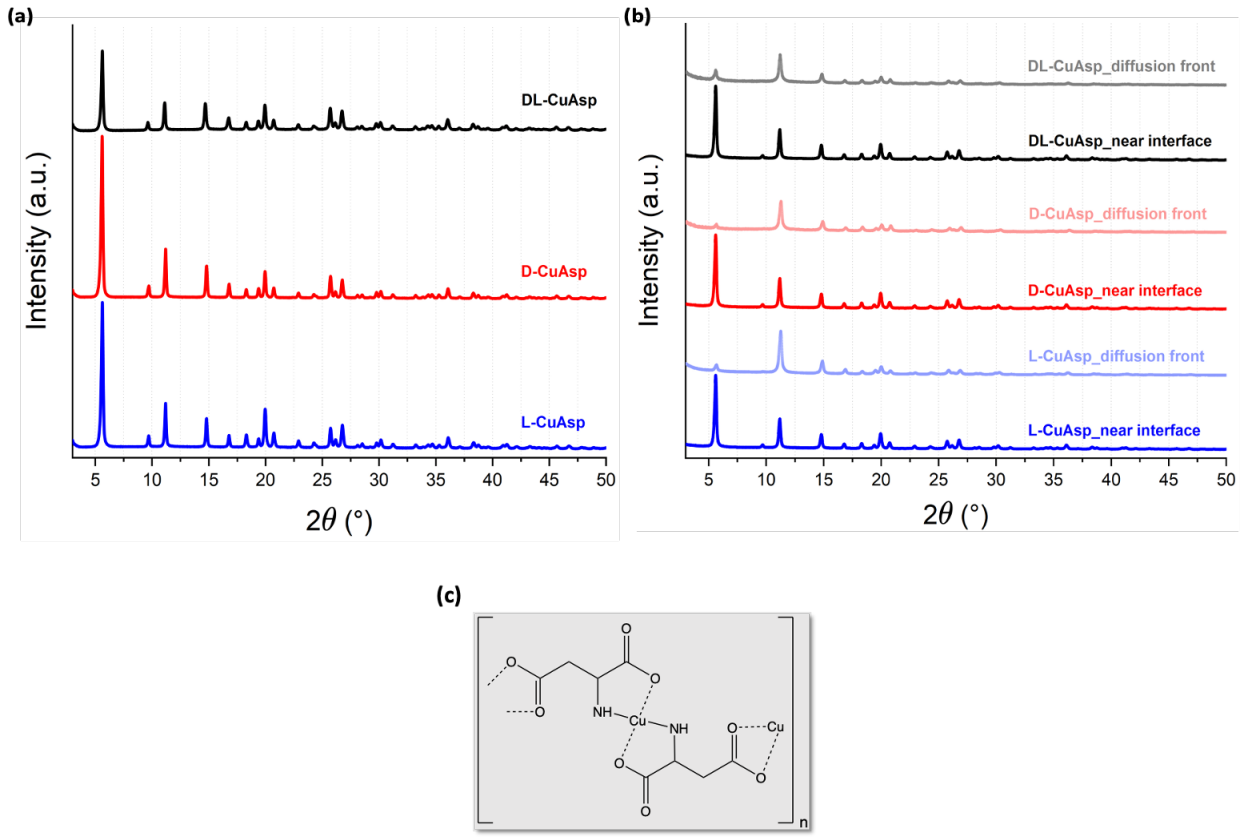

Figure 2.6. PXRD patterns of L- (blue), D- (red), and DL- (black) CuAsp in the (a) 1D and (b) 2D systems. (c) Structural model of the CuAsp coordination complex featuring a square-planar geometry formed through one-dimensional polymeric chains.[50]

PXRD performed on the CuAsp obtained from both systems confirmed their crystalline character. The PXRD data presented in Fig. 2.6 (a) for the 1D system is consistent with prior reports by Imaz *et al.*[49], where both L- and D-CuAsp exhibit the same diffraction patterns, indicating that both forms share the same crystal packing, similarly to the samples near the interface in the 2D system. Intriguingly, our analysis of DL-CuAsp also revealed the same diffraction pattern as the homochiral CuAsp. However, the samples collected from the diffusion front in the 2D system (Fig. 2.6 b) lack the reflections around 10º observed in other samples, possibly due to preferred orientation.[96,97,99] Unfortunately, a detailed analysis of the structural

connectivity was not feasible due to their sub-200 nm diameter nanofibers and the difficulty in obtaining large single crystals. Imaz and coworkers suggested that the CuAsp nanofibers were aligned in 1D $[Cu(Asp)(H_2O)_x]_n$ polymeric chains.[49] While, Wu *et al*. proposed a CuAsp coordination complex exhibited a square-planar geometry, where the copper ion is bonded to the α-carboxylate oxygen and amino nitrogen of the Asp to form the typical five-membered glycinate chelate ring (Fig. 2.6 c).[50]

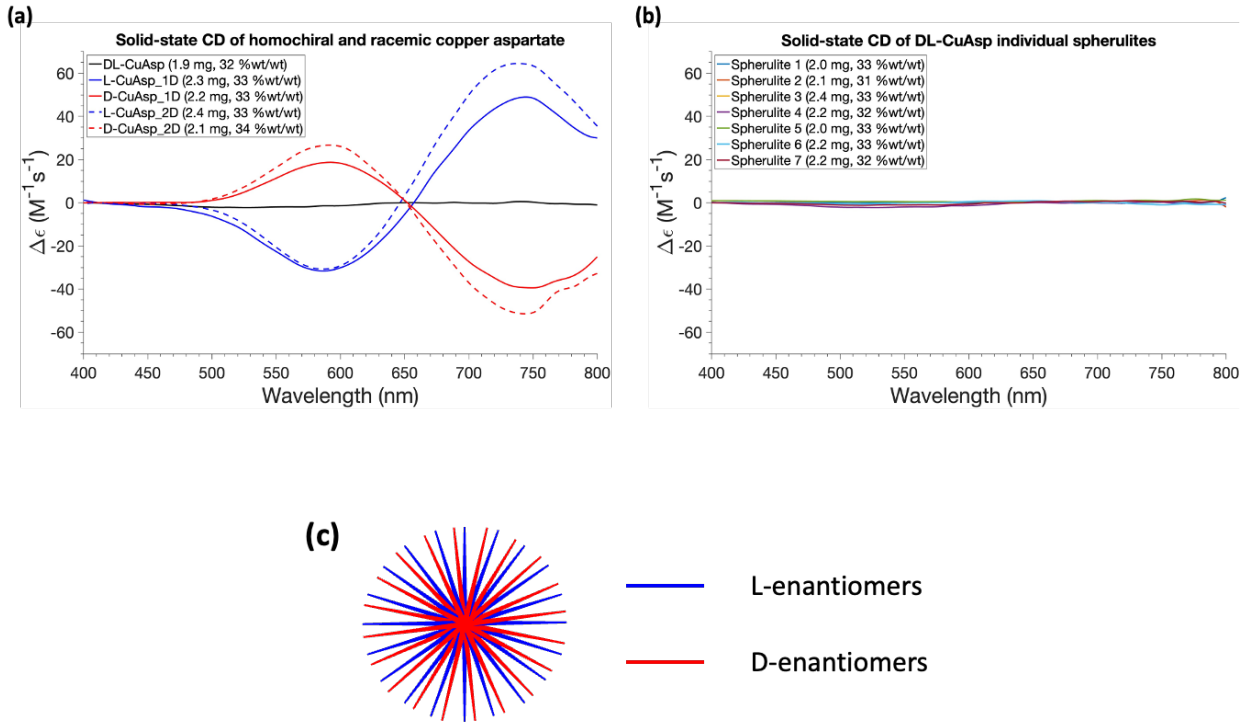

Figure 2.7. (a) Solid-state CD spectra of L- (blue), D- (red), and DL-(black) CuAsp in Nujol. Solid and dash lines outlined the signal of CuAsp obtained in 1D and 2D systems, respectively. (b) Solid-state CD spectra of individual DL-CuAsp spherulites. (c) DL-CuAsp spherulite is made up of individual homochiral nanofibers.

Solid-state CD was employed to investigate the chirality of CuAsp polymers. As depicted in Fig. 2.7 (a), L-CuAsp exhibited a positive Cotton effect, whereas D-CuAsp showed a negative

Cotton effect, with both crossing at a wavelength around 645 – 655 nm, indicating the presence of a chiral coordination sphere of the Cu^{2+} with chiral Asp.[49] In contrast, DL-CuAsp showed no Cotton effect, nor did the individual DL-CuAsp spherulites (Fig. 2.7 b). Recall that the PXRD pattern for the DL-CuAsp was the same as the homochiral CuAsp. This appears to contradict the CD results of the individual spherulites of DL-CuAsp with no chiral signal. A possible explanation for this unexpected outcome is that the nanofibers within each spherulite are individually homochiral (Fig. 2.7 c). However, they aggregate in such a way that they present racemic-like behavior in CD analysis, reconciling the observed PXRD data with the lack of chiral signal in the CD results.

So far, these findings have demonstrated that the RDF method can successfully facilitate the periodic precipitation of L-, D-, and DL-CuAsp coordination polymers in agar gels. In addition, this study paves the way for further exploration into the nuances of chiral resolution of DL-CuAsp using homochiral amino acid additives.

2.3.2 Chiral resolution of DL-Asp in the presence of homochiral Pro-copper complexes in the 1D and 2D systems

In this section, we aimed to achieve chiral resolution of DL-Asp in gels using L- and D-Pro-copper complexes in 1D and 2D systems. This approach was inspired by the pioneering work of Harada *et al*., who successfully resolved DL-Asp in solution using homochiral proline (Pro), alanine (Ala), and glutamic acid (Glu) copper complexes.[93] Their findings revealed that the configuration of the first crop of crystals always opposed that of the introduced chiral amino acid, a phenomenon known in preferential crystallization as the 'rule of reversal'.[89] The configuration of the second crop of crystals was determined by the mole ratio of the amino acid additive to DL-Asp. A critical factor for successful resolution by preferential crystallization is the ability of the racemic mixture to crystallize as a conglomerate,[89,91] making CuAsp an ideal candidate for our experiments. The TMAs used—homochiral amino acid-copper complexes—must mirror the

stereochemistry of DL-Asp to ensure they are adsorbed at and occluded from specific crystalline facets, thus inhibiting the growth of the affected enantiomer, and precipitating the opposite configuration first.

Prior to our experiments, we replicated Harada's work in solution by using a 1:1 mole ratio of L-Pro-copper complex to DL-Asp, following the procedures outlined in [93]. Notably, basic copper carbonate was used as the copper source, which differs from the $Cu(NO_3)_2 \cdot 3H_2O$ employed in the gel experiments. As illustrated in Fig. 2.8, the initial precipitation occurred after 1 day, with subsequent precipitation emerging after 5 days. Solid-state CD analysis showed that the first crop of crystals displayed a negative Cotton effect, indicative of the preferred crystallization of D-CuAsp, whereas the second crop exhibited a positive Cotton effect, confirming the crystallization of L-CuAsp. These observations are consistent with the results reported by Harada.[93]

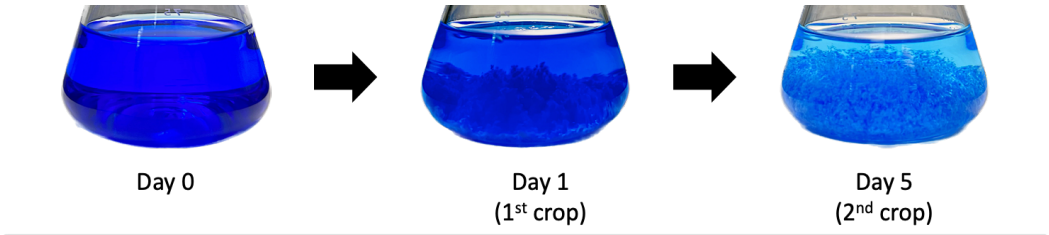

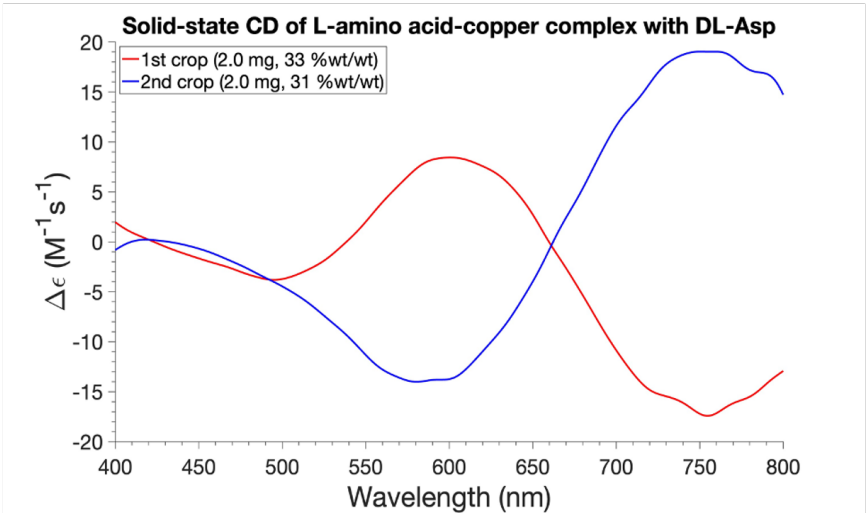

Figure 2.8. (Top) Visualizations of chiral resolution of Asp with L-Pro-copper complex (1:1 mole ratio to DL-Asp) in solution-state. (Bottom) Solid-state CD spectra of corresponding crops.

In our 1D gel-based experiments, we employed 100 mM or 200 mM of L- and D-Pro, with mole ratios of 2:3 and 4:3 to DL-Asp, respectively, to study the effects on crystallization. According to Harada *et al*., both the concentration of reactants and the mole ratio between the homochiral amino acid additives and DL-Asp, could affect the resolution process.[93] In order to confirm proper complexation, UV-Vis absorption was performed, revealing an adsorption shift from 800 nm to approximately 725 nm, regardless the concentration of Pro, indicating the formation of Pro-Cu(II) complexes in solution (Fig. 2.9).

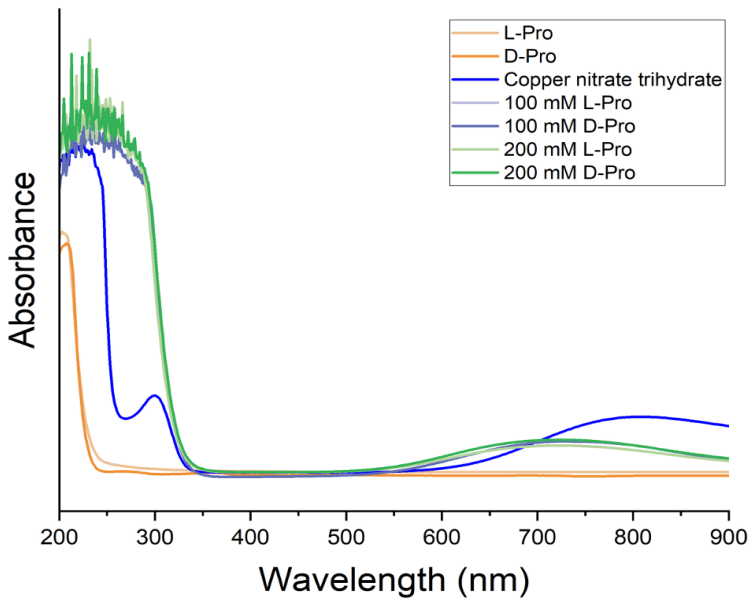

Figure 2.9. UV-Vis spectra of the starting materials (L- and D-Pro, copper nitrate trihydrate) and copper complexes with 100 mM and 200 mM L- and D-Pro.

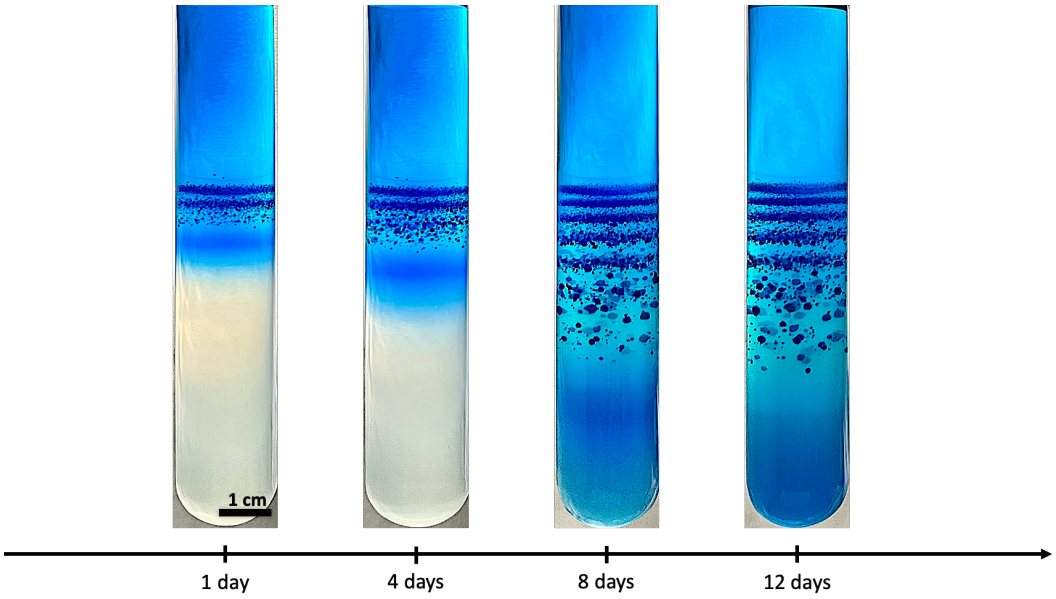

Figure 2.10. Periodic precipitation of chiral resolution of DL-Asp in the presence of 100 mM D-Pro in 1D system.

After diffusing Pro-copper complexes into DL-Asp gel, a spatiotemporal band formation of CuAsp polymers in the test tube was observed. The evolution of this periodic precipitation is shown in Fig. 2.10. The samples obtained near the interface consistently showed chirality opposite to that the introduced TMAs. Solid-state CD analysis reveals negative Cotton effect in the presence of L-Pro-copper complexes, suggesting predominance of D-CuAsp. In contrast, the presence of D-Pro-copper complexes led to positive Cotton effects, indicating L-CuAsp formation (Fig. 2.11 and 2.12). These results aligned with the 'rule of reversal'. However, the overall chiral intensity showed a notable decreased when L- and D-Pro-copper complexes were introduced compared to the coordination without TMAs. This suggests that although these TMAs selectively attached on the nanofibers of the conglomerates, which possessed the same configuration, they only partially resolved the DL-Asp conglomerates. Notably, fewer precipitates formed at higher concentration of Pro-copper compared to lower concentration due to the slower coordination rate.

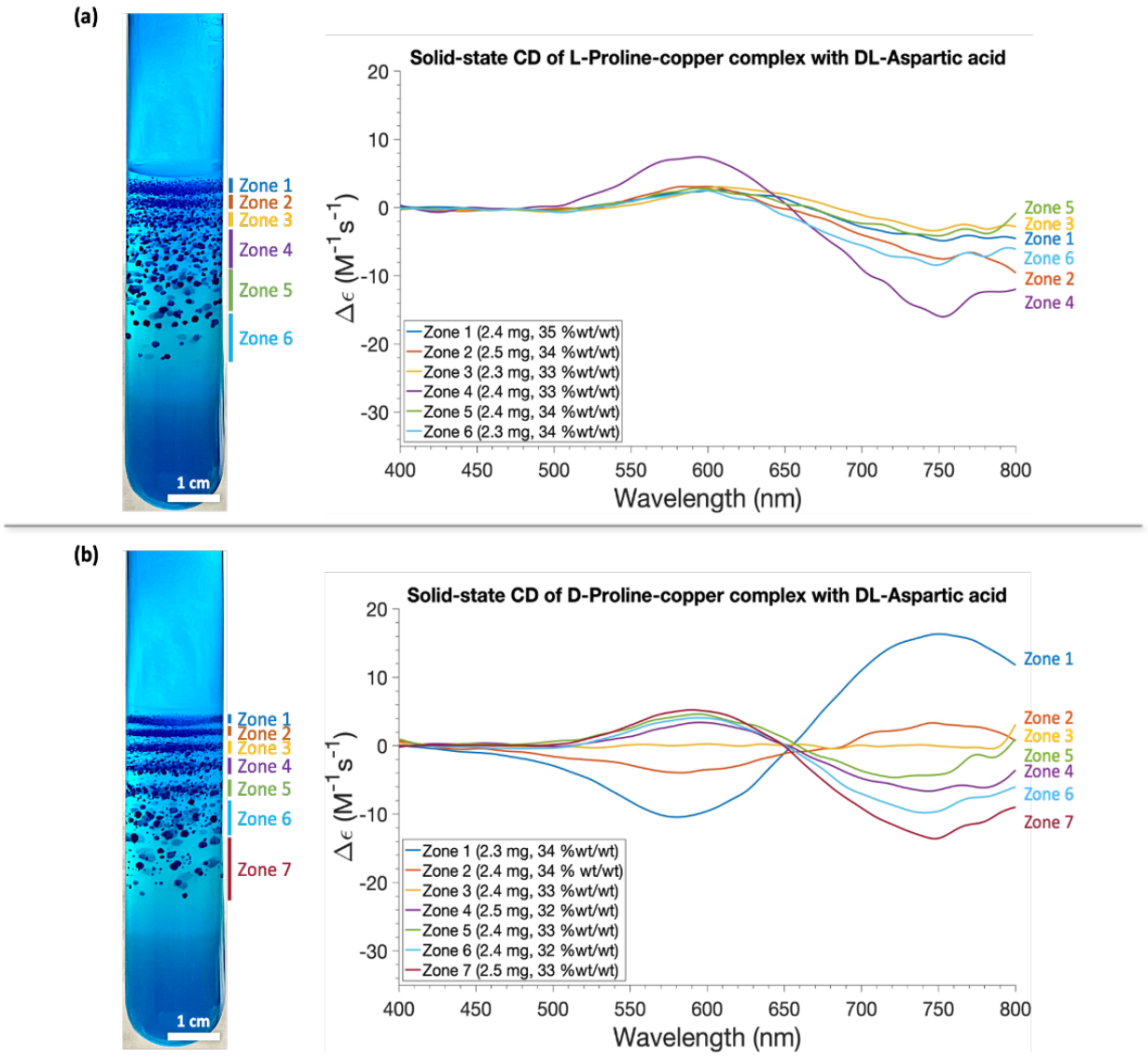

Figure 2.11. (Left) Visualizations of DL-CuAsp coordination complexes crystallized in the presence of 100 mM (a) L-Pro-copper complex and (b) D-Pro-copper complex in the 1D system. (Right) Solid-state CD spectra of each precipitation zone.

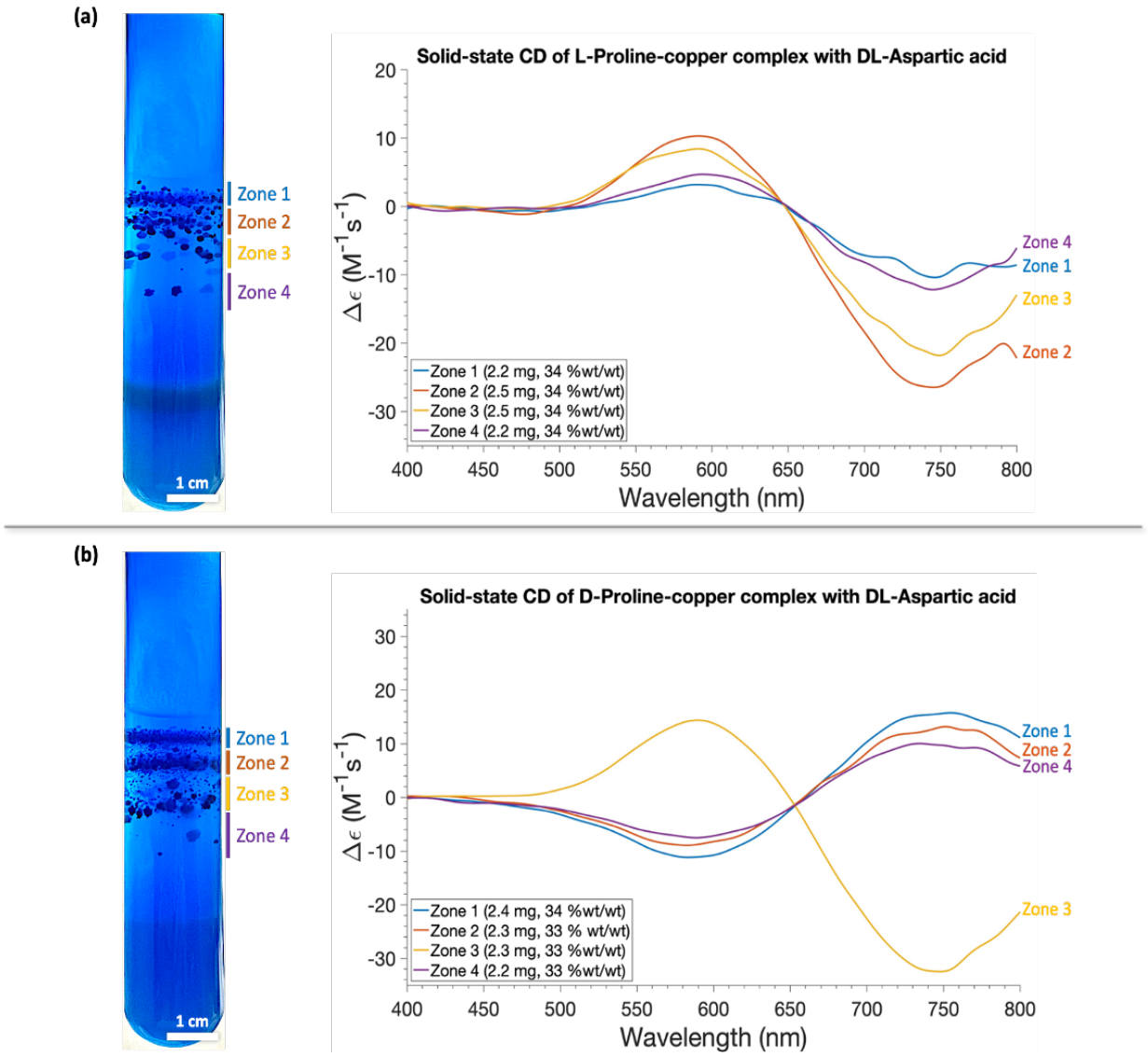

Figure 2.12. (Left) Visualizations of DL-CuAsp coordination complexes crystallized in the presence of 200 mM (a) L-Pro-copper complex and (b) D-Pro-copper complex in the 1D system. (Right) Solid-state CD spectra of each precipitation zone.

During crystallizations involving L-Pro-copper additives, mainly negative Cotton effect was observed for all the zones (Fig 2.11 a and 2.12 a), indicating the predominance of D-CuAsp formations in these reactions. A lower chiral intensity was observed in the presence of 100 mM L-Pro-copper compared to 200 mM L-Pro-copper, suggesting that a decrease in concentration of

additive resulted in a progressive decrease in altering the affected L-nanofibers.[90] With 100 mM D-Pro-copper additive, a gradual chiral switching from positive to negative Cotton effects was observed (Fig. 2.11 b), yet two chiral switching events occurred in the presence of 200 mM D-Pro (Fig. 2.12 b). This switching could be attributed to the local concentration varied along the reaction tube, influenced by diffusion gradients or local supersaturation levels. An additional variation is the composition of the agar gel, which primarily consisting of D-galactose. In the context of the 'rule of reversal', the TMAs could be a slightly modified molecule with a stereochemistry resembling the host molecule.[118] Therefore, it is plausible that the agar itself could act as a chiral competitor, diminishing the chiral influence of the D-Pro-copper additive, thus preventing the selective adsorption.

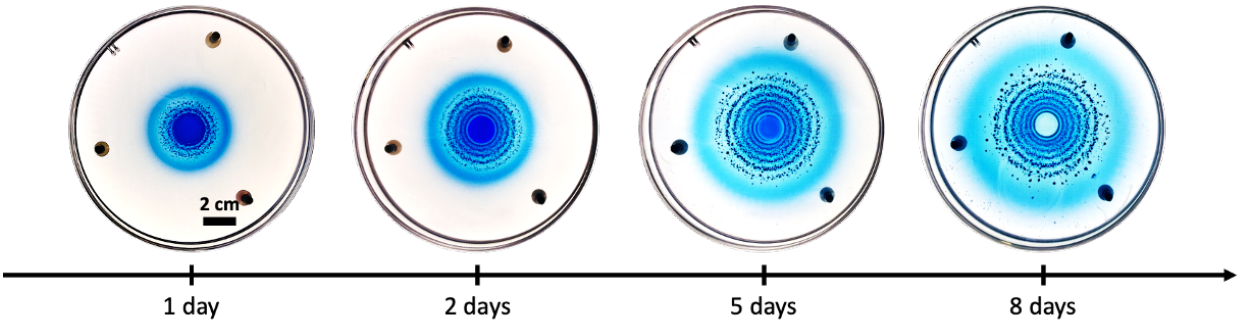

Figure 2.13. Time-lapse images of chiral resolution of DL-Asp in the presence of 100 mM D-Pro-copper complex in 2D system.

In the 2D system, the evolution of ring formation of CuAsp polymers is depicted in Fig 2.13. The samples obtained near the interface exhibited chirality opposite to that the introduced TMAs in all conditions (Fig 2.14 – 2.16), which agreed with the 'rule of reversal'. Samples obtained from zones 3 and 4 in the presence of 100 mM (Fig. 2.14 a) and zone 2 obtained when using 150 mM (Fig. 2.15 a) L-Pro-copper, showed relatively weak positive Cotton effect or nearly no Cotton effect,

likely due to the depletion of L-Pro-copper complex within those regions, until the concentrations were replenished, then a subsequent precipitate with negative Cotton effect reoccurred. However, in the presence of 200 mM L-Pro-copper, all three zones consistently showing negative Cotton effect (Fig. 2.16 a).

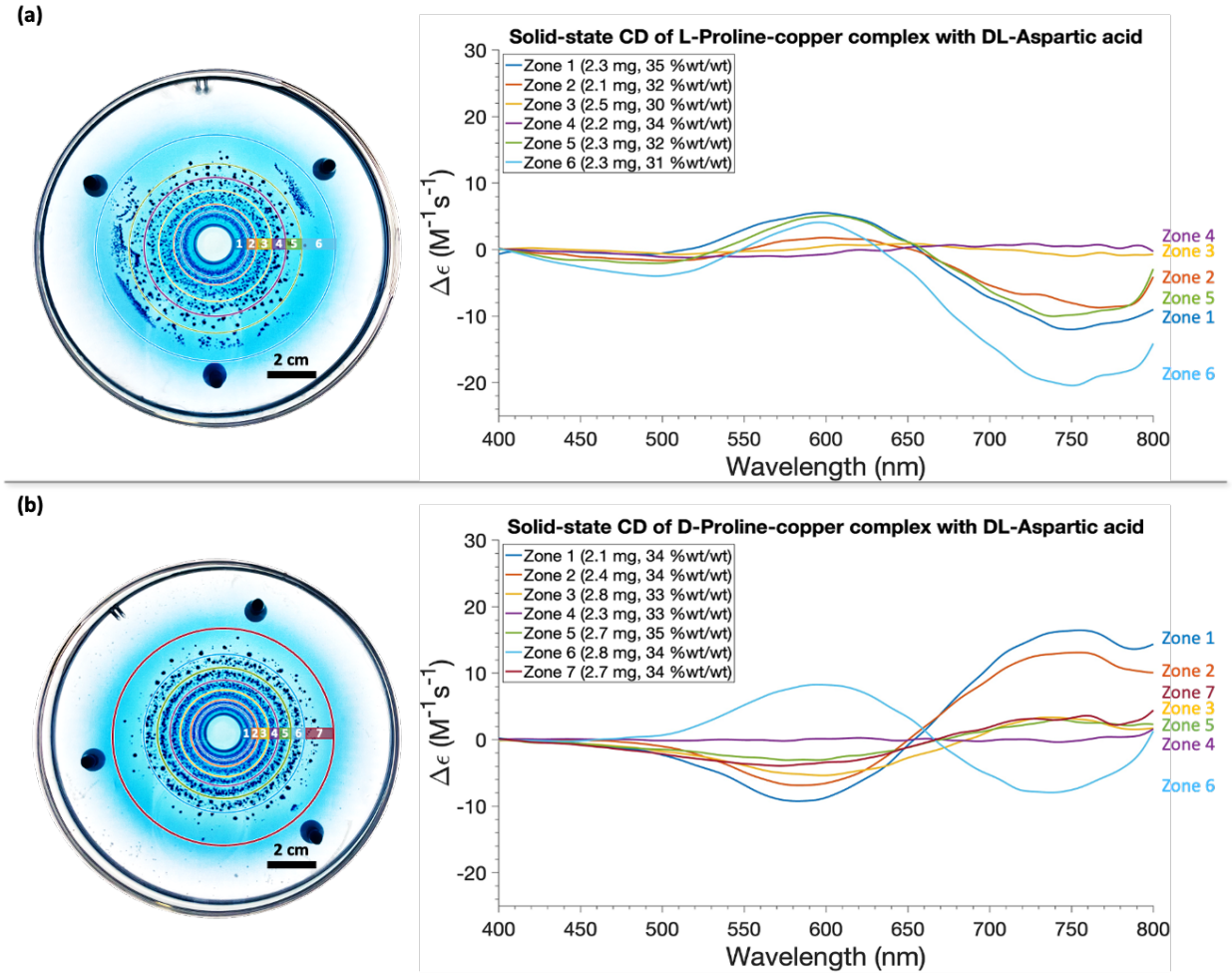

Figure 2.14. (Left) Illustrations of DL-CuAsp coordination complexes crystallized in the presence of 100 mM (a) L-Pro-copper complex and (b) D-Pro-copper complex in the 2D system. (Right) Solid-state CD spectra of each precipitation zone.

Figure 2.15. (Left) Illustrations of DL-CuAsp coordination complexes crystallized in the presence of 150 mM (a) L-Pro-copper complex and (b) D-Pro-copper complex in the 2D system. (Right) Solid-state

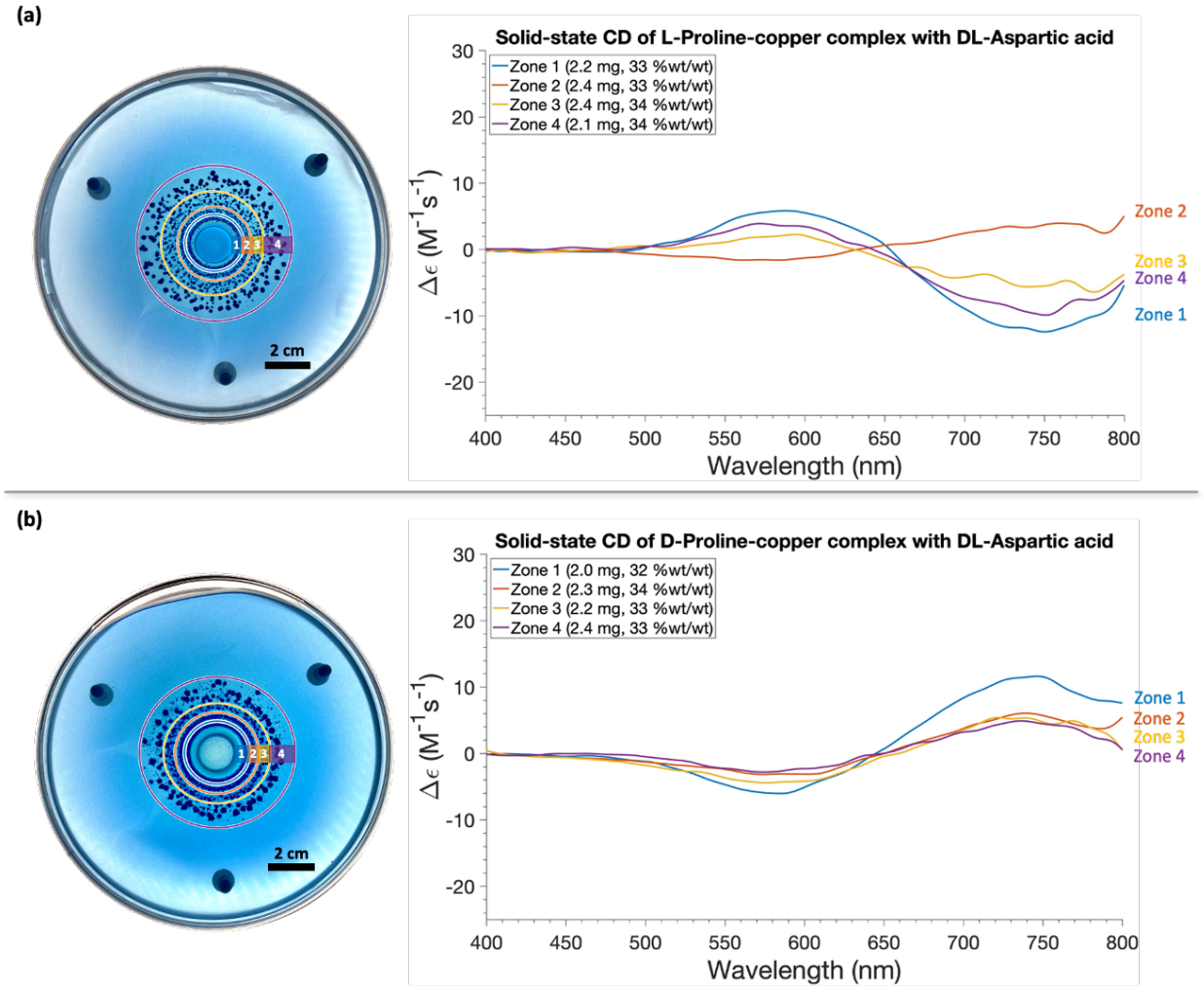

CD spectra of each precipitation zone.

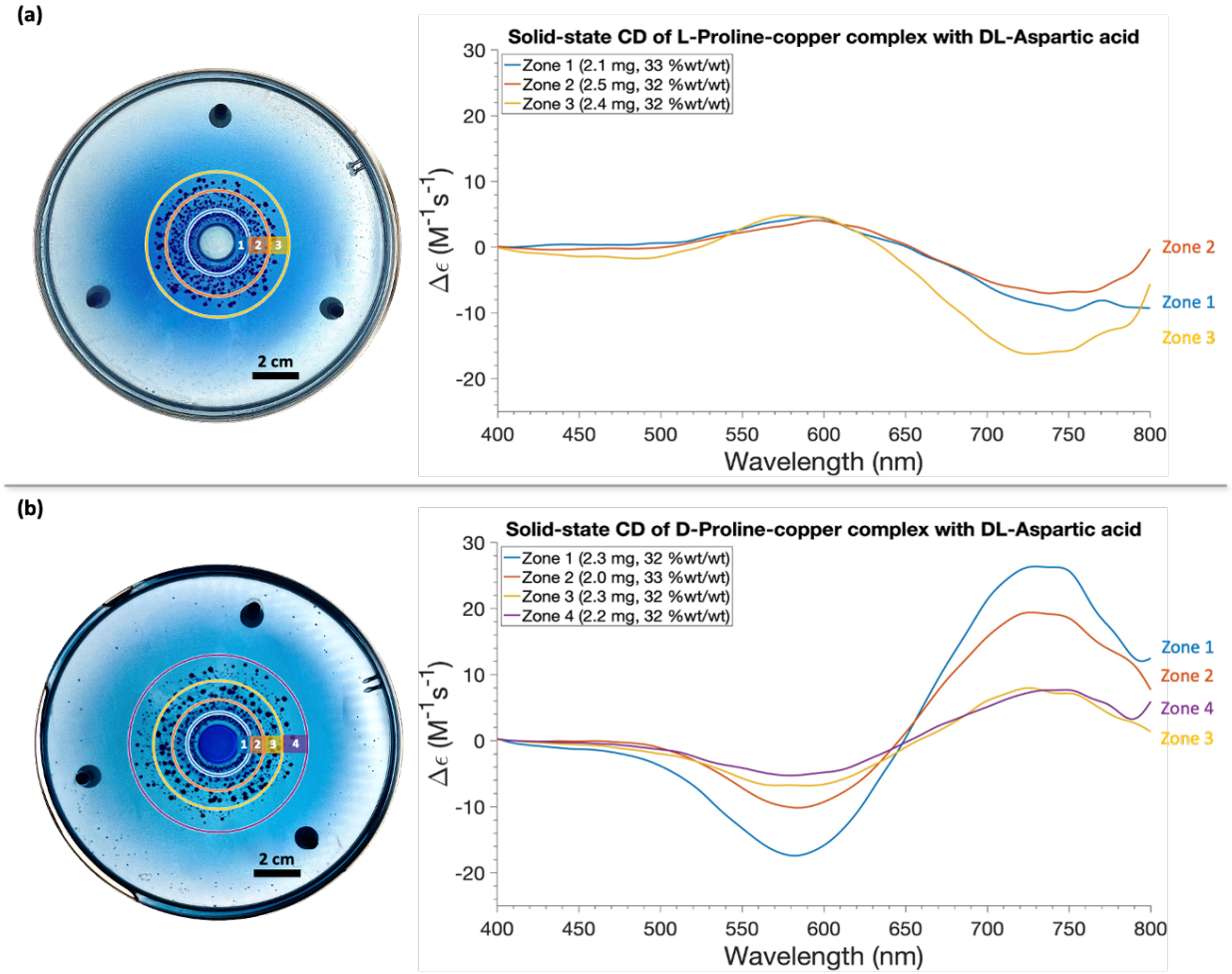

Figure 2.16. (Left) Illustrations of DL-CuAsp coordination complexes crystallized in the presence of 200 mM (a) L-Pro-copper complex and (b) D-Pro-copper complex in the 2D system. (Right) Solid-state CD spectra of each precipitation zone.

However, in the 2D system with 100 mM D-Pro, two chiral switching events were observed. This started with zones exhibiting a positive Cotton effect near the center, followed by a switching towards negative Cotton effect in zone 6, then a subsequent positive Cotton effect reoccurred in zone 7 (Fig. 2.14 b). Similar chiral switching was observed in the 1D system with 200 mM D-Pro, which is possibly due to the feedback mechanism of local concentrations of electrolytes. At higher concentrations of D-Pro, all zones exhibited consistently a positive Cotton effect (Fig. 2.15 b and 2.16 b). PXRD analyses were performed on the samples near the interface and at the diffusion

front obtained from both 1D and 2D systems (Fig. 2.17), confirming the crystalline structure. Moreover, the partially resolved DL-CuAsp exhibited consistent phases of the to the DL-Asp conglomerates without TMAs.

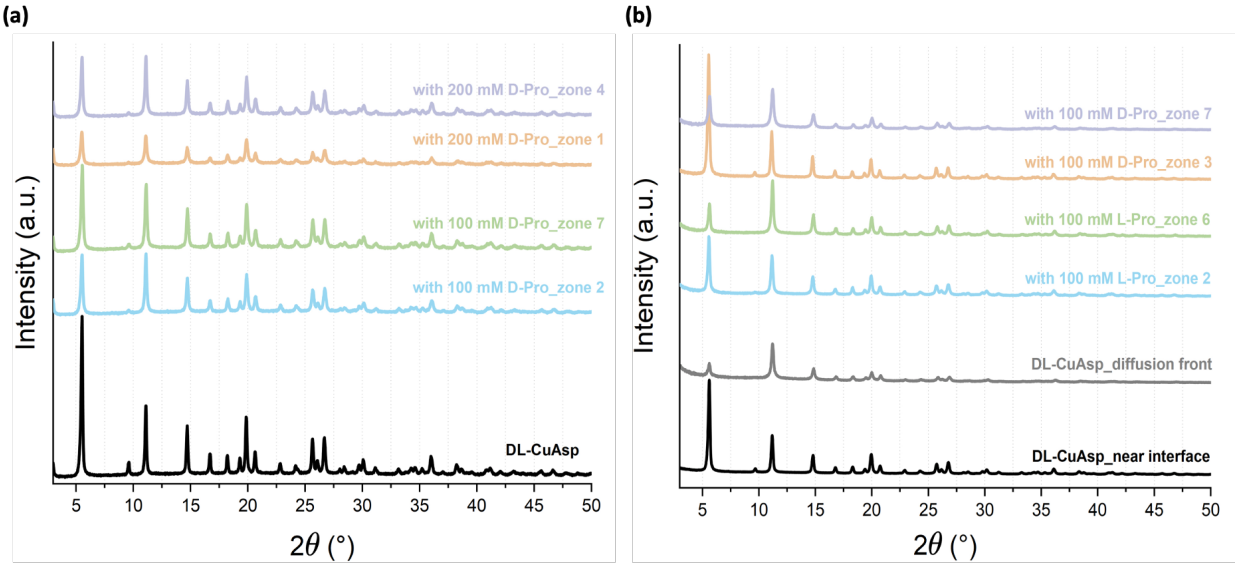

Figure 2.17. (a) PXRD pattern of DL-CuAsp, resulting samples obtained near the interface and at diffusion front, in the presence of 100 mM and 200 mM D-Pro-copper complex in the 1D system. (b) PXRD pattern of DL-CuAsp and the samples obtained near the interface and at diffusion front, with 100 mM L- and D-Pro-copper complex in the 2D system.

2.4 Conclusions

Herein, coordination polymerization of CuAsp and additive-assisted preferential crystallization of DL-Asp using L- or D-Pro-copper complexes were carried out via RDF in 1D and 2D agar gel systems. The supersaturation gradient induced across the diffusion flux resulted in CuAsp coordination polymers with spherulitic morphology, exhibiting gradients in crystal sizes. Solid-state CD analysis revealed that L-CuAsp and D-CuAsp showed positive and negative Cotton effects, respectively, while DL-CuAsp showed no Cotton effect. However, PXRD analyses of these

polymers displayed the same diffraction patterns, indicating that DL-CuAsp crystallized as a conglomerate.

The introduction of chiral additives led to crystalline CuAsp near the liquid-gel interface adopting configurations opposite to those of the introduced additives. This aligned with the 'rule of reversal' in preferential crystallization. Further from the interface, CuAsp precipitates showed varied chirality due to the concentration gradients. Intriguingly, with L-Pro-copper complexes, a consistent negative Cotton effect was observed, suggesting that the composition of agar gel influenced the reaction outcomes. PXRD confirmed that the resolved CuAsp shared the same crystalline phases as DL-Asp conglomerates without additives. This research underscores the potential of additive-assisted preferential crystallization *via* RDF as an innovative approach for resolution of other racemic compounds, with implications for the pharmaceutical, food industries, as well as applications in material engineering.

Chapter 3

Conclusions

The main objective of this study was to achieve (i) the conglomerate polymerization of L-, D-, and DL-CuAsp and (ii) the spatiotemporal resolution of DL-Asp in gel using homochiral Pro-copper complexes in agar gel. In part (i), the work was inspired by Imaz *et al*. who successfully prepared CuAsp nanofibers at the interface of a Cu^{2+} solution with a water/ethanol mixture containing deprotonated L or D-Asp.[49] Building on this, we demonstrated the crystallization of CuAsp CPs with a spherulitic morphology *via* RDF in both 1D and 2D agar gel systems. By diffusing a higher concentration of $Cu(NO_3)_2 \bullet H_2O$ into the agar gel containing lower concentration of deprotonated Asp, generated a concentration gradient that drove the formation of Liesegang bands in 1D system and concentric rings in 2D system. Solid-state CD spectra of both L-CuAsp and D-CuAsp displayed opposite Cotton effects, confirming their chiral nature. To confirm conglomerate formation, detailed CD analysis of the bands and individual spherulites of DL-CuAsp indicated the formation of a racemic polymer. Based on our PXRD and CD results, we propose that individual homochiral nanofibers self-assemble into an overall racemic spherulite. While a detailed crystal structure analysis was not possible, we deduced that the CuAsp nanofibers were aligned in 1D $[Cu(Asp)(H_2O)_x]_n$ polymeric chain, and that the CuAsp coordination complex adopted a square planar geometry, as previously reported by Imaz *et al*.[49] and Wu *et al*.[50]

Chiral resolution remains crucial in the pharmaceutical and food industries to ensure the efficacy and safety of chiral compounds.[111] In part (ii), we conducted the spatiotemporal resolution of DL-Asp in 1D and 2D agar gel systems, employing homochiral Pro-copper complexes as TMAs. Solid-state CD analysis was performed to study the chirality of the resolved CuAsp. Our CD results were consistent with the principles of preferential crystallization and the 'rule of reversal'.[89] We

observed that varying the concentrations of TMAs resulted in different resolution outcomes, highlighting the influence of TMA concentration on the process. Furthermore, the agar gel not only provided a diffusion environment for crystallization but also influenced the resolution outcomes due to the chiral nature of its composition. Furthermore, PXRD analysis confirmed that the resolved CuAsp shared the same crystalline phases as the DL-Asp conglomerates formed without additives.

In conclusion, this research demonstrates the potential of preferential crystallization *via* RDF, using chiral amino acid-based coordination polymers, as an innovative approach for resolving other conglomerate compounds. This method offers a sustainable and cost-effective alternative, as it does not require hazardous solvents, and amino acids are inexpensive, biodegradable and biocompatible, with the versatile capabilities in coordinating with metal ions.

Future work

Several experiments could be conducted to further explore the resolution of conglomerates in agar gel systems. A promising direction for future research involves substituting the chiral agar gel with an achiral sodium metasilicate gel to investigate chiral resolution of DL-Asp using homochiral Pro-copper complexes. This experimental setup aims to determine whether the hierarchical chirality of the agar gel influences the resolution outcomes. Moreover, taking the advantage of the 2D system, we can conduct the conglomerate crystallization of L-, D-, and DL-CuAsp by applying electric field (Fig. 3.1 a), to observe the effects on the pattern formation of precipitates. This approach is inspired by the work of Badr *et al*.[10], who demonstrated the periodic precipitation of $Co(OH)_2$ by layering the NH_4OH onto the gelatin gel containing $CoCl_2 \cdot 6H_2O$, with the application of a DC current under a potential difference of 4V. They observed narrow band spacing of $Co(OH)_2$

ring patterns without applying electric field, whereas a larger spacing occurred in the presence of an electric field (Fig. 3.1 b).

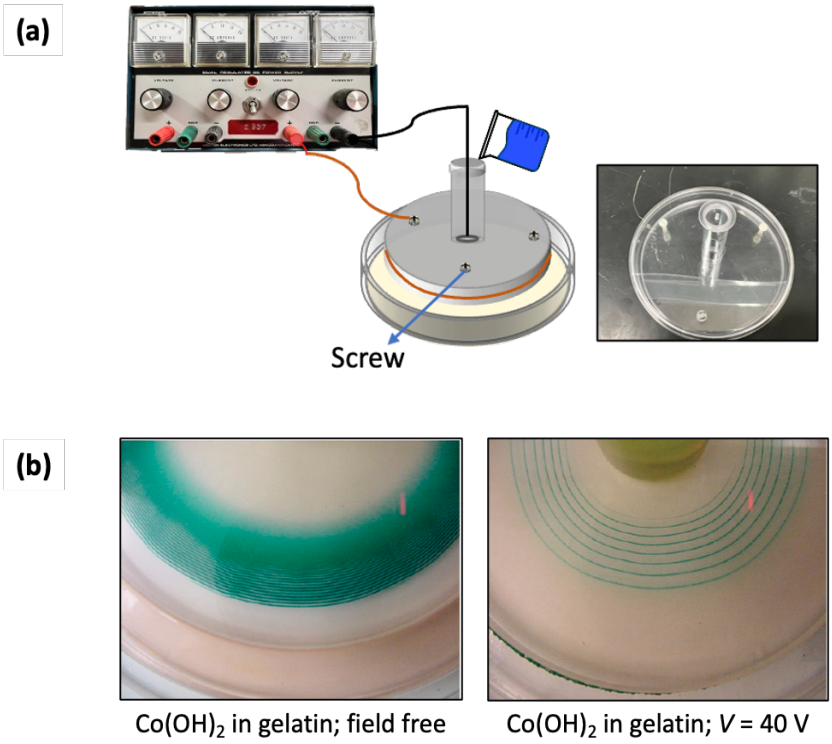

Figure 3.1. (a) Schematic illustration of the 2D RDF experiment with application of an electric field. (b) $Co(OH)_2$ precipitate patterns in gelatin gel: field-free environment (left) and under a DC of 4V (right), highlighting the increase in band spacing when the electric field is applied.[10]

Another interesting future work is the spatiotemporal resolution of sodium ammonium tartrate in agar gel *via* RDF. As discussed in Chapter 1, Louis Pasteur was the first to demonstrate the resolution of a racemic mixture of sodium ammonium tartrate tetrahydrate.[40–42] This process was later revisited by Ostromisslensky in 1908,[126] who successfully resolved sodium ammonium tartrate using additive-assisted preferential crystallization using malic acid or asparagine (Asn).[89] Building on these studies, we propose an experimental setup in which a homochiral Asn-sodium complex is diffused into an agar gel containing deprotonated DL-tartaric acid, neutralized by ammonium hydroxide. The aim of this setup is to resolve sodium ammonium tartrate conglomerate

crystals through preferential crystallization, following the ‘rule of reversal’. The agar gel would act as a diffusion-controlled matrix, slowing down nucleation, and thereby further enhancing the resolution efficiency.

References

(1) Whitesides, G. M.; Grzybowski, B. Self-Assembly at All Scales. *Science* **2002**, *295* (5564), 2418–2421.

(2) Hoffmann, F. *Introduction to Crystallography*, 1st ed.; Springer: Cham, Switzerland, 2020.

(3) Isaeva, V. V. Self-Organization in Biological Systems. *Biol. Bull.* **2012**, *39* (2), 110–118.

(4) Grzybowski, B. A.; Bishop, K. J.; Campbell, C. J.; Fialkowski, M.; Smoukov, S. K. Micro- and Nanotechnology via Reaction–Diffusion. *Soft Matter* **2005**, *1* (2), 114–128.

(5) Nabika, H.; Itatani, M.; Lagzi, I. Pattern Formation in Precipitation Reactions: The Liesegang Phenomenon. *Langmuir* **2019**, *36* (2), 481–497.

(6) Turing, A. M. The Chemical Basis of Morphogenesis. *Bull. Math. Biol.* **1990**, *52*, 153–197.

(7) Ball, P. Forging Patterns and Making Waves from Biology to Geology: A Commentary on Turing (1952) 'The Chemical Basis of Morphogenesis.' *Philos. Trans. R. Soc. Lond. B Biol. Sci.* **2015**, *370* (1666), 20140218.

(8) Zaikin, A. N.; Zhabotinsky, A. M. Concentration Wave Propagation in Two-Dimensional Liquid-Phase Self-Oscillating System. *Nature* **1970**, *225* (5232), 535–537.

(9) Grzybowski, B. A. *Chemistry in Motion: Reaction-Diffusion Systems for Micro-and Nanotechnology*; John Wiley & Sons, 2009.

(10) Badr, L.; Sultan, R. Ring Morphology and pH Effects in 2D and 1D $Co(OH)_2$ Liesegang Systems. *J. Phys. Chem. A* **2009**, *113* (24), 6581–6586.

(11) Papineau, D. Chemically Oscillating Reactions in the Formation of Botryoidal Malachite. *Am. Mineral.* **2020**, *105* (4), 447–454.

(12) Stern, K. H. The Liesegang Phenomenon. *Chem. Rev.* **1954**, *54* (1), 79–99.

(13) Sadek, S.; Sultan, R. Liesegang Patterns in Nature: A Diverse Scenery across the Sciences. *Precipitation patterns in reaction-diffusion systems* **2010**, *661*, 1–43.

(14) Nabika, H. Liesegang Phenomena: Spontaneous Pattern Formation Engineered by Chemical Reactions. *Curr. Phys. Chem.* **2015**, *5* (1), 5–20.

(15) Jablczynski, C. K. The Rhythmic Formation of Precipitates Liesegang Rings. *Bull. Soc. Chim. Fr.* **1923**, *33*, 1592–1602.

(16) Matalon, R.; Packter, A. The Liesegang Phenomenon. I. Sol Protection and Diffusion. *J.Colloid Sci.* **1955**, *10* (1), 46–62.

(17) Sultan, R. F. Rhythmic Precipitate Patterns and Fractal Structure. *Acta. Phys. Sin.* **2011**, *27*, 119–124.

(18) Morse, H. W.; Pierce, G. W. Diffusion and Supersaturation in Gelatine. *Phys. Rev. (Series I)* **1903**, *17* (3), 129.

(19) Itatani, M.; Onishi, Y.; Suematsu, N. J.; Lagzi, I. Periodic Precipitation in a Confined Liquid Layer. *J. Phys. Chem. Lett.* **2024**, *15* (18), 4948–4957.

(20) Ostwald, W. *Lehrbuch Der Allgemeinen Chemie*; W. Engelmann, 1891; Vol. 1.

(21) Nakouzi, E.; Steinbock, O. Self-Organization in Precipitation Reactions Far from the Equilibrium. *Sci. Adv.* **2016**, *2* (8), e1601144.

(22) Henisch, H. K. *Crystals in Gels and Liesegang Rings*; 1988.

(23) Asenath-Smith, E.; Li, H.; Keene, E. C.; Seh, Z. W.; Estroff, L. A. Crystal Growth of Calcium Carbonate in Hydrogels as a Model of Biomineralization. *Adv. Funct. Mater.* **2012**, *22* (14), 2891–2914.

(24) Issa, R.; Hmadeh, M.; Al-Ghoul, M. Control of Particle Size and Morphology of MOF-199 Crystals via a Reaction-Diffusion Framework. *Trans. Tech. Publ.* **2017**, *380*, 39–47.

(25) Suganthi, R. V.; Girija, E. K.; Narayana Kalkura, S.; Varma, H. K.; Rajaram, A. Self-Assembled Right-Handed Helical Ribbons of the Bone Mineral Hydroxyapatite. *J. Mater. Sci.: Mater. Med.* **2009**, *20*, 131–136.

(26) Patel, A. R.; Venkateswara Rao, A. Crystal Growth in Gel Media. *Bull. Mater. Sci.* **1982**, *4*, 527–548.

(27) Gour, N.; Kanth, C. P.; Koshti, B.; Kshtriya, V.; Shah, D.; Patel, S.; Agrawal-Rajput, R.; Pandey, M. K. Amyloid-Like Structures Formed by Single Amino Acid Self-Assemblies of Cysteine and Methionine. *ACS Chem. Neurosci.* **2019**, *10* (3), 1230.

(28) Lord, K. *Baltimores Lectures on Molecular Dynamics and the Wave Theory of Light: Founded on Mr AS Hathaway's Stenographic Report of Twenty Lectures Delivered in Johns Hopkins*; CJ Clay and sons, 1904.

(29) Sallembien, Q.; Bouteiller, L.; Crassous, J.; Raynal, M. (Review) Possible Chemical and Physical Scenarios towards Biological Homochirality. *Chem. Soc. Rev.* **2022**, *51* (9), 3436–3476.

(30) Inaki, M.; Liu, J.; Matsuno, K. Cell Chirality: Its Origin and Roles in Left–Right Asymmetric Development. *Philosophical Transactions of the Royal Society B: Biological Sciences* **2016**, *371* (1710), 20150403.

(31) Pray, L. Discovery of DNA Structure and Function: Watson and Crick. *Nature Education* **2008**, *1* (1), 100.

(32) Amabilino, D. B. *Chirality at the Nanoscale: Nanoparticles, Surfaces, Materials and More*; John Wiley & Sons, 2009.

(33) Noorduin, W. L. *Single Chirality through Crystal Grinding*; Sl: sn, 2010.

(34) Grzybowski, B. A.; Wilmer, C. E.; Kim, J.; Browne, K. P.; Bishop, K. J. Self-Assembly: From Crystals to Cells. *Soft Matter* **2009**, *5* (6), 1110–1128.

(35) Tilley, R. J. *Crystals and Crystal Structures*; John Wiley & Sons, 2020.

(36) Jacques, J.; Collet, A.; Wilen, S. H.; Collet, A. *Enantiomers, Racemates, and Resolutions*; Wiley New York, 1981.

(37) Keene, F. R. *Chirality in Supramolecular Assemblies : Causes and Consequences*; John Wiley & Sons, Ltd: Chichester, West Sussex, 2017.

(38) Viedma, C. Enantiomeric Crystallization from DL-Aspartic and DL-Glutamic Acids: Implications for Biomolecular Chirality in the Origin of Life. *Orig. Life Evol. Biosph.* **2001**, *31*, 501–509.

(39) Kuroda, R.; Mason, S. F. Crystal Structures of Dextrorotatory and Racemic Sodium Ammonium Tartrate. *J. Chem. Soc., Dalton Trans.* **1981**, *6*, 1268-1273.

(40) Pasteur, L. Memoires Sur La Relation Qui Peut Exister Entre La Forme Crystalline et al Composition Chimique, et Sur La Cause de La Polarization Rotatoire. *Compt. rend.* **1848**, *26*, 535–538.

(41) Gal, J. The Discovery of Biological Enantioselectivity: Louis Pasteur and the Fermentation of Tartaric Acid, 1857—a Review and Analysis 150 Yr Later. *Chirality: the pharmacological, biological, and chemical consequences of molecular asymmetry* **2008**, *20* (1), 5–19.

(42) Derewenda, Z. S. On Wine, Chirality and Crystallography. *Acta Crystallogr. A.* **2008**, *64* (1), 246–258.

(43) Kipping, F. S.; Pope, W. J. LXIII.—Enantiomorphism. *J. Chem. Soc., Trans.* **1898**, *73* (0), 606–617.

(44) Viedma, C. Chiral Symmetry Breaking During Crystallization: Complete Chiral Purity Induced by Nonlinear Autocatalysis and Recycling. *Phys. Rev. Lett.* **2005**, *94* (6), 065504.

(45) Petrova, R. I.; Swift, J. A. Selective Growth and Distribution of Crystalline Enantiomers in Hydrogels. *J. Am. Chem. Soc.* **2004**, *126* (4), 1168–1173.

(46) Lee, T.; Lin, Y. K. The Origin of Life and the Crystallization of Aspartic Acid in Water. *Cryst. Growth Des.* **2010**, *10* (4), 1652–1660.

(47) Medina, D. D.; Gedanken, A.; Mastai, Y. Chiral Amplification in Crystallization under Ultrasound Radiation. *Chem. Eur. J.* **2011**, *17* (40), 11139–11142.

(48) Li, W. W.; Spix, L.; De Reus, S. C.; Meekes, H.; Kramer, H. J.; Vlieg, E.; Ter Horst, J. H. Deracemization of a Racemic Compound via Its Conglomerate-Forming Salt Using Temperature Cycling. *Cryst. Growth Des.* **2016**, *16* (9), 5563–5570.

(49) Imaz, I.; Rubio-Martínez, M.; Saletra, W. J.; Amabilino, D. B.; Maspoch, D. Amino Acid Based MetalOrganic Nanofibers. *J. Am. Chem. Soc.* **2009**, *131* (51), 18222–18223.

(50) Wu, H.; Tian, C.; Zhang, Y.; Yang, C.; Zhang, S.; Jiang, Z. Stereoselective Assembly of Amino Acid-Based Metal–Biomolecule Nanofibers. *Chem. Commun.* **2015**, *51* (29), 6329–6332.

(51) T. O. Aiyelabola; D. A. Isabirye; E. O. Akinkunmi; O. A. Ogunkunle; I. A. O. Ojo. Synthesis, Characterization, and Antimicrobial Activities of Coordination Compounds of Aspartic Acid. *J. Chem.* **2016**, *1*, 7317015.

(52) Aiyelabola, T.; Akinkunmi, E.; Ojo, I.; Obuotor, E.; Adebajo, C.; Isabirye, D. Syntheses, Characterization, Resolution, and Biological Studies of Coordination Compounds of Aspartic Acid and Glycine. *Bioinorg. Chem. Appl.* **2017**, *1*, 2956145.

(53) Kraft, A. On the Discovery and History of Prussian Blue. *Bull. Hist. Chem* **2008**, *33* (2), 61–67.

(54) Kraft, A. What a Chemistry Student Should Know about the History of Prussian Blue. *ChemTexts : The Textbook Journal of Chemistry* **2018**, *4* (4), 1–11.

(55) Buser, H.; Schwarzenbach, D.; Petter, W.; Ludi, A. The Crystal Structure of Prussian Blue: $Fe_4[Fe(CN)_6]_3.xH_2O$. *Inorg. Chem.* **1977**, *16* (11), 2704–2710.

(56) Wu, X.; Shao, M.; Wu, C.; Qian, J.; Cao, Y.; Ai, X.; Yang, H. Low Defect $FeFe(CN)_6$ Framework as Stable Host Material for High Performance Li-Ion Batteries. *ACS Appl. Mater. Interfaces.* **2016**, *8* (36), 23706–23712.

(57) Lehn, J. M. Cryptates: Inclusion Complexes of Macropolycyclic Receptor Molecules. *Pure Appl. Chem.* **1978**, *50*, 871–892.

(58) Desiraju, G. R.; Parshall, G. W. Crystal Engineering: The Design of Organic Solids. *Mater. Sci. Monogr.* **1989**, *54*.

(59) Etter, M. C. Encoding and Decoding Hydrogen-Bond Patterns of Organic Compounds. *Acc. Chem. Res.* **1990**, *23* (4), 120–126.

(60) Wells, A. F. *Three-Dimensional Nets and Polyhedra*; Wiley monographs in crystallography; Wiley: New York, 1977.

(61) Hoskins, B. F.; Robson, R. Design and Construction of a New Class of Scaffolding-like Materials Comprising Infinite Polymeric Frameworks of 3D-Linked Molecular Rods. A Reappraisal of the $Zn(CN)_2$ and $Cd(CN)_2$ Structures and the Synthesis and Structure of the

Diamond-Related Frameworks $[N(CH_3)_4][Cu^{I}Zn^{II}(CN)_4]$ and Cu^{I}[4,4',4'',4'''-tetracyanotetraphenylmethane]$BF_4.xC_6H_5NO_2$. *J. Am. Chem. Soc.* **1990**, *112* (4), 1546–1554.

(62) Hoskins, B. F.; Robson, R. Infinite Polymeric Frameworks Consisting of Three Dimensionally Linked Rod-like Segments. *J. Am. Chem. Soc.* **1989**, *111* (15), 5962–5964.

(63) Engel, E. R.; Scott, J. L. Advances in the Green Chemistry of Coordination Polymer Materials. *Green Chem.* **2020**, *22* (12), 3693–3715. https://doi.org/10.1039/d0gc01074j.

(64) Sanchis-Gual, R.; Coronado-Puchau, M.; Mallah, T.; Coronado, E. Hybrid Nanostructures Based on Gold Nanoparticles and Functional Coordination Polymers: Chemistry, Physics and Applications in Biomedicine, Catalysis and Magnetism. *Coord. Chem. Rev.* **2023**, *480*, 215025.

(65) Wang, C.; Zhang, N.; Hou, C.-Y.; Han, X.-X.; Liu, C.-H.; Xing, Y.-H.; Bai, F.-Y.; Sun, L.-X. Transition Metal Complexes Constructed by Pyridine–Amino Acid: Fluorescence Sensing and Catalytic Properties. *Transit. Met. Chem.* **2020**, *45* (6), 423–433.

(66) Puškarić, A.; Dunatov, M.; Jerić, I.; Sabljić, I.; Androš Dubraja, L. Room Temperature Ferroelectric Copper(Ii) Coordination Polymers Based on Amino Acid Hydrazide Ligands. *New J. Chem.* **2022**, *46* (7), 3504–3511.

(67) Chen, S.-C.; Chai, N.-N.; Huang, K.-L.; Tian, F.; Shi, J.; He, M.-Y.; Chen, Q. Microwave Synthesis of 1-D, 2-D, and 3-D Blue Luminescent Coordination Polymers of d^{10} Metals with a New Rigid Tris-Triazole Ligand. *Inorganica Chim. Acta* **2019**, *494*, 187–193.

(68) Sala, A.; Faye Diouf, M. D.; Marchetti, D.; Pasquale, L.; Gemmi, M. Mechanochemical Synthesis and Three-Dimensional Electron Diffraction Structure Solution of a Novel Cu-Based Protocatechuate Metal–Organic Framework. *Cryst. Growth Des.* **2024**, *24* (8), 3246–3255.

(69) Ibrahim, M.; Mahmoud, G. A.-E.; Ali, A. A. M.; Fouad, D. M. Sonochemical Synthesis of Cu (II) Coordination Polymer: Structural Characterization and Antibacterial Activities against Human Pathogenic Bacteria. *Inorg. Chem. Commun.* **2024**, *168*.

(70) Stanley-Gray, J.; Zhang, Z.; Venkataraman, D. Updated Coordination Geometry Table of the D-Block Elements and Their Ions. *J. Chem. Ed.* **2021**, *98* (7), 2476–2481.

(71) Khan, I. U.; Sharif, S.; Sahin, O. Seven-, Eight-, and Ten-Coordinated Cerium (III) with Highly Connective Pyridine-2, 4, 6-Tricarboxylate, Oxalate, and Glycine Ligands. *J. Coord. Chem.* **2013**, *66* (17), 3113–3125.

(72) Furukawa, H.; Cordova, K. E.; O'Keeffe, M.; Yaghi, O. M. The Chemistry and Applications of Metal-Organic Frameworks. *Science (New York, N.Y.)* **2013**, *341* (6149), 1230444.

(73) Li, H.; Wang, K.; Sun, Y.; Lollar, C. T.; Li, J.; Zhou, H.-C. Recent Advances in Gas Storage and Separation Using Metal–Organic Frameworks. *Mater. Today* **2018**, *21* (2), 108–121.

(74) Jiao, L. Metal-Organic Frameworks as Platforms for Catalytic Applications. *Adv. Mater.* **2018**, *30* (37), e1703663.

(75) Yin, H.-Q.; Wang, X.-Y.; Yin, X.-B. Rotation Restricted Emission and Antenna Effect in Single Metal–Organic Frameworks. *J. Am. Chem. Soc.* **2019**, *141* (38), 15166–15173.

(76) Ma, B.; Wu, Y.; Zhang, S.; Wang, S.; Qiu, J.; Zhao, L.; Guo, D.; Duan, J.; Sang, Y.; Li, L.; Jiang, H.; Liu, H. Terbium-Aspartic Acid Nanocrystals with Chirality-Dependent Tunable Fluorescent Properties. *ACS nano* **2017**, *11* (2), 1973–1981.

(77) Gorai, T.; Schmitt, W.; Gunnlaugsson, T. Highlights of the Development and Application of Luminescent Lanthanide Based Coordination Polymers, MOFs and Functional Nanomaterials. *Dalton Trans.* **2021**, *50* (3), 770–784.

(78) Wang, S.; Hou, Y.; Wang, E.; Li, Y.; Xu, L.; Peng, J.; Liu, S.; Hu, C. A Novel Organic-Inorganic Hybrid Material with Fluorescent Emission:$[Cd(PT)(H_2O)]_n$ (PT= phthalate). *New J. Chem.* **2003**, *27* (7), 1144–1147.

(79) Zhang, J.; Kosaka, W.; Kitagawa, Y.; Miyasaka, H. A Metal–Organic Framework That Exhibits CO2-Induced Transitions between Paramagnetism and Ferrimagnetism. *Nat. Chem.* **2021**, *13* (2), 191–199.

(80) Imaz, I.; Rubio-Martínez, M.; García-Fernández, L.; García, F.; Ruiz-Molina, D.; Hernando, J.; Puntes, V.; Maspoch, D. Coordination Polymer Particles as Potential Drug Delivery Systems. *Chem. Commun.* **2010**, *46* (26), 4737–4739.

(81) An, H.; Li, M.; Gao, J.; Zhang, Z.; Ma, S.; Chen, Y. Incorporation of Biomolecules in Metal-Organic Frameworks for Advanced Applications. *Coord. Chem. Rev.* **2019**, *384*, 90–106. https://doi.org/10.1016/j.ccr.2019.01.001.

(82) Mizutani, M.; Maejima, N.; Jitsukawa, K.; Masuda, H.; Einaga, H. An Infinite Chiral Single-Helical Structure Formed in Cu(II)-L-/D-Glutamic Acid System. *Inorg. Chim. Acta* **1998**, *283* (1), 105–110.

(83) Zou, Q.; Yan, X. Amino Acid Coordinated Self-Assembly. *Chem. Eur. J.* **2018**, *24* (4), 755.

(84) Imaz, I.; Rubio-Martinez, M.; An, J.; Sole-Font, I.; Rosi, N. L.; Maspoch, D. Metal–Biomolecule Frameworks (MBioFs). *Chem. Commun.* **2011**, *47* (26), 7287–7302.

(85) Wang, S.; Zhao, Y.; Zhang, Z.; Zhang, Y.; Li, L. Recent Advances in Amino Acid-Metal Coordinated Nanomaterials for Biomedical Applications. *Chin. J. Chem. Eng.* **2021**, *38*, 30–42.

(86) Li, C.; Deng, K.; Tang, Z.; Jiang, L. Twisted Metal-Amino Acid Nanobelts: Chirality Transcription from Molecules to Frameworks. *J. Am. Chem. Soc.* **2010**, *132* (23), 8202.

(87) Pu, F.; Liu, X.; Xu, B.; Ren, J.; Qu, X. Miniaturization of Metal–Biomolecule Frameworks Based on Stereoselective Self-Assembly and Potential Application in Water Treatment and as Antibacterial Agents. *Chem. Eur. J.* **2012**, *18* (14), 4322–4328.

(88) Zhu, Y.; Lu, M.; Gao, F.; Zhou, C.; Jia, C.; Wang, J. Role of Tailor-Made Additives in Crystallization from Solution: A Review. *Ind. Eng. Chem. Res.* **2023**, *62* (12), 4800–4816.

(89) Addadi, L.; van Mil, J.; Gati, E.; Lahav, M. Amplification of Optical Activity by Crystallization in the Presence of Tailor-Made Additives. The "Inversion Rule"; Springer, 1981, 355–364.

(90) Addadi, L.; Berkovitch-Yellin, Z.; Domb, N.; Gati, E.; Lahav, M.; Leiserowitz, L. Resolution of Conglomerates by Stereoselective Habit Modifications. *Nature* **1982**, *296* (5852), 21–26.

(91) Coquerel, G. Preferential Crystallization. *Novel optical resolution technologies* **2007**, 1–51.

(92) Harada, K. Optical Resolution of a DL-Amino-Acid by a Stereoselective Ligand Exchange Reaction. *Nature* **1965**, *205* (4971), 590–591.

(93) Harada, K.; Tso, W. Optical Resolution of Aspartic Acid by Using Copper Complexes of Optically Active Amino Acids. *Bull. Chem. Soc. Jpn.* **1972**, *45* (9), 2859–2862.

(94) Lahav, M.; Leiserowitz, L. The Story Behind the Link between Molecular Chirality and Crystal Shape. *Helv. Chim. Acta* **2023**, *106* (5), e202200172.

(95) Weissbuch, I.; Lahav, M.; Leiserowitz, L. Crystal Morphology Control with Tailor-Made Additives; A Stereochemical Approach; Elsevier Science B.V, **2001**, 381–400.

(96) Sharma, R.; Bisen, D.; Shukla, U.; Sharma, B. X-Ray Diffraction: A Powerful Method of Characterizing Nanomaterials. *Recent Res. Sci. Technol.* **2012**, *4* (8), 77–79.

(97) Ameh, E. A Review of Basic Crystallography and X-Ray Diffraction Applications. *Int. J. Adv. Manuf. Technol.* **2019**, *105* (7), 3289–3302.

(98) Shinoda, K.; Matsubara, E.; Waseda, Y. *X-Ray Diffraction Crystallography: Introduction, Examples and Solved Problems*, 1. Aufl.; Springer-Verlag: Berlin, Heidelberg, 2011.

(99) Font Bardia, M. M.; Alcobé i Ollé, X. X-Ray Single Crystal and Powder Diffraction: Possibilities and Applications. *Capítol del llibre: Handbook of instrumental techniques for materials, chemical and biosciences research, Centres Científics i Tecnològics. Universitat de Barcelona, Barcelona, 2012. Part I. Materials technologies (MT), MT. 9, 14 p.* **2012**.

(100) Cotton, A. Dispersion Rotatoire Anomale des Corps Absorbants. *Compt. rend* **1895**, *120*, 1044.

(101) Cotton, A. Absorption Inégale des Rayons Circulaires Droit et Gauche Dans Certains Corps Actifs. *Compt. Rend.* **1895**, *120*, 989–991.

(102) Ahluwalia, V. K. *Stereochemistry of Organic Compounds*; Springer: Cham, 2022.

(103) Ding, L.; Lin, L.; Liu, C.; Li, H.; Qin, A.; Liu, Y.; Song, L.; Zhang, H.; Tang, B. Z.; Zhao, Y. Concentration Effects in Solid-State CD Spectra of Chiral Atropisomeric Compounds. *New J. Chem.* **2011**, *35* (9), 1781–1786.

(104) Kuroda, R.; Honma, T. CD Spectra of Solid-State Samples. *Chirality (New York, N.Y.)* **2000**, *12* (4), 269–277.

(105) Castiglioni, E.; Biscarini, P.; Abbate, S. Experimental Aspects of Solid-State Circular Dichroism. *Chirality (New York, N.Y.)* **2009**, *21* (Suppl. 1E), E28–E36.

(106) McLaughlin, D. T.; Nguyen, T. P. T.; Mengnjo, L.; Bian, C.; Leung, Y. H.; Goodfellow, E.; Ramrup, P.; Woo, S.; Cuccia, L. A. Viedma Ripening of Conglomerate Crystals of Achiral Molecules Monitored Using Solid-State Circular Dichroism. *Cryst. Growth & Des.* **2014**, *14* (3), 1067–1076.

(107) Chakraborty, G.; Park, I.-H.; Medishetty, R.; Vittal, J. J. Two-Dimensional Metal-Organic Framework Materials: Synthesis, Structures, Properties and Applications. *Chem. Rev.* **2021**, *121* (7), 3751–3891.

(108) Cruz, C.; Gonzalez, C.; Rubio, F.; Erices, J.; Wrighton-Araneda, K.; Cortés-Arriagada, D.; Venegas-Yazigi, D.; Audebrand, N.; Paredes-García, V. Chiral 1D Metal–Organic Materials Based on Cu(II) and Amino Acid Schiff Bases. *Cryst. Growth & Des.* **2022**, *22* (1), 237–250.

(109) Puigmartí-Luis, J.; Rubio-Martínez, M.; Hartfelder, U.; Imaz, I.; Maspoch, D.; Dittrich, P. S. Coordination Polymer Nanofibers Generated by Microfluidic Synthesis. *J. Am. Chem. Soc.* **2011**, *133* (12), 4216–4219.

(110) Zhou, Q.; Sun, R.; Ren, Y.; Tian, R.; Yang, J.; Pang, H.; Huang, K.; Tian, X.; Xu, L.; Tang, Y. Reactive Template-derived Interfacial Engineering of CoP/CoO Heterostructured Porous Nanotubes towards Superior Electrocatalytic Hydrogen Evolution. *Carbon Energy* **2023**, *5* (1).

(111) Shemchuk, O.; Grepioni, F.; Leyssens, T.; Braga, D. Chiral Resolution via Cocrystallization with Inorganic Salts. *Isr. J. Chem.* **2021**, *61* (9–10), 563–572.

(112) Coquerel, G. Preferential Crystallization. *Novel optical resolution technologies* **2007**, 1–51.

(113) Springuel, G.; Leyssens, T. Innovative Chiral Resolution Using Enantiospecific Co-Crystallization in Solution. *Cryst. Growth & Des.* **2012**, *12* (7), 3374–3378.

(114) Tang, B.; Wang, W.; Hou, H.; Liu, Y.; Liu, Z.; Geng, L.; Sun, L.; Luo, A. A β-Cyclodextrin Covalent Organic Framework Used as a Chiral Stationary Phase for Chiral Separation in Gas Chromatography. *Chin. Chem. Lett.* **2022**, *33* (2), 898–902.

(115) Lee, H. L.; Hung, Y. L.; Amin, A.; Pratama, D. E.; Lee, T. Green and Strategic Approach for Chiral Resolution by Diastereomeric Salt Formation: The Study of Racemic Ibuprofen. *Ind. Eng. Chem. Res.* **2023**, *62* (4), 1946–1957.

(116) Harada, K. The Optical Resolution of DL-Aspartic Acid, DL-Glutamic Acid, DL-Asparagine and DL-Glutamine by Preferential Crystallization. *Bull. Chem. Soc. Jpn.* **1965**, *38* (9), 1552–1555.

(117) Harada, K.; Iwasaki, T. Optical Resolution of DL-Aspartic Acid in The Presence of Optically Active Amino Acid and Copper (II) Ion. *Chem. Lett.* **1972**, *1* (11), 1057–1059.

(118) Van Mil, J.; Addadi, L.; Gati, E.; Lahav, M. Useful Impurities for Optical Resolution. 4. Attempted Amplification of Optical Activity by Crystallization of Chiral Crystals of Photopolymerizing Dienes in the Presence of Their Topochemical Products. *J. Am. Chem. Soc.* **1982**, *104* (12), 3429–3434.

(119) Weissbuch, I.; Addadi, L.; Leiserowitz, L.; Lahav, M. Total Asymmetric Transformations at Interfaces with Centrosymmetric Crystals: Role of Hydrophobic and Kinetic Effects in the Crystallization of the System Glycine/. Alpha.-Amino Acids. *J. Am. Chem. Soc.* **1988**, *110* (2), 561–567.

(120) Kongsamai, P.; Flood, C.; Horst, J. H.; Flood, A. E. Particle Size Distributions and Performance of Preferential Crystallization of L-Asparagine·H_2O with Tailor-Made Additives. *Chem. Eng. Technol.* **2018**, *41* (6), 1173–1179.

(121) Gou, L.; Lorenz, H.; Seidel-Morgenstern, A. Investigation of a Chiral Additive Used in Preferential Crystallization. *Cryst. Growth & Des.* **2012**, *12* (11), 5197–5202.

(122) Shtukenberg, A. G.; Punin, Y. O.; Gunn, E.; Kahr, B. Spherulites. *Chem. Rev.* **2012**, *112* (3), 1805–1838.

(123) Rahbani, J.; Behzad, A. R.; Khashab, N. M.; Al-Ghoul, M. Characterization of Internal Structure of Hydrated Agar and Gelatin Matrices by cryo-SEM. *Electrophoresis* **2013**, *34* (3), 405–408.

(124) Dalton, J. B.; Schmidt, C. L. The Solubilities of Certain Amino Acids in Water, the Densities of Their Solutions at Twenty-Five Degrees, and the Calculated Heats of Solution and Partial Molal Volumes. *J. Biol. Chem.* **1933**, *103* (2), 549–578.

(125) Khan, S. Reaction-Diffusion Formation of Copper Aspartate in Gel. **2022**.

(126) Ostromisslensky, I. Untersuchungen Im Gebiete Der Spiegelbildisomerie. *Berichte der deutschen chemischen Gesellschaft* **1908**, *41* (2), 3035–3046.

Appendix

ARTICLE

Towards Spatiotemporal Resolution of Copper Aspartate in Gel

Poh Ying Fong,[a] Sehrish Khan,[a] Hatem M. Titi,[b] Manal Ammar,[c] Fiorenzo Vetrone,[d] Mazen Al-Ghoul[c]* and Louis A. Cuccia[a]*

Received 00th January 20xx,
Accepted 00th January 20xx

DOI: 10.1039/x0xx00000x

Chiral resolution is essential in the pharmaceutical and food industries and materials science due to the unique properties of enantiomers. This study explores the coordination polymerization of homochiral (L- and D-) and racemic (DL-) copper aspartate (CuAsp) and spatiotemporal resolution of racemic aspartic acid (DL-Asp) using L- and D-proline (Pro)-copper complexes as tailor-made additives (TMAs). The research is conducted within the reaction-diffusion framework (RDF) in a quasi-one-dimensional (1D) agar gel system. RDF, a far-from-equilibrium process, drives self-organization by creating a supersaturation gradient, which translates into a gradient of crystal sizes and leads to the formation of CuAsp coordination polymers with spherulitic morphology. This spatial self-organization occurs across multiple scales, from the macroscopic crystal structures to the microscopic coordination polymers. Solid-state circular dichroism (CD) and powder X-ray diffraction (PXRD) analyses confirmed the chiral nature and crystalline phases of the CuAsp polymers, with DL-CuAsp crystallizing as a conglomerate. Inspired by Kaoru Harada's seminal work on the resolution of DL-Asp in solution using L- and D-Pro-copper complexes, the preferential crystallization, following the 'rule of reversal', was observed. Crystalline CuAsp near the liquid-gel interface exhibited the opposite configuration to that of the TMA. Variability in chirality was noted further from the interface due to concentration gradients, a characteristic feature of the RDF. These findings emphasize the utility of the RDF, combined with the rule of reversal, as an innovative approach for achieving chiral resolution in conglomerate crystalline systems, with potential implications for broader enantioselective separation strategies.

Introduction

Coordination polymers (CPs) are versatile metal-ligand compounds that can form one-, two- or three-dimensional structures.[1,2] Their ability to incorporate various metals and ligands has led to a wide range of applications, including magnetism,[3] gas adsorption,[4] catalysis,[5] luminescence,[6] and drug delivery.[7] Recent advancements have focused on chiral CPs due to their complex architectures and potential in enantioselective separation and asymmetric catalysis.[2,8] The ideal enantiopure ligand should be accessible, cost-effective, environmentally friendly, and exhibit flexible coordination behavior.[2] Strategic selection and design of chiral ligands are crucial for developing multifunctional chiral CPs. Amino acids, in particular, have garnered significant attention for their efficient coordination with metal ions.[9–11] Their distinct amino, carboxylate, and side chain functional groups render them ideal for complexation.[12,13] Several research groups have demonstrated the fabrication of 1D nanostructures, such as nanofibers,[9,10,14] nanowires,[15] nanobelts,[16] and nanorods[11] from metal-amino acid assemblies. For example, Imaz *et al*. successfully prepared CuAsp nanofibers at the interface of a Cu^{2+} solution with a water/ethanol mixture containing deprotonated L- or D-Asp. Similarly, Pu *et al*. and Wu *et al*. demonstrated the self-assembly of CuGlu,[10,17] CuAsp,[10] and CuAmi[10] at room temperature. Their studies revealed that crystallization is driven by coordination between deprotonated amino acids and Cu^{2+} metal ions in a proposed square planar coordination geometry. Furthermore, amino acid chirality influences supramolecular self-assembly.[10,17]

Chiral resolution is crucial in the pharmaceutical and food industries, where enantiopure products are essential.[18] Various techniques have been developed to resolve conglomerate crystalline systems,[19–23] with preferential crystallization (PC) being particularly effective in resolving conglomerate crystals by seeding a supersaturated solution with the preferred enantiomer.[20] Pioneering work by Kaoru Harada more than 50 years ago demonstrated the successful separation of DL-Asp, DL-Glu, and DL-Asn using homochiral amino acid-copper complexes.[24–27] Addadi *et al*. later introduced the *'rule of reversal'* to rationalize how the enantiomer with the opposite configuration crystallizes preferentially in the presence of homochiral tailor-made additives (TMAs).[28] Homochiral TMAs share a similar structure with the solute molecules, allowing for enantioselective adsorption, which in turn hinders nucleation and crystal growth of one enantiomer.[19,28–30] More recently, Kongsamai *et al*. explored the resolution of DL-Asn•H_2O using D-Asp and D-Glu,[31] while Gou *et al*. and Zou *et al*. reported

[a] Department of Chemistry and Biochemistry, Concordia University, 7141 Sherbrooke Street West, H4B 1R6 Montreal, Canada
[b] Department of Chemistry, McGill University, 801 Sherbrooke Street West, H3A 0B8 Montreal, Canada
[c] Department of Chemistry, American University of Beirut, P.O. Box 11-0236, Riad El-Solh, 1107 2020 Beirut, Lebanon
[d] Centre Énergie, Matériaux et Télécommunications, Institut National de la Recherche Scientifique, Université du Québec, 1650 Boul. Lionel-Boulet, J3X 1P7 Varennes, Canada

† Footnotes relating to the title and/or authors should appear here.
Supplementary Information available: [details of any supplementary information available should be included here]. See DOI: 10.1039/x0xx00000x

higher product yields and purity of (*S*)-mandelic acid and L-norvaline, respectively, using PC with TMAs.[32,33] The reaction-diffusion framework (RDF) offers a robust platform for investigating chiral resolution and pattern formation in coordination polymers, functioning under far-from-equilibrium conditions.[34] In this framework, a metal ion such as Cu^{2+} diffuses through a gel medium containing a chiral ligand (homochiral or racemic), creating a dynamic concentration gradient. This gradient drives the nucleation and growth of coordination polymers, resulting in highly organized structures.[35,36] What distinguishes RDF is its ability to facilitate self-organization at multiple scales. While distinct patterns, such as Liesegang rings or spherulites, emerge at the macroscopic level, there is also concurrent self-organization at the microscopic scale, where molecular interactions dictate the arrangement of atoms within the coordination polymer.[35,37] This hierarchical self-organization is a hallmark of far-from-equilibrium systems, where the continuous influx of energy or matter drives complexity and order.[34]

One of the remarkable features of RDF-based self-organization is its capacity for selective spatial segregation. As the system evolves, distinct bands of precipitated material form in the gel.[37] This spatial organization not only allows for the segregation of particles based on size but also provides a strategy for attempting to segregate various chiral compounds into these bands. Through the careful control of reaction conditions, such as ion concentration and ligand chirality, this method may enable the separation of enantiomers *in situ*, as different chiral species preferentially nucleate and crystallize in specific bands. This capability opens new possibilities for chiral resolution and enantioselective separations in structured environments.

In the present study, the diffusion of Cu^{2+} into a gel matrix containing deprotonated aspartate ligand results in the formation of blue spherulites made of a coordination polymer of CuAsp. This process exemplifies self-organization across length scales, as the spherulites exhibit macroscopic symmetry, while the chiral nature of the ligands dictates their microscopic arrangement. The far-from-equilibrium nature of the RDF ensures that the system does not settle into a static, low-energy arrangement but instead continues to evolve,[38] allowing for the emergence of intricate spatial patterns and chiral resolution.

Inspired by the work of Imaz *et al*.[9] and Harada *et al*.[27], this study aims to explore the chiral crystallization of L- and D-aspartate and the spatiotemporal resolution of DL-aspartate using homochiral additives in an agar gel medium. Through the application of the RDF, this work seeks to uncover new insights into the mechanisms driving chiral resolution and the role of amino acid chirality in the formation of coordination polymers. The findings contribute to the broader understanding of chiral materials design and the development of novel techniques for enantioselective separation in structured environments.

Results and discussion

Coordination polymerization and characterization of L-, D-, and DL-CuAsp in agar gel

Research on the coordination polymerization of CuAsp has traditionally focused on solution-based self-assembly processes.[9,10] However, to our knowledge, the coordination polymerization of CuAsp in hydrogels has yet to be reported. Taking advantage of the RDF, we successfully achieved the periodic precipitation (Liesegang banding) of L-, D-, and DL-CuAsp coordination polymers in a 1D agar gel system (Fig. 1). The diffusion of $Cu(NO_3)_2 \cdot 3H_2O$ solution, serving as the outer electrolyte, into the gel containing deprotonated Asp led to the formation of distinct blue spherulites. The temporal evolution of this periodic precipitation is depicted in Fig. S1, ESI†.

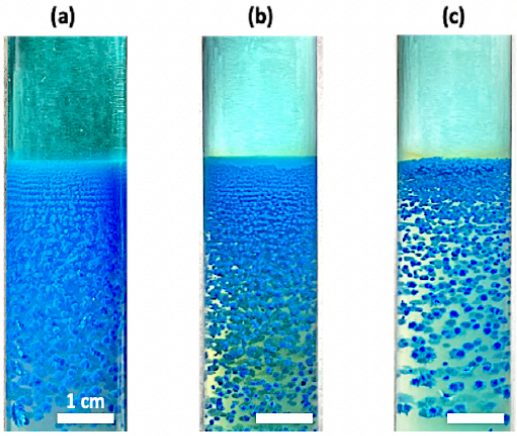

Figure 1 Periodic precipitation of (a) L-, (b) D-, and (c) DL-CuAsp in a 1D agar gel system with the initial concentrations of the outer electrolyte: [Cu^{2+}] = 300 mM; and the inner electrolyte: [Agar] = 1%, [Asp] = 50 mM, [NaOH] = 100 mM at *ca.* 22 °C.

A notable 6-fold higher concentration of Cu^{2+} outer electrolyte was used to create a high level of supersaturation at the liquid-gel interface, facilitating rapid diffusion.[35] This setup established a concentration gradient, where supersaturation decreased progressively with distance from the interface.[35] At the interface, the highest concentration of Cu^{2+} ions leads to rapid nucleation due to high supersaturation. Since nucleation dominates crystal growth at high supersaturation, many small spherulites form simultaneously, competing for available ions (Fig. 2a). This results in a high number of nuclei, limiting the growth of each crystal. Furthermore, in the middle zone, the supersaturation decreases as Cu^{2+} ions diffuse further from the liquid-gel interface. Here, nucleation slows down, allowing the spherulites that form to grow larger as crystal growth begins to dominate over nucleation. This creates a balance between nucleation and crystal growth, leading to intermediate particle sizes (Fig. 2a). When Cu^{2+} ions reach the bottom zone, supersaturation is significantly lower. Fewer nuclei form in this region, allowing the already-formed spherulites to grow larger due to reduced ion competition. Crystal growth is the dominant process, leading to the formation of large spherulites. (Fig. 2a).

Spherulite formation is a common phenomenon in RDFs.[33] It begins with the nucleation at a single point. Once nucleation occurs, anisotropic forces drive the directional growth of nanofibers of CuAsp coordination polymers away from the nucleus, resulting from the established concentration gradient. As the CuAsp nanofibers grow, they align radially from the nucleation site, with the diffusion flux continuing to supply material that contributes to the growth of the fibers. This results in the formation of bundles of nanofibers, where each bundle maintains a preferred orientation driven by the anisotropy in the reaction environment.[33] These nanofiber bundles progressively organize into a hierarchical structure, with the inner layers of the spherulite formed first, followed by the addition of outer layers as the reaction continues. The hierarchical organization is a crucial feature of spherulitic growth, where small-scale units such as nanofibers are integrated into progressively larger structures, ultimately forming a spherulite with a radial, starburst-like morphology. This self-organization across multiple scales, from nanofibers to macroscopic crystals, is a hallmark of the far-from-equilibrium conditions maintained in the reaction-diffusion system.[33] The continuous supply of Cu^{2+}, combined with anisotropic forces, ensures that the spherulite grows symmetrically and retains its distinctive hierarchical architecture. Thus, RDF not only promotes radial growth but also fosters the creation of well-ordered, complex structures that are characteristic of spherulites. This described mechanism is clearly illustrated in the SEM micrographs where the CuAsp nanofibers are densely aggregated around the spherulite's nucleus (Fig. 2b (i-iii)). Interestingly, although the overall size of the spherulites increased (from 0.3 to 1.2 mm; Fig. 2a), the diameters of the nanofibers progressively decreased along the reaction tube (Fig. 2b (iv-vi)), ranging from 100 nm near the interface to 50 nm near the diffusion front, aligning closely with homochiral CuAsp nanofibers reported by Imaz *et al.*[9] This decrease in fiber thickness can also be attributed to the reduction of supersaturation along the tube. For example, as nucleation near the gel interface is abundant, the supply of ions is divided among many forming nuclei. This allows the nanofibers to grow thicker due to the abundance of material at the initial stages of fiber formation. This fact is reversed further away from the interface.

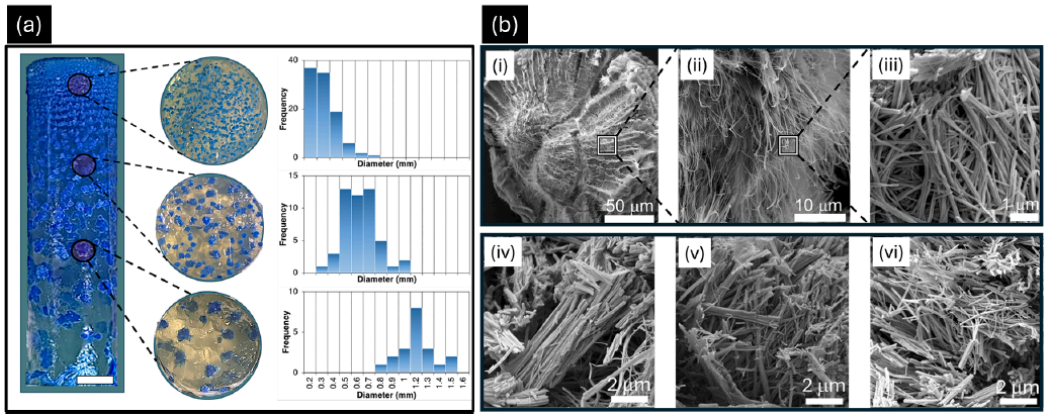

Figure 2 (a) Periodic precipitation and particle size distribution of D-CuAsp spherulites in a 1D agar gel system. Slices of the gel column highlight three distinct zones formed due to the reaction-diffusion process: the liquid-gel interface, middle zone, and bottom zone, which exhibit progressively larger spherulites, as shown in the accompanying flowchart. Near the liquid-gel interface, the spherulites are the smallest, with a size range of 0.3 to 0.5 mm in diameter, due to the high supersaturation of Cu^{2+} ions, which promotes rapid nucleation. This leads to the formation of a large number of small crystals competing for ions. In the middle zone, where supersaturation is moderate, the spherulites reach intermediate sizes, ranging from 0.6 to 0.9 mm in diameter, as nucleation slows down and crystal growth becomes more dominant. Fewer nucleation events occur in the bottom zone, with the lowest supersaturation, allowing existing crystals to grow to their largest size, with diameters between 1.0 and 1.2 mm. The flowchart illustrates the size distribution across the three zones, clearly demonstrating the progression of spherulite growth as supersaturation decreases with distance from the liquid-gel interface. (b) Scanning electron microscopy (SEM) images of a D-CuAsp spherulite cross-section from the reaction tube. Panels (i-iii) show the densely packed nanofibers that make up the spherulite at various magnifications. Panels (iv-vi) depict the progressive reduction in nanofiber diameters along the reaction tube, with 100 nm near the liquid-gel interface (iv), decreasing to 50 nm near the diffusion front (vi). This nanofiber size reduction correlates with the changing supersaturation levels, as smaller nanofibers are observed in regions where nucleation rates are higher (closer to the interface), while larger, more developed fibers appear further along the diffusion front, where growth dominates. Initial concentrations of the outer electrolyte: [Cu^{2+}] = 300 mM; inner electrolyte: [Agar] = 1%, [D-Asp] = 50 mM, [NaOH] = 100 mM; at *ca.* 22 °C. Scale = 1 cm.

Noteworthy differences in precipitation Liesegang patterns were observed when comparing homochiral L-CuAsp or D-CuAsp to DL-CuAsp. Homochiral CuAsp spherulites formed densely packed arrays, while DL-CuAsp spherulites were more sparsely distributed. Liesegang bands result from periodic precipitation in reaction-diffusion systems as the reactant concentration fluctuates due to diffusion and supersaturation cycles.[38] The spacing of these bands is directly influenced by the nucleation rate, which in turn is affected by the solubility of the precipitating compound. For homochiral CuAsp, the lower solubility of L- or D-Asp (between 4 mg/mL and 5 mg/mL at 25 °C)[39,40] means that precipitation occurs more readily, leading to closely spaced Liesegang bands because the system reaches the necessary concentration for nucleation frequently along the diffusion front. This rapid nucleation results in shorter intervals between precipitation bands as new crystals form in quick

succession. For DL-CuAsp, the higher solubility of DL-Asp (7.78 mg/mL at 25 °C),[39,40] means that the system requires a greater concentration of Cu^{2+} ions to reach supersaturation, leading to wider spacing between precipitation events. This results in more sparsely distributed Liesegang bands, as nucleation happens less frequently due to the slower approach to supersaturation in the higher-solubility DL-Asp solution. Additionally, the slower formation of coordination complexes in DL-CuAsp, compared to homochiral CuAsp, can be attributed to the incompatibility between L- and D-Asp in nanofiber formation. This suggests that CuAsp crystallizes as a conglomerate (*vide infra*). Wu *et al.* demonstrated that mixing equal concentrations of Cu^{2+} solution with deprotonated L- or D-Asp leads to rapid gelation, while DL-Asp forms a blue gel more slowly at the same concentration, indicating faster assembly rates for homochiral CuAsp than for DL-CuAsp.[9,10]

Powder X-ray diffraction (PXRD) analysis confirmed the crystalline nature of CuAsp (Fig. 3a). Both L- and D-CuAsp exhibit the same diffraction patterns, in agreement with Wu *et al.*[10], indicating that both forms share the same crystal packing. Remarkably, DL-CuAsp gave the same diffraction pattern. The identical PXRD patterns observed for all three forms (L-, D-, and DL-CuAsp) imply that the coordination environment around Cu^{2+} and the packing arrangement remain consistent regardless of whether the system is homochiral or racemic. This uniformity suggests that the presence of both L-and D- in DL-CuAsp does not disrupt the crystal structure but rather crystallizes in a conglomerate. Unfortunately, a detailed analysis of the structural connectivity was not feasible due to their sub-200 nm diameter nanofibers and the inability to obtain large single crystals. Imaz and coworkers suggested that the CuAsp nanofibers were aligned in 1D $[Cu(Asp)(H_2O)_x]_n$ polymeric chains[9], while Wu *et al.* later proposed that the CuAsp coordination complex adopt a square-planar geometry, where the Cu^{2+} ion is bonded to the α-carboxylate oxygen and amino nitrogen atoms of Asp, forming a typical five-membered glycinate chelate ring.[10]

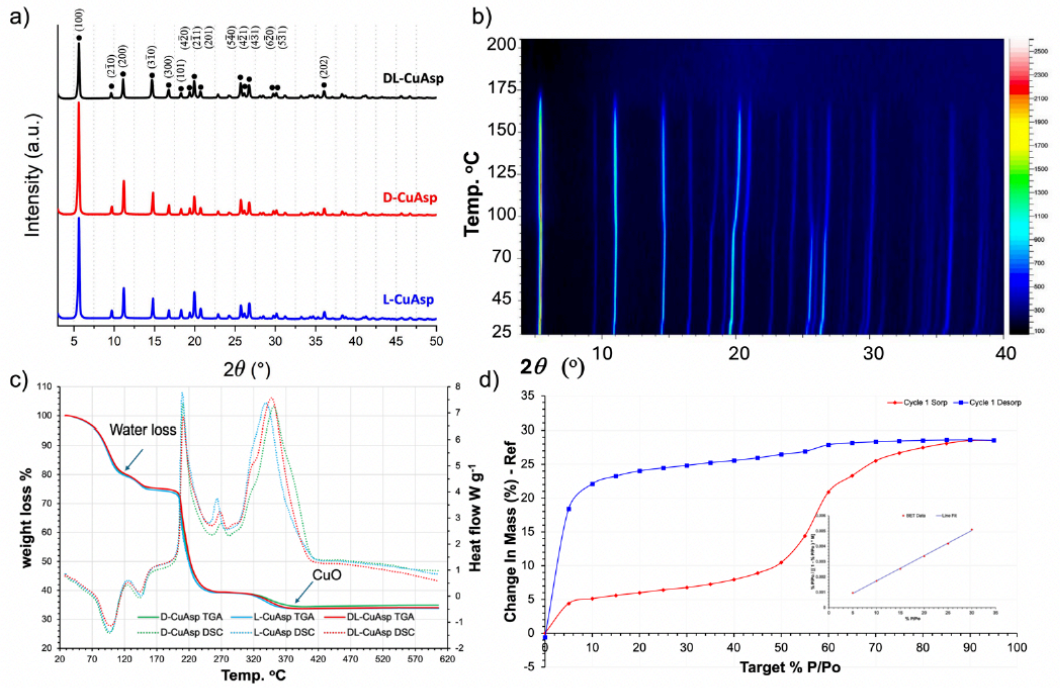

Figure 3 (a) PXRD of L-, D-, and DL-CuAsp. (b) VTPXRD of L-CuAsp between 25 - 200 °C, revealing changes at high angles, where the overall structure remains intact up to 170 °C. (c) Comparison of TGA and DSC thermograms for the synthesized L-, D- and DL-CuAsp. The observed weight loss of water and the residue range between 24.7 - 25.2 % and 33.8 - 34.8 %, respectively. These values suggest three water molecules totaling 27.0 %, which is off by *ca.* 2 %. At the same time, the residue of 29.8 % corresponds to CuO, which is off by 4 - 5%. (d) DVS of L-CuAsp shows a water uptake of 28.5 %, and the BET fit calculation is between the range of 5 - 30 RH%.

Attenuated total reflectance Fourier-transform infrared (ATR-FTIR) characterization was performed to probe the assembly process of the nanofibers. The coordination of aspartate with Cu^{2+} is evident when comparing the IR spectra of the starting material (L-aspartic acid) with the coordination polymers L-, D-, and DL-CuAsp (Fig. S2, ESI†). A detailed analysis of the IR spectrum of L-aspartic acid reveals characteristic peaks at 3132 cm^{-1} (νN–H), 3000 cm^{-1} (νC–H), 1680 cm^{-1} (νC=O), 1612 cm^{-1} (νCOOH), and 1070 cm^{-1} (νC–N). Additional peaks at 1344 cm^{-1} and 1210 cm^{-1} correspond to C–H

stretching and CH_2 twisting, respectively. Peaks at 890 cm^{-1}, 640 cm^{-1}, and 475 cm^{-1} are attributed to C–C stretching, COOH bending, and NH_3 torsion vibrations, respectively. Deprotonation of the COOH groups, prior to coordination with Cu^{2+}, is confirmed by the shift of the C=O stretching vibration to 1580 cm^{-1}.[10] The band observed at 675 cm^{-1} is attributed to Cu–O stretching, while the band at 420 cm^{-1} in all three coordination polymers corresponds to the asymmetric stretching mode of the Cu–N bonds (395 cm^{-1} - 455 cm^{-1}).[41,42] All three CPs, L-, D-, and DL-CuAsp CPs, exhibit virtually identical IR spectra.

All attempts to obtain a single crystal of the L-CuAsp CP failed. Therefore, we conducted further experiments to shed light on the underlying CuAsp structure. The IR shows a broad peak in the range of 2800 - 3600 cm^{-1}, corresponding to the presence of water molecules. To confirm the presence of water as part of the structure, the thermal stability of the compound L-CuAsp was investigated using variable temperature PXRD (VTPXRD) and thermogravimetric analysis (TGA). The VTPXRD reveals changes in 2θ, especially at 18.1°, 19.2°, 19.5°, 25.4°, and 26.2°, starting when the sample was heated from 90 °C until 125 °C. These changes may correspond to the loss of solvents from the structure. The temperature and experimental preparation suggest the loss of free water molecules at around 90 °C, while the coordinated water molecules can be released above 110 °C (Fig. 3b). The structure remains intact up to 170 °C, followed by the material's complete amorphization. TGA was used to investigate the number of water molecules in the structure (Fig. 3c). The weight loss due to water ends at 130 °C, with a weight loss drop of approximately 27 %. The material then shows thermal stability between 170 - 200 °C, which aligns very well with the amorphization of the compound, as observed in the VTPXRD. The decomposition led to the formation of CuO at 370 °C. Interestingly, the calculated number of water molecules from the weight loss is approximately four. It is worth mentioning that the pure enantiomers and the racemate have the same profile and weight loss, indicating they have a similar structure, which agrees with conglomerate crystallization and supports the results from the PXRD analysis. The water uptake of a dry sample of L-CuAsp was also investigated using Dynamic Vapour Sorption (DVS, Fig. 3d). First, the CP was activated by heating the sample at 100 °C for 4 hours; then, the dried sample was placed on the DVS, and the relative humidity was gradually increased starting from 0 RH% up to 95 RH%, with increments of 5 RH%. The compound shows a water uptake and desorption of 28.5%, which agrees with the TGA results. Based on the DVS results, the surface area (SA) calculation using the Brunauer-Emmett-Teller (BET) method shows an SA of 170.5 m^2/g.

To assess the porosity, N_2 adsorption-desorption isotherm of DL-CuAsp was measured at 77 K (Fig. S3, ESI†), exhibiting a Type IV isotherm. The initial rapid adsorption observed at low relative pressures corresponds to the monolayer formation, indicating the rapid filling of mesopores, as evidenced by the first knee in the isotherm. As the relative pressure increased, more adsorption occurred, leading to multilayer formation. A steep spike was observed, indicating capillary condensation within the mesopores. The desorption isotherm exhibited an H3 hysteresis loop, typically observed in materials that form aggregates of fibers, resulting in slit-like mesoporous structures.[43] The BET surface area and pore width for DL-CuAsp were calculated to be 21 m^2/g and *ca.* 190 Å, respectively (Table 1, ESI†). These results suggested the material has a relatively low surface area and is mesoporous.[43]

Solid-state circular dichroism (CD) was employed to investigate the chirality of CuAsp polymers (Fig. 4). L-CuAsp exhibited a positive Cotton effect, while D-CuAsp showed a negative Cotton effect at 745 nm, with both crossing at 655 nm, indicating the presence of a chiral coordination sphere of the Cu^{2+} with chiral Asp.[9] In contrast, DL-CuAsp showed no Cotton effect, nor did the individual DL-CuAsp spherulites (Fig. S4, ESI†). This observation apparently contradicts crystallization as a conglomerate, as indicated by the identical PXRD pattern shared by DL- and homochiral CuAsp. Herein, it is believed that the nanofibers within each DL-CuAsp spherulite are individually homochiral. Still, their aggregation presents racemic-like behavior in CD analysis, reconciling the PXRD data with the lack of chiral signals in the CD results. These findings demonstrate that RDF enables the periodic precipitation of L-, D-, and DL-CuAsp coordination polymers in agar gel.

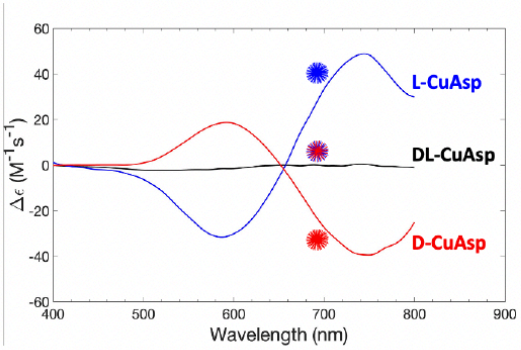

Figure 4 Solid-state CD of L- (blue), D- (red), and DL-CuAsp (black). The L- and D-CuAsp are made of pure blue and pure red nanofibers, respectively. However, the DL-CuAsp is composed of a mixture of L- (blue) and D- (red) nanofibers.

Chiral resolution of DL-Asp in the presence of homochiral proline (Pro)-copper complexes in agar gel

Homochiral L- and D-Pro-copper complexes as tailor-made additives (TMAs) were used to achieve spatiotemporal chiral resolution of DL-Asp in the gel. The diffusion of homochiral Pro-copper complexes (L-Pro or D-Pro) into the agar gel containing DL-Asp results in spatially distinct bands of CuAsp coordination polymers. The spatial organization is guided by the concentration gradients established by the RDF, which controls where and how the chiral molecules crystallize. Drawing from Harada's research, when the mole ratio of the chiral amino acid to DL-Asp is less than 1, the second crop of crystals maintains the same configuration as the first crop. Yet, when the mole ratio is equal to or greater than 1, the configuration of the second crop reverses relative to the first crop.[27] To confirm proper complexation, UV-Vis absorption analysis was performed, revealing an adsorption shift from 800 nm to approximately 725

nm regardless of the concentration of Pro, indicating the formation of a Pro-Cu(II) complex in solution (Fig. S5, ESI†).

After diffusing chiral Pro-copper complexes into DL-Asp gel, distinct spatiotemporal regions of CuAsp polymers were observed (Fig. 5). The evolution of this periodic precipitation is shown in Fig. S6, ESI†. Samples obtained near the interface consistently showed chirality opposite to the introduced TMAs. Solid-state CD analysis reveals a negative Cotton effect in the presence of L-Pro-copper complexes, suggesting the predominance of D-CuAsp (Fig. 5a and c). In contrast, the presence of D-Pro-copper complexes led to positive Cotton effects, indicating L-CuAsp formation near the liquid-gel interface (Fig. 5b and d). These findings align with the 'rule of reversal', where the presence of a homochiral additive influences the chiral environment, promoting the crystallization of the opposite enantiomer. However, the overall chiral intensity decreased when L- and D-Pro-copper complexes were introduced, compared to the coordination polymers formed in the absence of TMAs. This suggests that although these TMAs selectively attached to the nanofibers of the conglomerates with the same configuration, they only partially resolved the DL-Asp conglomerates. This differential impact could be attributed to the inherent differences in how L- and D-Pro complexes interact with DL-Asp and the agar gel environment. Notably, fewer precipitates formed at higher concentrations of Pro-copper complexes than those formed at lower concentrations, likely due to the slower coordination rate: at higher concentrations, the Pro-copper complexes may create a denser environment around the aspartate ligands, leading to increased steric hindrance and reduced mobility. This congestion can slow the rate at which the Pro-copper complexes effectively coordinate with the aspartate, impeding efficient nucleation and subsequent crystal growth. The slower coordination rate thus limits the number of nucleation sites available, resulting in a reduced number of precipitates despite the higher concentration of reactants. Additionally, higher concentrations of TMAs may promote the formation of transient or less stable intermediates, further delaying or hindering the crystallization process.

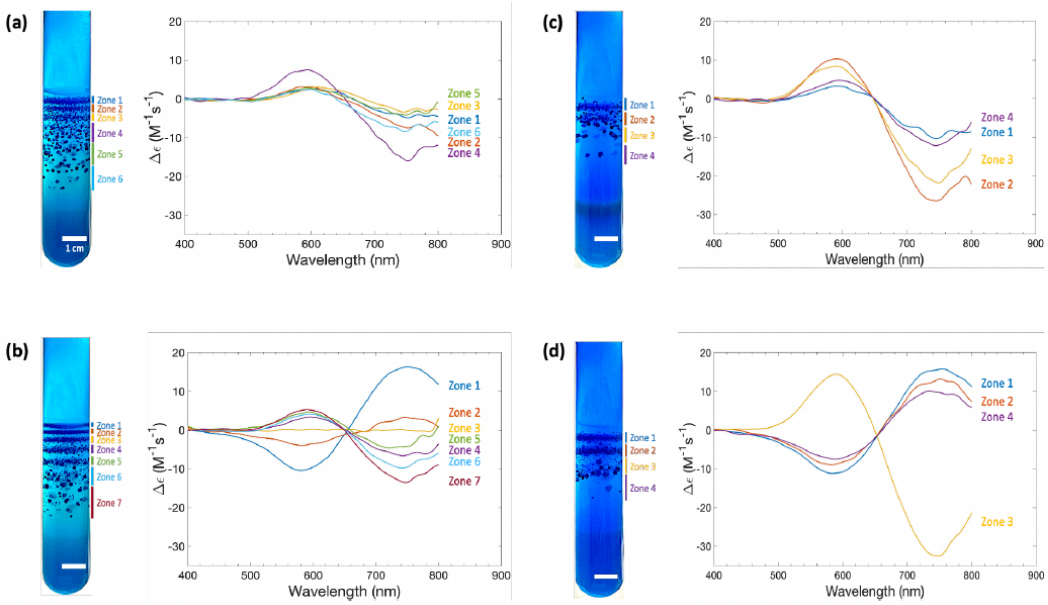

Figure 5 Visualizations of DL-CuAsp coordination complexes crystallized in the presence of (a) 100 mM L-Pro-copper complex, (b) 100 mM D-Pro-copper complex, (c) 200 mM L-Pro-copper complex, and (d) 200 mM D-Pro-copper complex in agar gel, along with the corresponding solid-state CD spectra of each precipitate zone. For (a) and (b), the initial concentrations of the outer electrolyte: [Cu^{2+}] = 300 mM, [Pro] = 100 mM, [NaOH] = 100 mM, while the inner electrolyte consisted of [Agar] = 1%, [DL-Asp] = 50 mM, [NaOH] = 100 mM. For (c) and (d), the inner electrolyte conditions were the same, but the outer electrolyte concentrations were [Cu^{2+}] = 300 mM, [Pro] = 200 mM, [NaOH] = 200 mM; at *ca.* 22 °C.

During crystallizations involving L-Pro-copper additives, mainly coordination polymers with negative Cotton effects were observed across all zones (Fig 5a and c), indicating the predominant formation of D-CuAsp. A lower chiral intensity was observed with 100 mM L-Pro-copper than 200 mM L-Pro-copper. In the case of 100 mM D-Pro-copper additive, a gradual chiral switching of the coordination polymers from positive to negative Cotton effect was observed (Fig. 5b). In contrast, two chiral switching events occurred in the presence of 200 mM D-Pro (Fig. 5d). This switching develops on Harada's work in solution and is attributed to the slower coordination rates and higher steric hindrance introduced by the excessive presence of Pro-copper complexes, which could inhibit effective nucleation and crystallization. The reduced efficiency suggests an optimal

concentration range for the TMAs where they exert maximum influence on the chiral resolution process. Beyond this range, the coordination kinetics may not favor the formation of organized chiral domains.

A factor that can rationalize the effect of L- and D-Pro-copper additive on the chiral distribution of CuAsp could be related to the composition of the agar gel itself, which primarily consists of D-galactose. In the context of the 'rule of reversal', the gel may also influence the chiral crystallization of CuAsp.[29] In other words, the agar could act as a chiral competitor, diminishing the chiral influence of the D-Pro-copper additive. This would be particularly noticeable as the distance from the interface increases and the concentration of the TMA decreases, allowing the agar's intrinsic chirality to become more influential. This result may indicate that while the RDF can create favorable conditions for chiral resolution, the specific chiral interactions and competition with the gel matrix must be considered to optimize the outcome.

Conclusions

In this study, coordination polymerization of CuAsp and additive-assisted preferential crystallization of DL-Asp using L- or D-Pro-copper complexes were conducted *via* the reaction-diffusion framework (RDF) in agar gel. The supersaturation gradient established across the diffusion flux resulted in CuAsp coordination polymers with spherulitic morphology and varied sizes. Solid-state CD analysis revealed that L-CuAsp and D-CuAsp showed positive and negative Cotton effects, respectively, while DL-CuAsp exhibited no Cotton effect. However, PXRD analyses confirmed that all forms of CuAsp, including DL-CuAsp, shared identical diffraction patterns, indicating that DL-CuAsp crystallized as a conglomerate. This was further evident from the results of VTPXRD and TGA, indicating that CuAsp polymers have similar structures and nature.

Introducing chiral additives caused the CuAsp with the opposite configuration to crystallize near the liquid-gel interface. Further from the interface, CuAsp precipitates showed varied chirality due to concentration gradients. Interestingly, with L-Pro-copper complexes, a consistent negative Cotton effect was observed, suggesting that the chirality of the agar gel itself may have influenced the outcome of chiral crystallization. PXRD further confirmed that the resolved CuAsp shared the same crystalline phases as DL-Asp conglomerates without additives.

These results highlight the utility of the RDF, not only as a method for understanding chiral resolution but also as a practical tool for developing innovative strategies for enantioselective separations. The approach provides a promising pathway for further exploration in the design of chiral materials and the application of RDF in other complex coordination systems. Future work may expand this method to other amino acids or ligands, exploring different gel matrices and diffusion conditions to refine and enhance the chiral resolution process.

Author contributions

Poh Ying Fong: investigation, visualisation, formal analysis, writing - original draft; Sehrish Khan: investigation, visualisation, formal analysis; Hatem M. Titi: investigation, formal analysis, visualisation, writing; Manal Ammar: investigation, formal analysis; Fiorenzo Vetrone: supervision, resources, conceptualization, editing; Mazen Al-Ghoul: supervision, conceptualization, investigation, methodology, writing; Louis A. Cuccia: supervision, resources, funding acquisition, conceptualization, investigation, methodology, writing.

Conflicts of interest

There are no conflicts to declare.

Acknowledgments

Financial support from NSERC Canada, the FQRNT-supported multi-university Québec Centre for Advanced Materials (QCAM), and Concordia University are greatly acknowledged. MAG acknowledges the support from the American University of Beirut Research Board. We thank Dr. Ashlee Howarth for allowing access to the PXRD instrument and Dr. Mihails Arhangelskis for his support with the crystal structure studies.

References

1 G. Chakraborty, I.-H. Park, R. Medishetty and J. J. Vittal, *Chem. Rev.*, 2021, **121**, 3751–3891.
2 E. R. Engel and J. L. Scott, *Green Chem.*, 2020, **22**, 3693–3715.
3 J. Zhang, W. Kosaka, Y. Kitagawa and H. Miyasaka, *Nat. Chem.*, 2021, **13**, 191–199.
4 H. Li, K. Wang, Y. Sun, C. T. Lollar, J. Li and H.-C. Zhou, *Mater. Today*, 2018, **21**, 108–121.
5 L. Jiao, *Adv. Mater.*, 2018, **30**, e1703663.
6 S. Wang, Y. Hou, E. Wang, Y. Li, L. Xu, J. Peng, S. Liu and C. Hu, *New J. Chem.*, 2003, **27**, 1144–1147.
7 I. Imaz, M. Rubio-Martínez, L. García-Fernández, F. García, D. Ruiz-Molina, J. Hernando, V. Puntes and D. Maspoch, *Chem. Commun.*, 2010, **46**, 4737–4739.
8 C. Cruz, C. Gonzalez, F. Rubio, J. Erices, K. Wrighton-Araneda, D. Cortés-Arriagada, D. Venegas-Yazigi, N. Audebrand and V. Paredes-García, *Cryst. Growth & Des.*, 2022, **22**, 237–250.
9 I. Imaz, M. Rubio-Martínez, W. J. Saletra, D. B. Amabilino and D. Maspoch, *J. Am. Chem. Soc.*, 2009, **131**, 18222–18223.
10 H. Wu, C. Tian, Y. Zhang, C. Yang, S. Zhang and Z. Jiang, *Chem. Commun.*, 2015, **51**, 6329–6332.
11 M. Mizutani, N. Maejima, K. Jitsukawa, H. Masuda and H. Einaga, *Inorg. Chim. Acta*, 1998, **283**, 105–110.
12 C. Wang, N. Zhang, C.-Y. Hou, X.-X. Han, C.-H. Liu, Y.-H. Xing, F.-Y. Bai and L.-X. Sun, *Transit. Met. Chem.*, 2020, **45**, 423–433.
13 I. Imaz, M. Rubio-Martinez, J. An, I. Sole-Font, N. L. Rosi and D. Maspoch, *Chem. Commun.*, 2011, **47**, 7287–7302.
14 J. Puigmartí-Luis, M. Rubio-Martínez, U. Hartfelder, I. Imaz, D. Maspoch and P. S. Dittrich, *J. Am. Chem. Soc.*, 2011, **133**, 4216–4219.
15 Q. Zhou, R. Sun, Y. Ren, R. Tian, J. Yang, H. Pang, K. Huang, X. Tian, L. Xu and Y. Tang, *Carbon Energy*, 2023, **5**(1), e273.
16 C. Li, K. Deng, Z. Tang and L. Jiang, *J. Am. Chem. Soc.*, 2010, **132**, 8202.

17 F. Pu, X. Liu, B. Xu, J. Ren and X. Qu, *Chem. Eur. J.*, 2012, **18**, 4322–4328.
18 O. Shemchuk, F. Grepioni, T. Leyssens and D. Braga, *Isr. J. Chem.*, 2021, **61**, 563–572.
19 L. Addadi, Z. Berkovitch-Yellin, N. Domb, E. Gati, M. Lahav and L. Leiserowitz, *Nature*, 1982, **296**, 21–26.
20 G. Coquerel, *Novel optical resolution technologies*, 2007, 1–51.
21 G. Springuel and T. Leyssens, *Cryst. Growth & Des.*, 2012, **12**, 3374–3378.
22 B. Tang, W. Wang, H. Hou, Y. Liu, Z. Liu, L. Geng, L. Sun and A. Luo, *Chin. Chem. Lett.*, 2022, **33**, 898–902.
23 H. L. Lee, Y. L. Hung, A. Amin, D. E. Pratama and T. Lee, *Ind. Eng. Chem. Res.*, 2023, **62**, 1946–1957.
24 K. Harada, *Nature*, 1965, **205**, 590–591.
25 K. Harada, *Bull. Chem. Soc. Jpn.*, 1965, **38**, 1552–1555.
26 K. Harada and T. Iwasaki, *Chem. Lett.*, 1972, **1**, 1057–1059.
27 K. Harada and W. Tso, *Bull. Chem. Soc. Jpn.*, 1972, **45**, 2859–2862.
28 L. Addadi, J. van Mil, E. Gati and M. Lahav, Springer, 1981, pp. 355–364.
29 J. Van Mil, L. Addadi, E. Gati and M. Lahav, *J. Am. Chem. Soc.*, 1982, **104**, 3429–3434.
30 I. Weissbuch, L. Addadi, L. Leiserowitz and M. Lahav, *J. Am. Chem. Soc.*, 1988, **110**, 561–567.
31 P. Kongsamai, C. Flood, J. H. Horst and A. E. Flood, *Chem. Eng. Technol.*, 2018, **41**, 1173–1179.
32 L. Gou, H. Lorenz and A. Seidel-Morgenstern, *Cryst. Growth & Des.*, 2012, **12**, 5197–5202.
33 A. G. Shtukenberg, Y. O. Punin, E. Gunn and B. Kahr, *Chem. Rev.*, 2012, **112**, 1805–1838.
34 E. Nakouzi and O. Steinbock, *Sci. Adv.*, 2016, **2**, e1601144.
35 R. Issa, M. Hmadeh and M. Al-Ghoul, *Trans. Tech. Publ.*, *2017*, **380**, 39–47.
36 R. Issa, F. A. Ibrahim, M. Al-Ghoul and M. Hmadeh, *Nano Res.*, 2021, **14**, 423–431.
37 R. Zakhia Douaihy, M. Al-Ghoul and M. Hmadeh, Small, 2019, **15**, 1901605.
38 H. Nabika, M. Itatani and I. Lagzi, *Langmuir*, 2019, **36**, 481–497.
39 J. B. Dalton and C. L. Schmidt, *J. Biol. Chem.*, 1933, **103**, 549–578.
40 T. Lee and Y. K. Lin, *Cryst. Growth & Des.*, 2010, **10**, 1652–1660.
41 K. Nakamoto and A. E. Martell, *J. Chem. Phys.*, 1960, **32**, 588–597.
42 J. Zhou, X. Li, L. Yang, S. Yan, M. Wang, D. Cheng, Q. Chen, Y. Dong, P. Liu and W. Cai, *Anal. Chim. Acta*, 2015, **899**, 57–65.
43 C. Ziejewska, A. Grela and M. Hebda, *Materials*, 2023, **16**, 2044.

Supplementary Information

Towards Spatiotemporal Resolution of Copper Aspartate in Gel

Poh Ying Fong,[a] Sehrish Khan,[a] Hatem M. Titi,[b] Manal Ammar,[c] Fiorenzo Vetrone,[d] Mazen Al-Ghoul[c]* and Louis A. Cuccia[a]*

[a] Department of Chemistry and Biochemistry, Concordia University, 7141 Sherbrooke Street West, H4B 1R6 Montreal, Canada

[b] Department of Chemistry, McGill University, 801 Sherbrooke Street West, H3A 0B8 Montreal, Canada

[c] Department of Chemistry, American University of Beirut, P.O. Box 11-0236, Riad El-Solh, 1107 2020 Beirut, Lebanon

[d] Centre Énergie, Matériaux et Télécommunications, Institut National de la Recherche Scientifique, Université du Québec, 1650 Boul. Lionel-Boulet, J3X 1P7 Varennes, Canada

List of Figures

Materials and methods

Materials

All chemical reagents, L-aspartic acid (from Aldrich Chemical Company), D-aspartic acid (from Alfa Aesar), DL-aspartic acid, L-proline, D-proline (from TCI America), BD™ Difco™ Agar (from Fisher Scientific; Cat# 281230), sodium hydroxide (from BDH Reagents and Chemicals), and copper nitrate trihydrate (from Thermo Scientific Chemicals), were used without further purification. All electrolyte solutions and hydrogels were freshly prepared using Millipore water (18.2 mΩ). Glass test tubes with (20 mm × 125 mm) were used.

Coordination polymerization of homochiral and racemic CuAsp in agar gel

CuAsp coordination polymers were synthesized in test tubes containing both inner and outer electrolytes. Initially, the inner gel solution was prepared by dissolving 0.6 g (1% wt/wt) agar powder in 54 mL of water, heating (80 - 85 ºC), and stirring until completely dissolved. The agar gel was then cooled to 60 ºC. Concurrently, a solution of deprotonated L-, D-, or DL-Asp was prepared by dissolving 0.3993 g (3 mmol) of Asp and 0.24 g (6 mmol) of NaOH in water (6 mL). This solution was then added to the cooled agar gel and stirred for 5 minutes. The mixture was carefully transferred to test tubes, covered, and left to solidify fully (~4 hours). The final concentration of the inner electrolyte was 50 mM Asp and 100 mM NaOH, filling each tube with a total gel volume of 18 mL. The outer electrolyte, composed of copper nitrate trihydrate ($Cu(NO_3)_2 \cdot 3H_2O$) 1.4496 g (6 mmol, 300 mM), was dissolved in water (20 mL) and carefully layered over the gel using a glass Pasteur pipette. The test tubes were sealed with parafilm and left undisturbed to facilitate the controlled diffusion of electrolytes and the formation of distinctive blue spherulitic crystals.

The CuAsp spherulites were collected after the diffusion process was completed. The agar gel was carefully extracted and segmented into different zones using a spatula. Each zone underwent 3-5 washes in hot water to effectively separate the spherulites from the agar gel matrix. The spherulites were transferred to Corning® 15 mL centrifuge tubes, followed by centrifugation at 450 xg for 5 minutes, using an IEC clinical CL bench-model centrifuge equipped with a Rotor 809 (radius = 12.7 cm). Finally, the spherulites were dried overnight in a 60 ºC oven.

Chiral separation of DL-Asp using homochiral Pro-copper complexes in agar gel

The inner electrolyte, consisting of 1 %wt/wt agar and deprotonated DL-Asp, was prepared as described above. The outer electrolyte was then prepared by dissolving 0.2303 g (2 mmol, 100 mM), and 0.4605 g (4 mmol, 200 mM) of L- or D-Pro in water (20 mL), followed by the addition of 0.08 g (2 mmol, 100 mM), and 0.16 g (4 mmol, 200 mM) of NaOH for deprotonation. Subsequently, 1.4496 g (6 mmol, 300 mM) of $Cu(NO_3)_2 \cdot 3H_2O$ was added to the deprotonated Pro solution with continuous stirring for 5 minutes until fully dissolved. This outer electrolyte was then gently layered over the gel using a glass Pasteur pipette. The test tubes were sealed with Parafilm and left undisturbed. After two weeks, the gels were extracted, and the spherulites were isolated as outlined above.

Solid-state circular dichroism (Solid-state CD)

CD spectra were recorded in the range of 400 to 800 nm using a Jasco J-710 spectropolarimeter. The spectra were obtained with a resolution of 5 points/nm, and each curve represents the accumulation of 5 scans at a scan rate of 100 nm/min. A binomial filter with a convolution width of 99 points was applied. Solid-state samples were prepared as Nujol mulls by grinding the samples (2.0 - 2.8 mg) from each zone in a mortar and pestle in Nujol mineral oil to achieve a homogeneous mixture (30 - 35 %wt/wt). This mixture was

then sandwiched between two quartz discs (22.5 mm diameter, 1 mm thick), and the sample assembly was mounted in the instrument using a circular cell holder.

Powder X-ray diffraction (PXRD)
PXRD patterns were collected on a Rigaku MiniFlex 6G X-ray diffractometer equipped with Cu$K\alpha$ radiation (λ = 1.54059 Å) and a sealed-tube X-ray source operating at 40 kV and 15 mA. Samples were smeared onto a zero-diffraction silicon wafer and measured between the 2θ of 3 - 50 in 0.01° step with a scan rate of 10 °/min.

Scanning electron microscopy imaging (SEM)
SEM images were acquired using a Tescan Mira instrument with an accelerating voltage of 15 kV. Prior to imaging, SEM samples were coated with a thin layer of platinum prior to imaging.

Nitrogen adsorption-desorption isotherms
The N_2 adsorption-desorption isotherms were measured at 77 K on a 3Flex Micromeritics instrument. Prior to the measurement, the sample was washed with DMF and DCM, and subsequently dried in a vacuum oven at 70 ºC overnight.

Attenuated total reflectance Fourier-transform infrared (ATR-FTIR)
ATR-FTIR spectra of samples in the form of powders were collected using a Bruker Alpha II FT-IR spectrometer. All spectra were recorded in the wavelength range from 400 cm^{-1} to 4000 cm^{-1}.

Variable temperature-Powder X-ray diffraction (VT-PXRD)
The thermal events for L-CuAsp were performed on a Bruker D8 Advance instrument equipped with a LYNXEYE detector using nickel nickel-filtered Cu$K\alpha$ radiation. The setup was equipped with an Anton Paar CHC^{+} chamber. Diffractograms were collected in a stepwise fashionstepwise in a dry environment. After each pattern was recorded for 6 min, then temperature in the chamber chamber temperature was raised by 5 °C at a heating rate of 30 ºC/min and kept for isotherm at the destination temperature for 1 min before the new scan was collected.

Thermogravimetric analysis (TGA)
TGA and differential scanning calorimetry (DSC) data were measured on a TGA/DSC 1 (Mettler-Toledo, Columbus, Ohio, USA) instrument. Samples (5-6 mg) were placed in alumina crucibles. All measurements were carried under a 25 mL/min stream of air, and the samples were heated from room temperature up to 600 ºC using a constant heating ramp of 10 ºC/min.

Dynamic vapour sorption (DVS)
Prior to the experiment the sample was dried at 100 ºC, for four hours. The experiment was conducted on a surface measurement system (DVS) using a full cycle sorption desorption method. The sorption cycle starts from 0 RH% to 95 RH% sorption with an increment of 5 RH% followed by desorption to 0 RH%, in which the temperature was kept constant at 25 ºC during the measurement on a L-CuAsp sample of 1.6633 mg. At each RH% step, the material will be allowed to equilibrate dm/dt of 0.002% for a period between 10 - 360 min.

UV-Vis spectrophotometry
UV-Vis absorbance spectra were recorded in the range of 200 to 900 nm using a Varian Cary 100 Bio UV-Vis spectrophotometer. The following sample concentrations were prepared: (1) L- and D-Pro solutions at 10 mg/mL (20 mg of Pro in 2 mL of Millipore water), (2) a 10-fold dilution of 300 mM $Cu(NO_3)_2 \cdot 3H_2O$, 100 mM L- and D-Pro-copper

complexes, and (3) a 20-fold dilution for the 200 mM L- and D-Pro-copper complexes. Each solution sample was loaded in a quartz cuvette with an optical path of 2 mm for analysis.

Coordination polymerization and characterization of L-, D-, and DL-CuAsp in agar gel

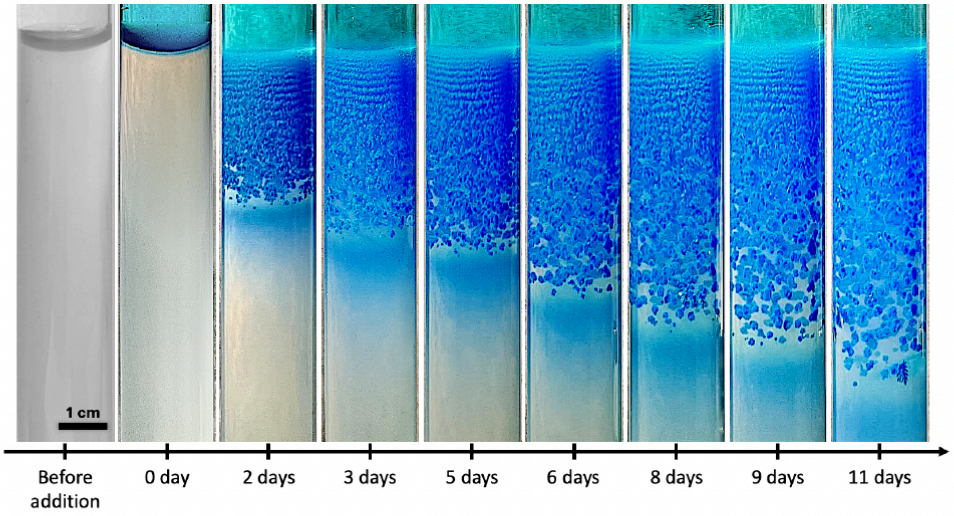

Figure S1. Time-lapse images of D-CuAsp periodic precipitation in 1D agar gel system. The diffusion of 300 mM $Cu(NO_3)_2 \cdot 3H_2O$ into 1% agar gel containing 50 mM deprotonated D-aspartic acid (with 100 mM NaOH) was carried out at room temperature (~ (*ca.* 22 ºC).

Attenuated total reflectance Fourier-Transform infrared (ATR-FTIR)

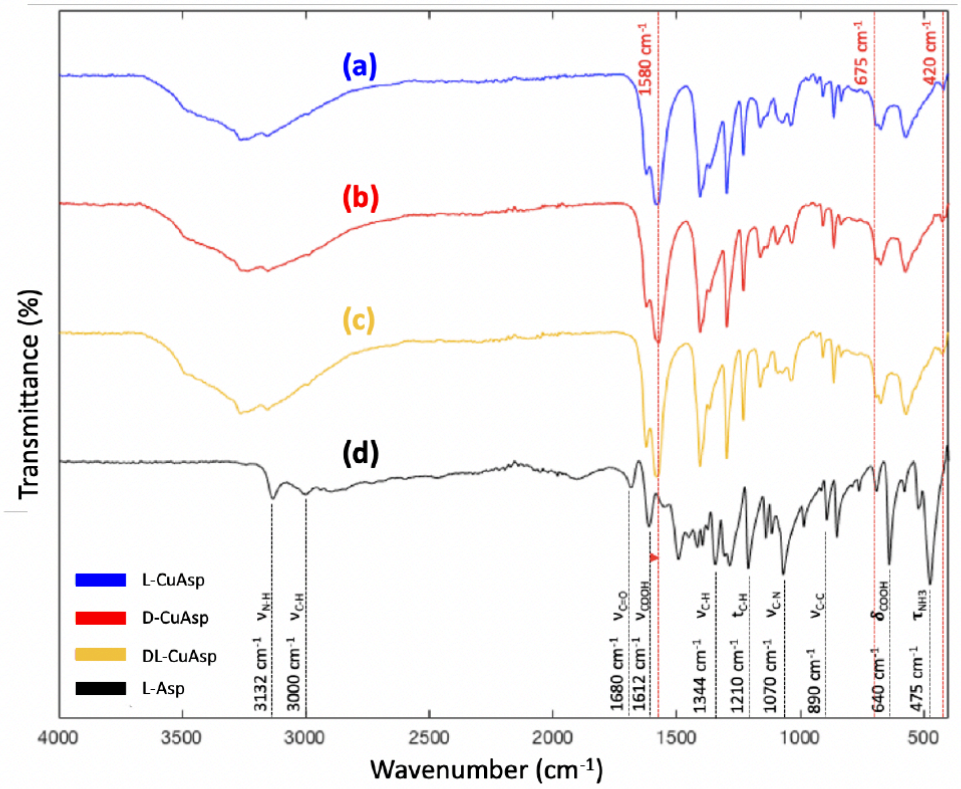

Figure S2. ATR-FTIR transmittance spectra of (a) L-, (b) D-, and (c) DL-CuAsp compared with (d) L-aspartic acid. Initial concentrations of the outer electrolyte: [Cu^{2+}] = 300 mM; inner electrolyte: [Agar] = 1%, [Asp] = 50 mM, [NaOH] = 100 mM at *ca.*~ 22 ºC.

Nitrogen isotherm and Brunauer-Emmett-Teller (BET) analysis

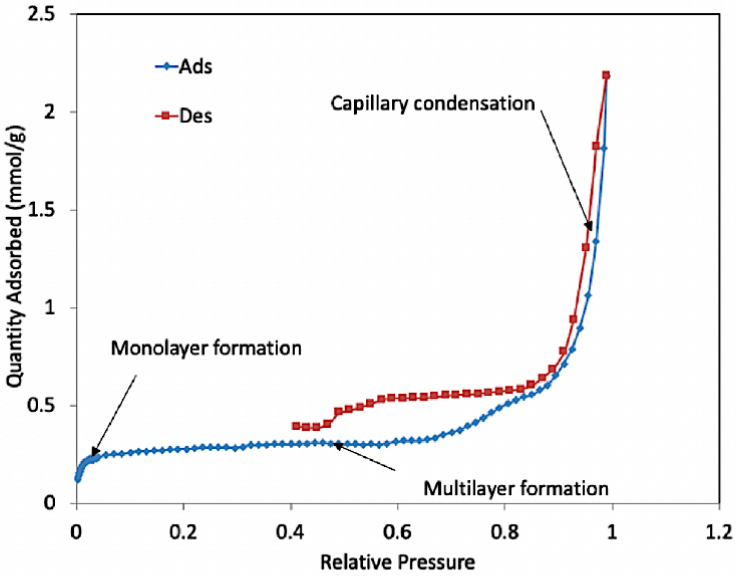

Figure S3. N_2 adsorption-desorption isotherm of DL-CuAsp at 77 K. The blue curve represents the adsorption isotherm, whereas the red curve is the desorption isotherm. Initial concentrations of the outer electrolyte: [Cu^{2+}] = 300 mM; inner electrolyte: [Agar] = 1%, [DL-Asp] = 50 mM, [NaOH] = 100 mM at *ca.* ~ 22 ºC.

Table 1. BET surface area and pore width of DL-CuAsp.

Analysis	Data
BET surface area	21 m^2/g
Pore width	190 Å

Solid-state circular dichroism (CD) spectra of DL-CuAsp individual spherulites

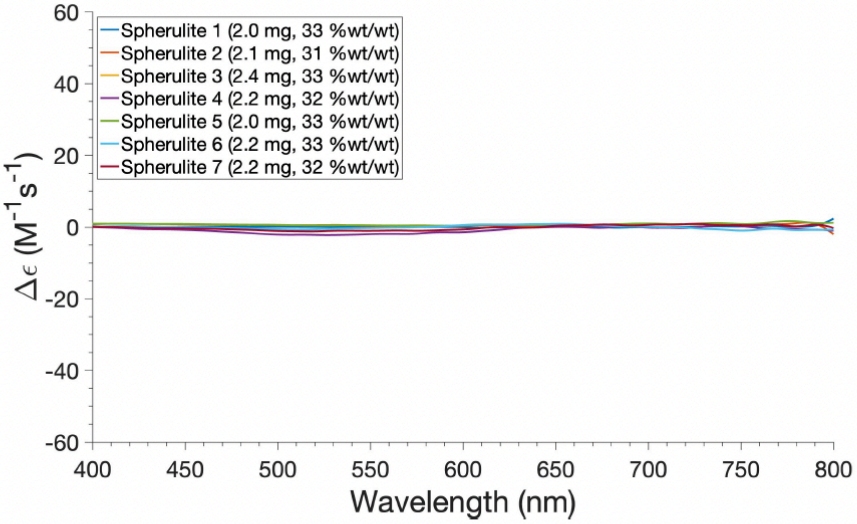

Figure S4. Solid-state CD for individual spherulites of DL-CuAsp, showing no Cotton effect. Initial concentrations of the outer electrolyte: [Cu^{2+}] = 300 mM; inner electrolyte: [Agar] = 1%, [DL-Asp] = 50 mM, [NaOH] = 100 mM. The sample mass from each spherulites and their corresponding %wt/wt in Nujol mineral oil are provided in the legend.

UV-Vis spectra

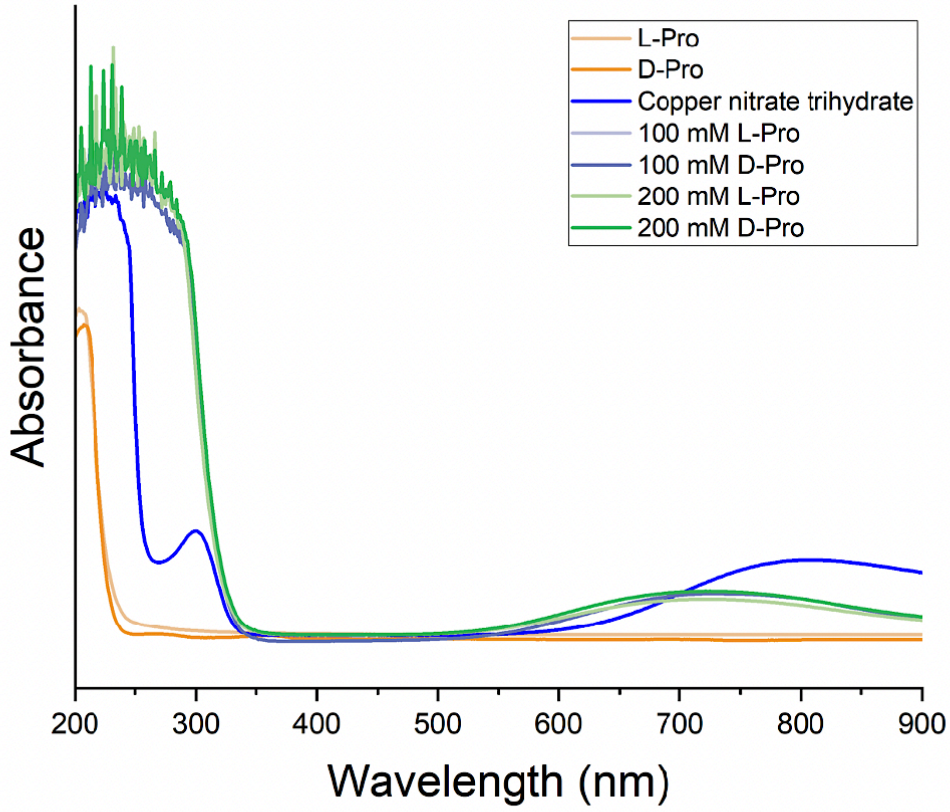

Figure S5. UV-Vis spectra of the starting materials (L- and D-Pro, $Cu(NO_3)_2 \cdot 3H_2O$) and copper complexes with 100 mM and 200 mM L- and D-Pro. The following sample concentrations were prepared: (1) L- and D-Pro solutions at 10 mg/mL (20 mg of Pro in 2 mL of Millipore water), (2) a 10-fold dilution of 300 mM $Cu(NO_3)_2 \cdot 3H_2O$, 100 mM L- and D-Pro-copper complexes, and (3) a 20-fold dilution for the 200 mM L- and D-Pro-copper complexes.

Chiral resolution of DL-Asp in the presence of homochiral Pro-copper complexes in agar gel

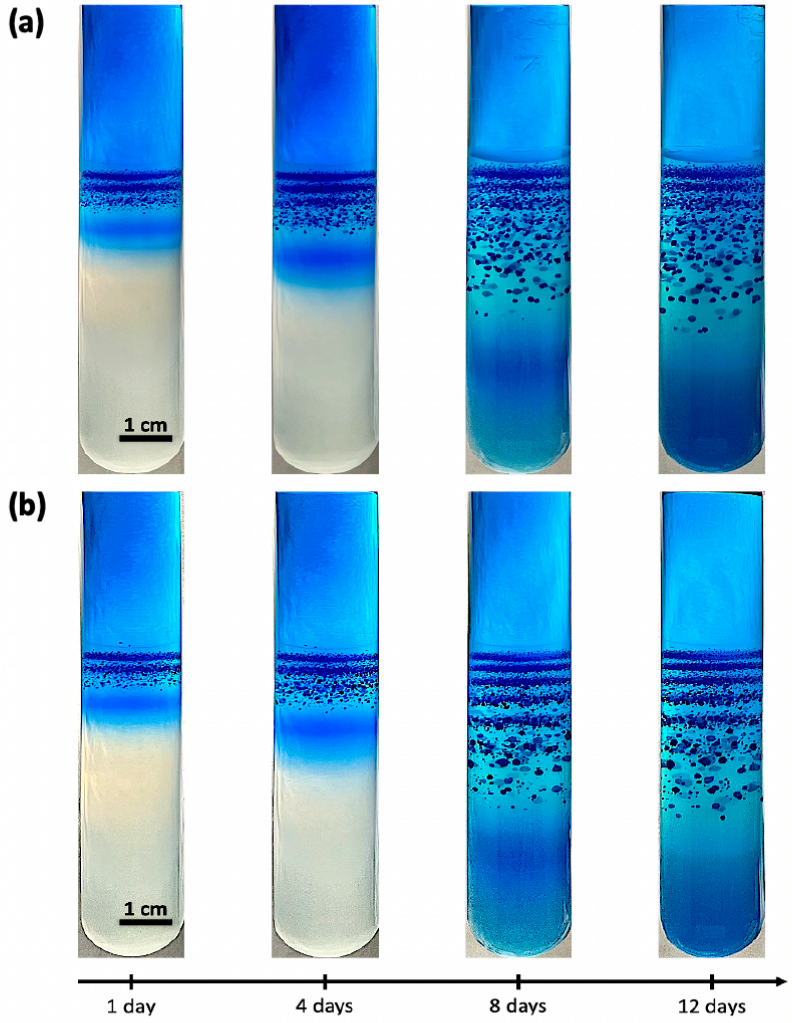

Figure S6. Periodic precipitation of chiral resolution of DL-Asp in the presence of 100 mM (a) L-Pro-copper complex and (b) D-Pro-copper complex in 1D system. Initial concentrations of the outer electrolyte: [Cu^{2+}] = 300 mM, [Pro] = 100 mM, [NaOH] = 200 mM; inner electrolyte: [Agar] = 1%, [DL-Asp] = 50 mM, [NaOH] = 100 mM at ~ *ca.* 22 ºC.